

INAUGURAL-DISSERTATION
zur
Erlangung der Doktorwürde
der
Naturwissenschaftlich-Mathematischen
Gesamtfakultät
der
Ruprecht-Karls-Universität
Heidelberg

vorgelegt von

Dipl.-Phys. Xianguo Lu
aus Shunde, China

Tag der mündlichen Prüfung: 22. Oktober 2013

**Exploring the performance limits of
the ALICE Time Projection Chamber
and Transition Radiation Detector
for measuring identified hadron production
at the LHC**

Gutachter: Prof. Dr. Johanna Stachel
 Prof. Dr. Norbert Herrmann

Zusammenfassung

Die Zeitprojektionskammer (TPC) und der Übergangsstrahlungsdetektor (TRD) sind die wesentlichen Komponenten für Spurrekonstruktion und Teilchenidentifikation im Experiment ALICE am LHC am CERN. In dieser Arbeit werden Methoden jenseits des ursprünglich vorgesehenen Anwendungsbereichs dieser Detektoren entwickelt: die Erweiterung der Impulsmessung mit der TPC auf kosmische Strahlung im sub-TeV Bereich, die zuverlässige Identifikation von Elektronen und Hadronen mit dem TRD, sowie die Entwicklung neuer Methoden zur Beschreibung des TPC und TRD Signals. Diese ermöglichen die Messung von Übergangsstrahlung von Myonen aus der Höhenstrahlung mit Energien im sub-TeV Bereich, sowie die Identifikation unterschiedlicher Teilchenarten mit Impulsen von 0.5 bis oberhalb von 20 GeV/ c .

Der neu entwickelte “TPC coherent fit” zur Untersuchung des TPC Signals erlaubt die Messung der Transversalimpulsspektren ($0.6 < p_T < 20$ GeV/ c) von Pionen, Kaonen und Protonen im zentralen Rapiditybereich $|y| \lesssim 0.8$ in Proton-Proton Kollisionen bei $\sqrt{s} = 2.76$ und 7 TeV und in Blei-Blei Kollisionen bei $\sqrt{s_{NN}} = 2.76$ TeV. Der universelle Ansatz, mit Gültigkeit über einen weiten Impulsbereich, erlaubt sowohl die Beobachtung der sogenannten Baryonanomalie, die ungewöhnliche Erhöhung des Verhältnisses zwischen Protonen und Pionen bei moderatem p_T (2–8 GeV/ c), als auch die nukleare Modifikation der Teilchenproduktion bis zu hohem p_T (> 10 GeV/ c) in Blei-Blei Kollisionen. Des Weiteren wird die Teilchenproduktion in Jets in Proton-Proton Kollisionen bei 7 TeV untersucht, wobei die Ergebnisse des “Perugia-0 Tune” von PYTHIA6 gute Übereinstimmung mit den experimentellen Resultaten zeigen.

Abstract

The Time Projection Chamber (TPC) and Transition Radiation Detector (TRD) are the main tracking and particle identification devices in the ALICE experiment at the CERN LHC. This thesis studies aspects of their performance beyond the original designs. This includes extending the TPC momentum measurement for cosmic rays to sub-TeV scale, investigating a robust identification method for electrons and hadrons by the TRD, and developing new approaches to characterize the TPC and TRD signals. These studies lead to an intriguing observation of the transition radiation from sub-TeV cosmic muons, and a universal method – the TPC coherent fit – to extract yields of different particle species with momentum from 0.5 to above 20 GeV/ c .

With the TPC coherent fit, transverse momentum spectra ($0.6 < p_T < 20$ GeV/ c) of pions, kaons and protons at mid-rapidity ($|y| \lesssim 0.8$) in pp collisions at $\sqrt{s} = 2.76$ and 7 TeV and Pb–Pb collisions at $\sqrt{s_{NN}} = 2.76$ TeV at the LHC are measured. In this unified approach both the anomalous enhancement of the proton-to-pion ratio at moderate p_T (2–8 GeV/ c) (the so-called baryon anomaly) and the nuclear modification of particle yields up to high p_T (> 10 GeV/ c) in Pb–Pb collisions are observed. The particle production is also studied in jets from pp collisions at 7 TeV and the results are well described by Perugia-0 tune of PYTHIA6.

Contents

1	Introduction	1
1.1	Quark-gluon plasma	3
1.2	Particle production in heavy ion collisions	6
1.3	The ALICE experiment	9
1.4	Outline of this thesis	11
2	TPC combined cosmic track fit	15
2.1	Implementation	16
2.2	Momentum resolution	17
3	A general statistical description of the TRD signal	23
3.1	The Landau distribution	23
3.1.1	Distribution of the number of interactions	25
3.1.2	Distribution of the azimuthal deflection angle	26
3.1.3	Distribution of the energy transfer	26
3.2	Distribution of the collisional ionization signal	29
3.3	Distribution of the combined signal of collisional ionization and transition radiation	32
4	TRD signals from sub-TeV cosmic muons	35
4.1	Measurement	36
4.2	Discussion	38
5	TRD truncated mean signal	41
5.1	Influence of the time-bin dependence of the cluster signals	42
5.2	Time-bin gain calibration	43
5.3	Tuning the truncation fraction	46
5.4	Dependence on the number of clusters	47
5.5	Particle identification with the truncated mean signal	50

CONTENTS

6 The TPC coherent fit	53
6.1 Setting the stage	54
6.1.1 Definition of the momentum observable	54
6.1.2 η -window restriction	56
6.1.3 η dependence of particle fractions	56
6.2 Machinery	57
6.2.1 Static features	58
6.2.2 Dynamic features	63
6.3 Error definition	63
6.4 Data analysis results	64
6.5 TPC coherent fit with subsidiary particle identification	69
6.6 Summary	73
7 Pion, kaon, and proton production in pp and Pb–Pb collisions	75
7.1 Procedure	75
7.1.1 Data sets and cuts	75
7.1.2 Systematic effects of the event cuts on the p_{T} -spectra	76
7.1.3 Contamination by secondary particles	77
7.1.4 Tracking efficiency	78
7.1.5 Calculation of p_{T} -spectra and yield ratios	80
7.2 Results and discussions	82
7.3 Outlook – identified jet fragmentation	90
8 Summary and conclusion	93
A Exclusive central production of $\pi^+\pi^-$	95
B Track cuts for the particle production analysis	97
List of Figures	99
List of Tables	105
Bibliography	107

Chapter 1

Introduction

Since the beginning of the 20th century, the understanding of the building blocks of matter has been evolving. In the Standard Model (SM) of particle physics [Ber12], the elementary particles are quarks, leptons, gauge bosons and the Higgs boson [Aad12, Cha12a]. Quarks are the constituents of hadrons, of which the protons and neutrons are the constituents of atomic nuclei. Leptons, of which the electron is the most common in daily life, make up another sector of the matter in the universe. The gluons, the photon, and the W - and Z -bosons are the gauge bosons mediating the fundamental interactions: the strong, electromagnetic and weak interactions¹, respectively. The Higgs boson is related to the mass generation of other elementary particles. The dynamics of the SM is provided by quantum field theory, where the concept of particles is promoted to quantum fields, whose quantum fluctuations represent the creation and annihilation of particles. The matter and gauge fields carry not only energy and momentum, but also charges which are conserved as a consequence of the symmetry due to the redundant degrees of freedom in the Lagrangian (Noether's theorem). The strong interaction in the SM is described by quantum chromodynamics (QCD), where the SU(3) group is the underlying symmetry. The corresponding charges are the three so-called colors which are carried not only by the six flavor of quarks but also by the eight gluons. The gluons carry different color-anticolor combinations and can couple to each other. This peculiar feature leads to fascinating phenomena of the strong interaction.

Due to quantum fluctuations, the vacuum is not empty. Condensates of gluons and quarks populate the vacuum [Shi79a, Shi79b]. The gluon condensate leads to the breaking of the dilatation symmetry, also known as the scale invariance, of the QCD Lagrangian, while the quark condensate, also called “chiral condensate”, leads to the spontaneous breaking of the chiral symmetry. In the presence of charge coupling, the vacuum is polarized. Virtual particles are created from the momentum transfer associated with the coupling and then propagate over a short interval of time before they annihilate each other. The coupling is modified by the screening and/or antiscreening by these virtual particles.

In QCD, self-coupling allows gluons to also participate in vacuum polarization, leading to an antiscreening of the color charge. In other words, the effective charge increases as the distance from it becomes larger. At a distance² larger than $1/\Lambda_{\text{QCD}}$, which is about 1

¹Gravity is not included in the SM.

²A system of units with $\hbar = c = k_B = 1$ is used, where \hbar , c , k_B are the Planck constant, the speed of

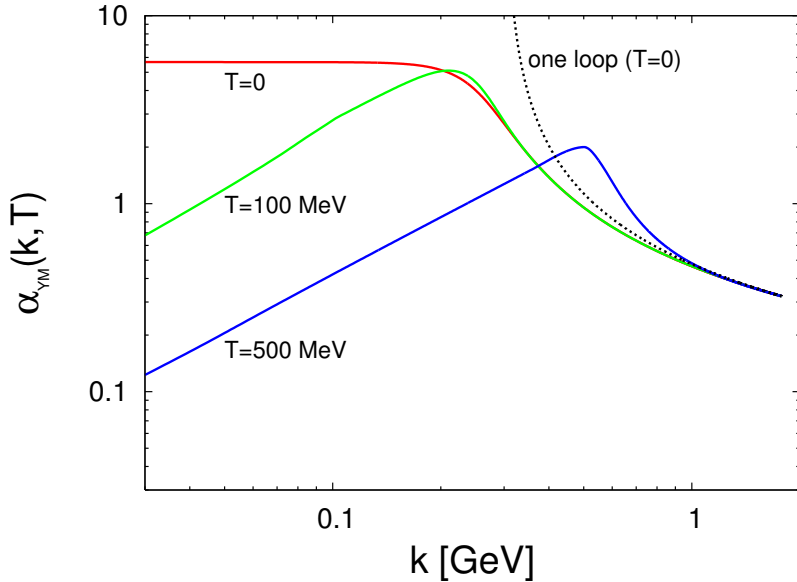


Figure 1.1: Running coupling in a pure SU(3) gauge (i.e. no quark degree of freedom) theory at finite temperature (colored curves). Figure from [\[Brau07\]](#).

fm with the QCD scale $\Lambda_{\text{QCD}} \sim 200$ MeV, the coupling is so strong that such a separation between color charges requires an infinite amount of energy, a phenomenon known as color confinement. Instead of quarks and gluons, hadrons – the color singlet bound state either of a quark and an antiquark (meson) or of three quarks (baryon)³ with a spatial extension of about 1 fm – are therefore the natural degrees of freedom in QCD. The experimentally observed hadron spectrum suggests that the QCD vacuum is chirally asymmetric: if chiral symmetry were unbroken then each hadronic state would be degenerate in parity [\[Gas82\]](#). At a small distance, or equivalently with a large momentum transfer $k \gg \Lambda_{\text{QCD}}$, the strong coupling α_s decreases with the scale k as $1/\ln(k/\Lambda_{\text{QCD}})$. The color interaction at very small distance is so weak that quarks and gluons behave like free particles as is observed in deep inelastic scattering of leptons off nucleons [\[Bre69\]](#). This is the so-called asymptotic freedom [\[Gro73, Pol73\]](#).

In the presence of a medium, in addition to quantum fluctuations, thermal fluctuations of the matter and gauge fields further modify the interactions. The modification due to the screening by real particles, whose population is determined by their thermal distributions, depends on the temperature and the chemical potential. For the strong interaction, the effects can be characterized by the Debye mass, which is related to the strength of the exponential screening to the chromo-electric field, and the Meissner mass of the quasi-particle propagation mode of the chromo-magnetic interaction, which represents the inverse interaction range [\[Gro81, Alf08\]](#). With increasing temperature T or quark chemical potential μ , both masses grow linearly and hence the effective interaction is weakened. The effective strong coupling at given scale k depends on T and μ . For example, Fig. 1.1

light and the Boltzmann constant, respectively.

³Without the quark degree of freedom, confinement and asymptotic freedom – driven by gluon self-coupling – still hold, as is shown by pure gauge calculations. Nevertheless, the bound state of pure gluons – the glueball – has not been experimentally conclusively confirmed.

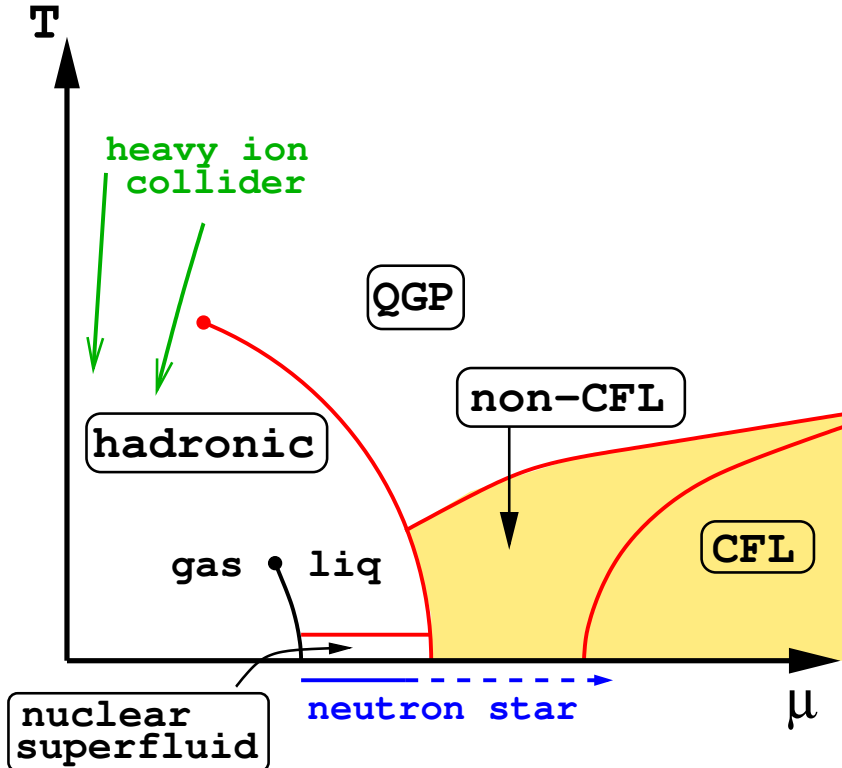


Figure 1.2: A schematic QCD phase diagram. Figure from [Alf08].

shows the running coupling calculated as a function of k and T [Brau07].

An important consequence of the running strong coupling $\alpha_s(k, T, \mu)$ as a function of T and μ is that at ultra-high temperature and/or density, color is deconfined [Cab75, Col75] and different forms of quark matter exist. Figure 1.2 is a schematic QCD phase diagram. In the regime of high temperature there is quark-gluon plasma (QGP) [Shu78] which is generally believed to have filled the universe for the first few microseconds after the Big Bang (see for example [Sch03]), and to have been created in ultra-relativistic heavy ion collisions in laboratories [Hei00, Ada05, Adc05, Ars05, Bac05]. In the low temperature high density regime it is expected that a degenerate liquid of quarks in the form of color superconductor, the so-called color-flavor locked (CFL) phase, exists in the cores of neutron stars (for a review cf. [Alf08]).

1.1 Quark-gluon plasma

In 1965, Hagedorn [Hag65] noted that the mass spectrum of hadronic states suggests an exponential growth and postulated “the highest possible temperature for strong interactions” near to 160 MeV (Fig. 1.3). Cabibbo and Parisi [Cab75] suggested that in the framework of the quark model the Hagedorn-type exponential spectrum is connected to a phase transition to a state where quarks are liberated. Another proposal for quark deconfinement was provided by Collins and Perry [Col75] using asymptotic freedom arguments. They showed that for the strong interaction at sufficiently high densities the

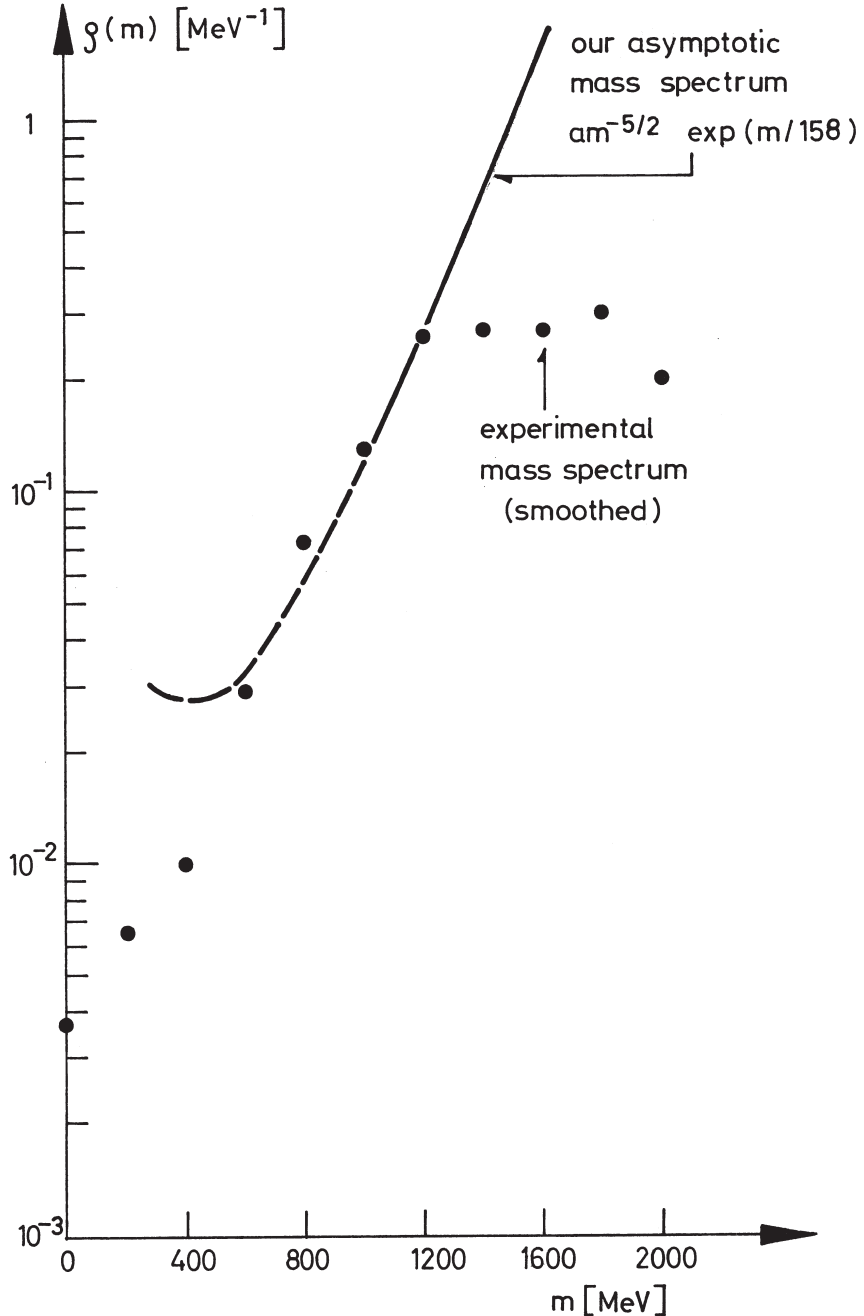


Figure 1.3: The hadronic mass spectrum from [Hag65]. For an update, cf. [Bro04].

effective coupling becomes arbitrarily small. Similar arguments may be applied for high temperature. This new phase of matter at high temperature was first called “plasma” by Shuryak [Shu78] because “explicit calculation [...] has produced positive sign of the Debye mass, opposite to that of virtual gluons and the same as in (quantum electrodynamics) QED” [Shu09]. At the time when the deconfinement phase transition was conceived, a chiral phase transition towards the restoration of chiral symmetry at high temperature was also conjectured [Gro81]: following a similar argument to deconfinement, as the temperature increases, all correlations between quarks decay exponentially, preventing the symmetry breaking.

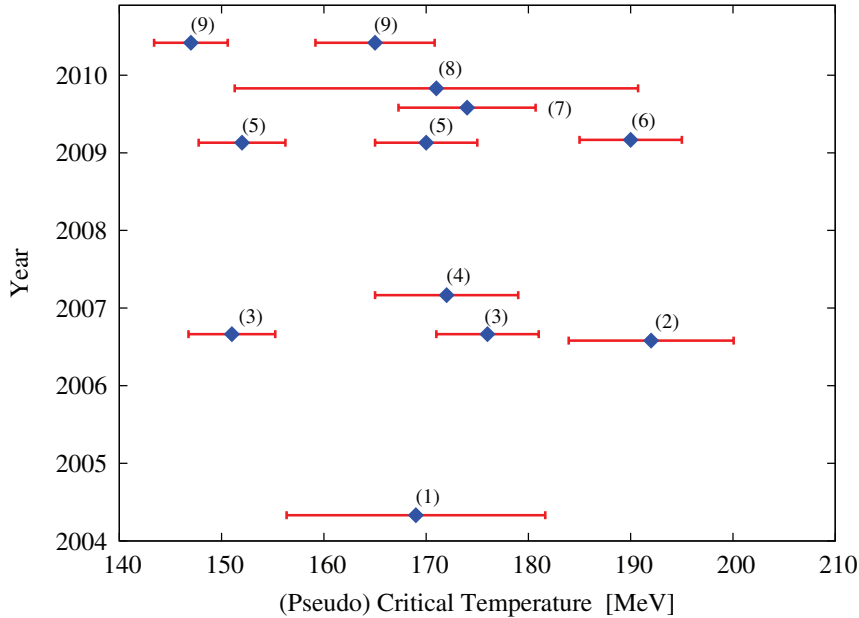


Figure 1.4: Pseudo-critical temperature T_{pc} for QCD transition(s) determined by recent lattice QCD calculations. Figure from [Fuk11], for details cf. references therein.

The QCD transitions have been studied, among many other approaches, with first-principle calculations using lattice QCD [Wil74, Kog75] by which the QCD Lagrangian is formulated in discretized space-time and results are obtained by extrapolation to the continuum limit. The deconfinement phase transition was first shown on the lattice by investigating the temperature dependence of the potential between two color charges in a pure gluonic system⁴ [Pol78, Sus79, Kut81, McL81]: at high temperature, the potential becomes a finite constant at a large distance due to the screening by gluons, in contrast to the zero temperature case where it increases linearly with the charge separation. Another demonstration came from the energy density of gluon matter [Eng81] which was shown to rise rapidly and approach the Stefan-Boltzmann limit of a free gluon gas as the temperature increases, indicating as well the liberation of new degrees of freedom. The first demonstration of the chiral phase transition was obtained using lattice calculations with quarks in the quenched approximation (leading order in the limit of a small number of quark flavors) in the small mass limit [Kog82, Kog83] by showing that the chiral condensate vanishes at large temperature.

The nature of the transitions observed in lattice calculations depends on how symmetries are realized. With physical quark masses in the full QCD theory, no global symmetry⁵ of the Lagrangian survives. As it turns out, both the deconfinement and chiral phase transitions are analytic crossovers at similar temperatures [Aok06, Bor10a]. The determination of these pseudo-critical temperatures is summarized (see [Fuk11] and references therein) in Fig. 1.4. As can be seen they lie between 140-200 MeV. The temperature dependence of the energy density obtained with physical lattice configurations [Bor10b] is shown in Fig. 1.5 (see also [Baz10]).

⁴In [Pol78, Sus79] the potential was translated to the free energy of the system. In [Kut81, McL81] the free energy of an isolated charge was further represented by what is nowadays called the Polyakov loop.

⁵Except the trivial U(1) symmetry for baryon number conservation.

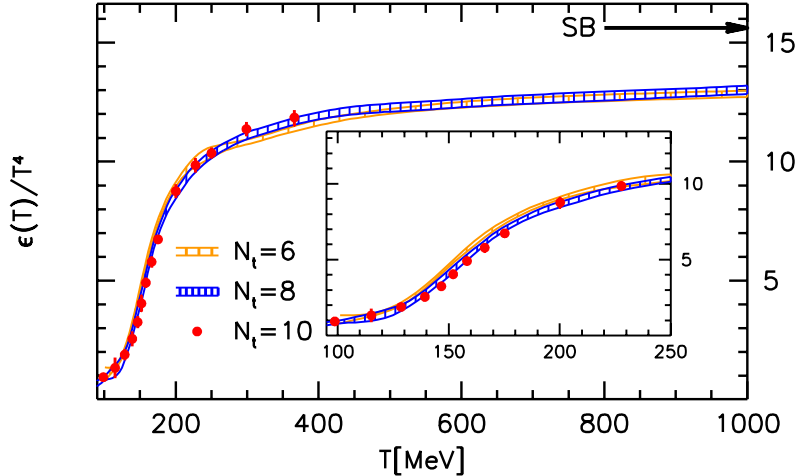


Figure 1.5: Lattice results on the temperature dependence of the energy density ϵ . Figure from [Bor10b]. The Stefan-Boltzmann limit of an ideal gas of quarks and gluons is indicated by an arrow. See also [Baz10].

1.2 Particle production in heavy ion collisions

The pseudo-critical energy density for the phase transitions is estimated as about 0.7 GeV/fm^3 following the discussion above if one takes the pseudo-critical temperature at $T_{pc} = 170 \text{ MeV}$ from Fig. 1.5, which is about four times that of normal nuclei (0.16 GeV/fm^3). For a given accelerator energy, to create the highest energy density it is necessary to accelerate as heavy nuclei as possible. This is not a sufficient condition to observe QGP due to issues like the efficiency of energy transfer into the system produced and whether this system is large and long-lived enough to equilibrate (see discussions in [Sta93] and [Bra03]).

Existing facilities with largest maximum initial energy density are the Relativistic Heavy Ion Collider (RHIC) at Brookhaven National Laboratory (BNL) in New York, USA and the Large Hadron Collider (LHC) at the European Organization for Nuclear Research (CERN) near Geneva, Switzerland. RHIC, completed in 1999, provides Au–Au collisions up to a center-of-mass energy 200 GeV per nucleon-pair, i.e. $\sqrt{s} = 200 \text{ A GeV}$ or $\sqrt{s_{NN}} = 200 \text{ GeV}$. The LHC, which restarted operation in 2009, has provided Pb–Pb collisions at $\sqrt{s_{NN}} = 2.76 \text{ TeV}$ and is planned to eventually double the accelerator energy after the shutdown for upgrade between 2013 and 2015. The initial energy density achieved in these ultra-high energy heavy ion collisions has been estimated model-dependently, at RHIC being $14\text{--}20 \text{ GeV/fm}^3$ [Bra07], well above the critical values from lattice QCD calculation. Measurements at the LHC imply that the initial energy density is approximately a factor of three higher than at RHIC [Mul12].

The matter formed in the early stages of the collisions, instead of being a pure hadron gas, behaves like a perfect liquid – very strongly interacting, the mean free path of the constituents being very short and the shear viscosity being very small [Kol03, Shu04]. This matter expands both in the longitudinal and transverse directions. The first case is sensitive to the initial conditions of the colliding nuclei while the latter, driven by the transverse pressure gradients, is hydrodynamic – the velocities of neighboring particles are

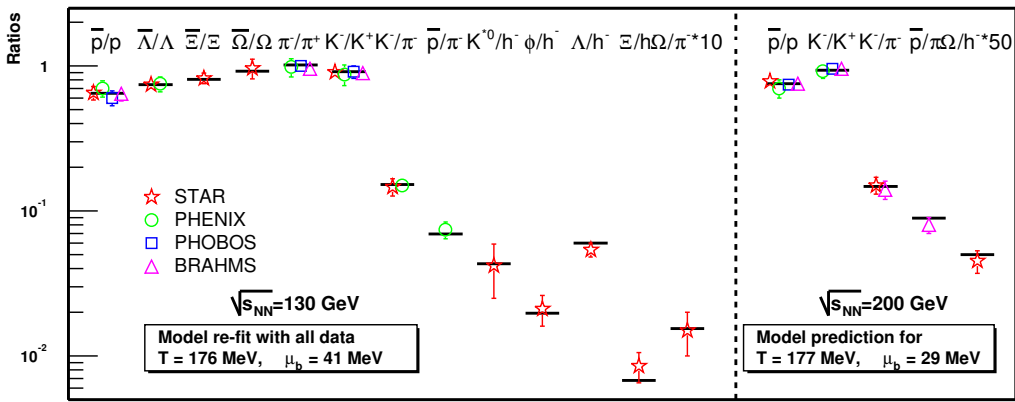


Figure 1.6: Relative particle abundances measured at RHIC at $\sqrt{s_{NN}} = 130$ and 200 GeV compared to thermal model calculations. Figure from [Bra03].

strongly correlated hence being collective. As the matter cools down it experiences chemical and kinetic freezeout and in the end all particles that are produced decouple and stream freely. The chemical freezeout, at which inelastic collisions between the constituents of the matter cease, is determined from the measured abundances of particle species assuming chemical equilibrium [Bra96, Bra03]. Figure 1.6 shows the two-parameter calculation for relative particle abundances, with the temperature T and baryon chemical potential μ_B at the freezeout, compared to measurements. The kinetic freezeout, i.e. the termination of elastic collisions among the hadrons, can be studied with the differential particle production on the transverse momentum p_T . The hydrodynamics-motivated blast-wave model [Sch93] has been used for this purpose (cf. discussions in [Abe13a]).

In general, particle p_T spectra can provide information about the production mechanism and the related medium effects. Hadrons (heavy flavors, the c and b quarks, are not considered) in high energy nuclear collisions can either be produced by a large momentum transfer (“hard” process), characterized by a high p_T , in the first instance of the interaction or from the subsequent parton production governed by multi-parton “soft” collisions. Hadrons with p_T larger than the soft scale progressively decouple from the collective motion of the bulk matter and the matter properties other than hydrodynamics begin to be important for the production. It was discovered at RHIC [Adc02a, Adl03, Abe06] that in the intermediate p_T region ($2\text{--}6$ GeV/ c) the baryon-to-meson ratios are strongly enhanced in nucleus-nucleus collisions – the so-called baryon-anomaly, as is shown in Fig. 1.7. A quantitative understanding of this phenomenon still remains a challenge [Bro08, Fri08, Top11]. The production of high- p_T hadrons originating from the fragmentation of high- p_T partons is predicted to experience attenuation due to energy loss in the QGP medium [Bjo82, Gyu90, Wan92], a phenomenon termed “jet quenching”. It has been first confirmed at RHIC [Adc02b, Adl02] where the effect was quantified by the nuclear modification factor R_{AA} which is the suppression of the hadron yields in nucleus-nucleus collisions compared to those in nucleon-nucleon collisions scaled by the number of binary collisions. The measurements at the LHC [Aam11a, Cha12b] show a stronger modification (see Fig. 1.8) and therefore indicate an enhanced energy loss and hence a denser medium produced at the LHC.

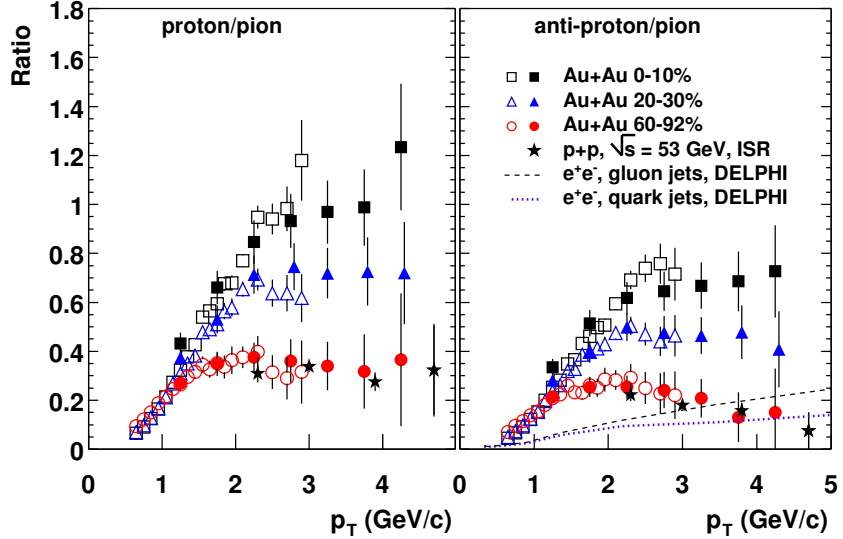


Figure 1.7: p/π and \bar{p}/π ratios for Au–Au collisions at $\sqrt{s_{NN}} = 200$ GeV at RHIC. Figure from [Adl03].

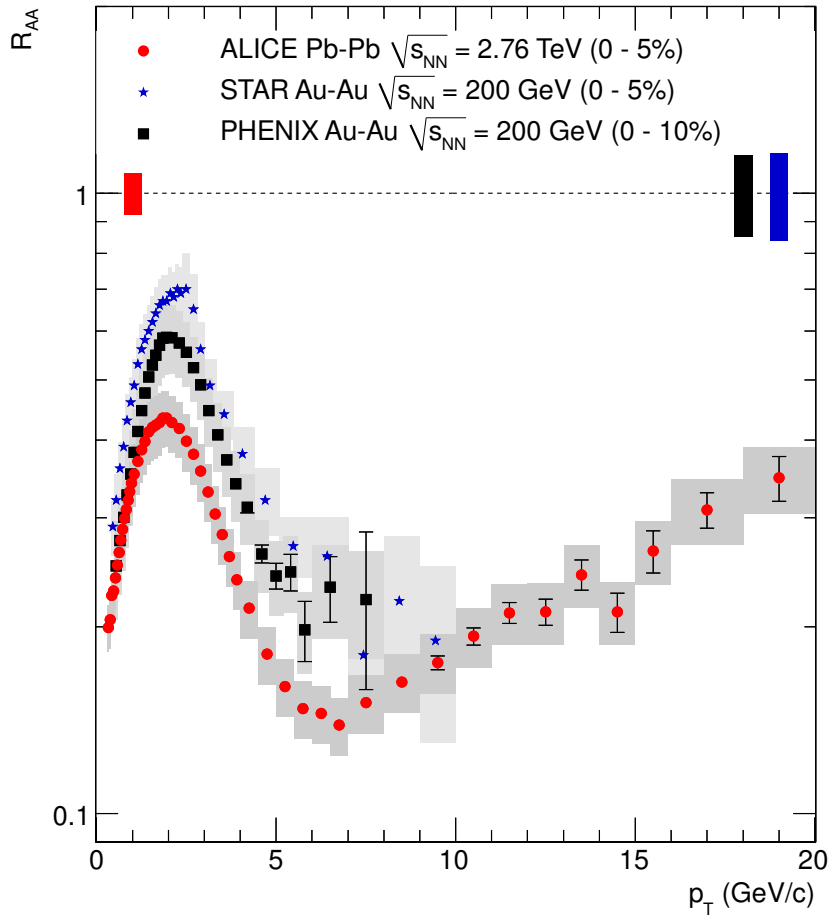


Figure 1.8: Nuclear modification factor R_{AA} in central Pb–Pb collisions at $\sqrt{s_{NN}} = 2.76$ TeV at the LHC compared to measurements at $\sqrt{s_{NN}} = 200$ GeV at RHIC. Figure from [Aam11a].

1.3 The ALICE experiment

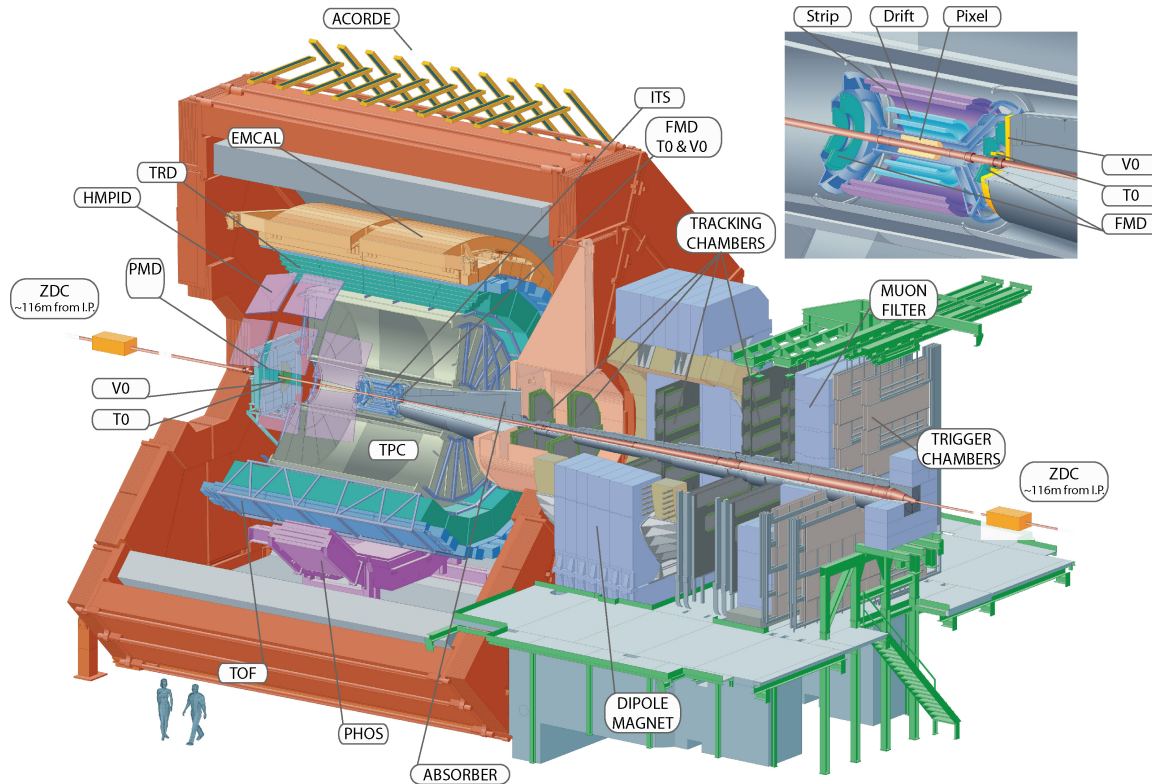


Figure 1.9: The ALICE detector in 3D view. The inset shows the ITS.

The ALICE experiment [Aam08] at the CERN LHC [Eva08] is a heavy ion experiment with the main goal to study Pb–Pb collisions at the LHC energies. The acceptance is divided into the central region covering a range of polar angle $45^\circ < \theta < 135^\circ$ and the forward regions (Fig. 1.9). In the central region which is entirely enclosed by a solenoidal magnet with field strength 0.5 T, the particle identification (PID) and tracking detectors are, from the collision point outwards, the Inner Tracking System (ITS), the Time Projection Chamber (TPC), the Transition Radiation Detector (TRD) and the Time-Of-Flight detector (TOF). Detectors that cover partial azimuth, the Photon Spectrometer (PHOS), the Electro-Magnetic Calorimeter (EMCal) and the High Momentum Particle Identification Detector (HMPID), locate also in the central region. In the forward regions, the forward scintillator hodoscopes (VZERO) are used for triggering and the Zero Degree Calorimeters (ZDCs) for measuring the interaction remnants of the nuclear collisions. The forward muon spectrometer, which is optimized for the study of heavy quarkonia via the muon decay channel, locates in the pseudo-rapidity region $2.5 < \eta < 4$, with $\eta \equiv -\ln \tan \theta/2$. An absorber in front is used to absorb the hadronic background. In the following the detectors which are involved in this work will be described.

The ITS consists of three types of silicon detectors in six cylindrical layers, the Silicon Pixel Detectors (SPD), the Silicon Drift Detectors (SDD) and the Silicon Strip Detectors (SSD), ranging from a radial position of 3.9 cm to 43.0 cm from the beam axis (Fig. 1.9 inset). It provides precise space point measurements for the tracking. In addition, the SPD is included in the minimum-bias trigger logic, which requires at least one charged

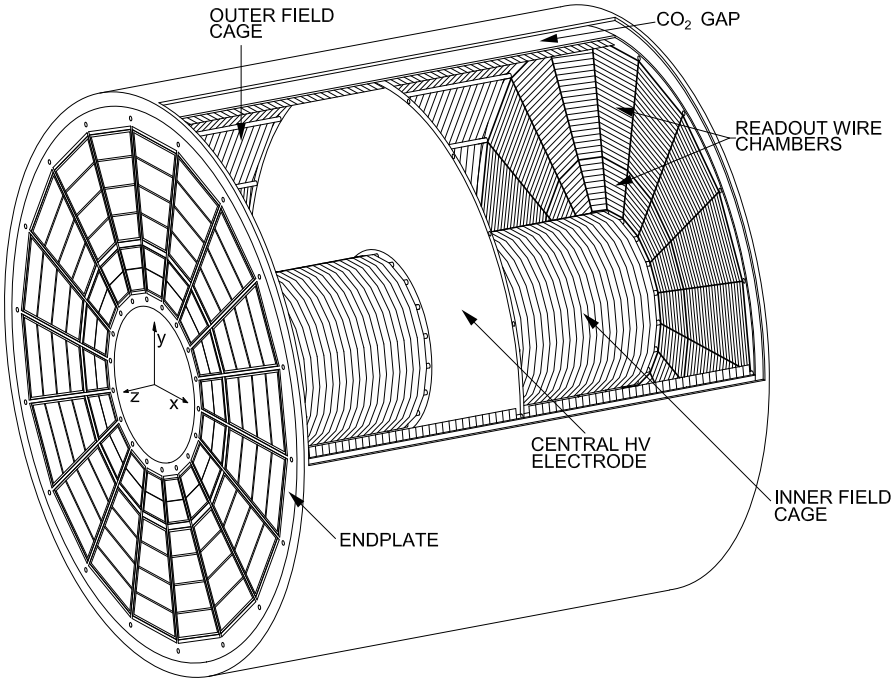


Figure 1.10: 3D view of the TPC field cage. Figure from [Alm10].

particle detected by one of the VZERO counters or by the SPD in coincidence with passing bunches. The SDD and SSD measure the specific energy loss dE/dx of traversing particles for PID. The ITS is used for tracking in the particle production analysis in Chapter 7.

The TPC [Del00b, Alm10] is the main tracking and PID device. Its active volume covers a radial range from 0.85 m to 2.47 m and a length of 5.1 m along the beam axis. It has acceptance in $|\eta| < 0.9$ (covering full radial range) and full azimuth. The drift volume, filled with a Ne–CO₂–N₂ (85.7% – 9.5% – 4.8%) gas mixture, is split by a high voltage central membrane (Fig. 1.10). The readout plane at each end cap consists of 159 pad rows with position resolution in the $r\phi$ -direction about 1100 μm to 800 μm from the inner to the outer radius. The resolution along the beam axis is between 1250 μm and 1100 μm . The measured dE/dx signal is the truncated mean signal with the truncation fraction 0.6 (see Chapter 5 for a discussion on the truncated mean signal in general). More discussions about the TPC tracking can be found in Chapter 2 and about the PID in Chapter 6. It is also used for tracking and PID in the particle production analysis in Chapter 7.

The TRD [Cor01, Aam08, And12] is optimized for the detection and identification of electrons. It also provides tracking and electron- and jet-triggers. It is a cylindrical detector system located in a radial position between 2.9 and 3.7 m and segmented in 6 layers. It has full azimuthal coverage in 18 super-modules and a polar coverage $45^\circ < \theta < 135^\circ$ in 5 stacks (Fig. 1.11). Individual TRD chamber consists of a 4.8 cm thick layer of fibers/-foam sandwich radiator and a drift chamber filled with Xe–CO₂ (85%–15%). The depths of the drift and amplification regions are 3 cm and 0.7 cm respectively (Fig. 1.12 (a)). The induced charges are readout by cathode pads which have a typical size of $0.7 \times 8.8 \text{ cm}^2$. The readout samples the signals in 100 ns time bins. A charged particle loses energy in primary collisions with gas atoms by ionization. Energetic ones with Lorentz factor γ

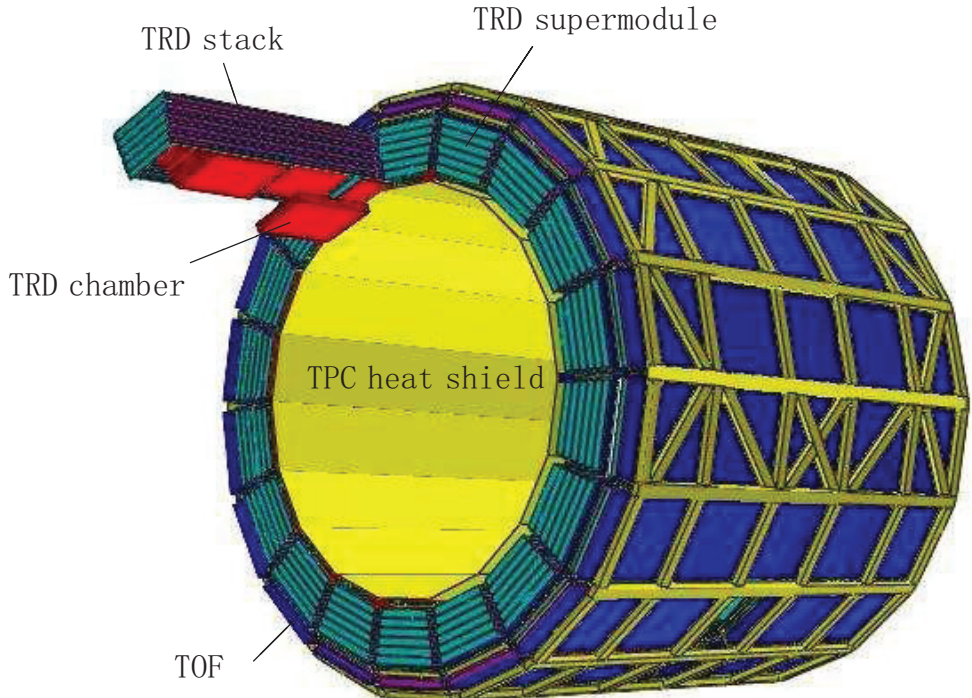


Figure 1.11: The layout of the TRD. Figure from [And12].

above 10^3 in addition induce transition radiation (TR) with an emission angle with respect to the particle momentum $\theta_{\text{TR}} \simeq 1/\gamma$ [Ber12] when passing through the radiator. The radial positions of the primary clusters of energy deposit are reconstructed from the drift time (Fig. 1.12). Therefore, besides the energy loss measurement, the TRD is also used for momentum determination. The TRD signal is the subject of Chapters 3, 4 and 5.

The TOF [Del00a, Aam08] detector is at the radial position between 370–399 cm from the beam axis. It consists of 18 azimuthal sectors, each containing five modules segmented along the beam axis. The measured time of flight of traversing particles from the vertex (Fig. 1.13) is used for PID. A new method to combine the TOF and TPC signals is discussed in Section 6.5 and used in the particle production analysis in Chapter 7.

1.4 Outline of this thesis

This thesis is organized as follows (see connections between chapters in Fig. 1.14). Chapter 2 discusses the newly developed cosmic combined track fit. Chapter 3 describes the TRD signal in a general statistical approach. In Chapter 4, using the methods developed in Chapters 2 and 3, the observation of TR induced by cosmic muons is reported. Chapter 5 discusses the truncated mean signal of the TRD, which is developed as a new method exploring the limit of the TRD PID. Chapters 6 and 7 focus on the analysis of particle production with a novel method – the TPC coherent fit. Detailed discussions on the observed baryon anomaly and nuclear modification are presented. The production of identified particles in jets are also discussed. In Appendix A, the measurement of exclusive central production of $\pi^+\pi^-$ in ALICE is mentioned.

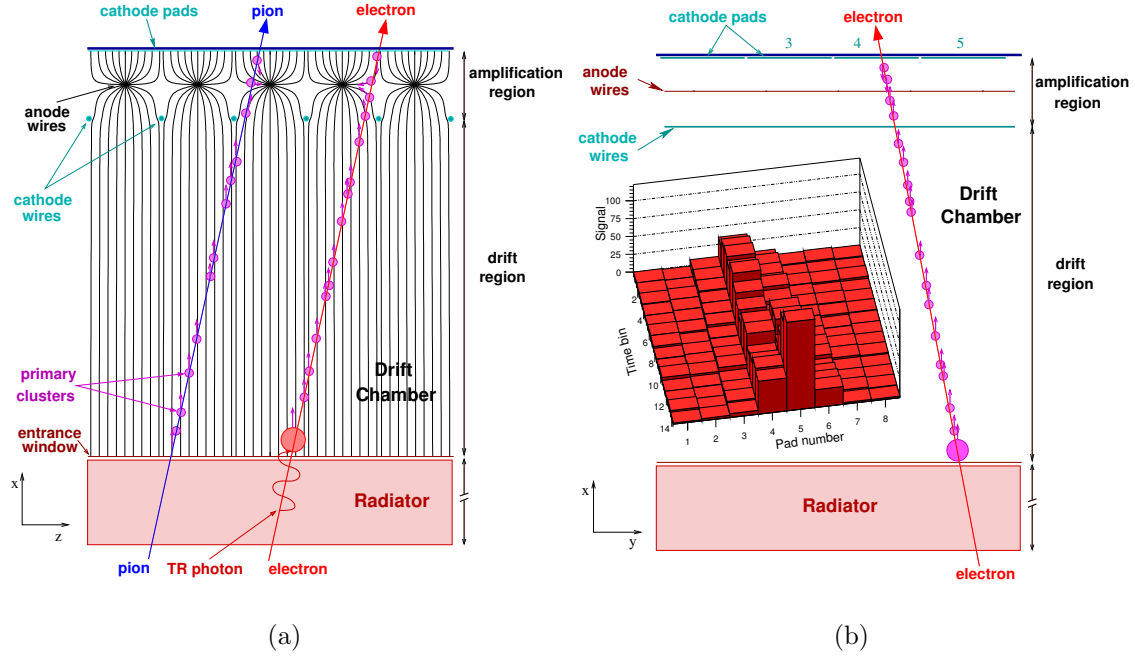


Figure 1.12: Cross-sectional view of a TRD module in (a) rz -plane and (b) $r\phi$ -plane. Figures from [And12].

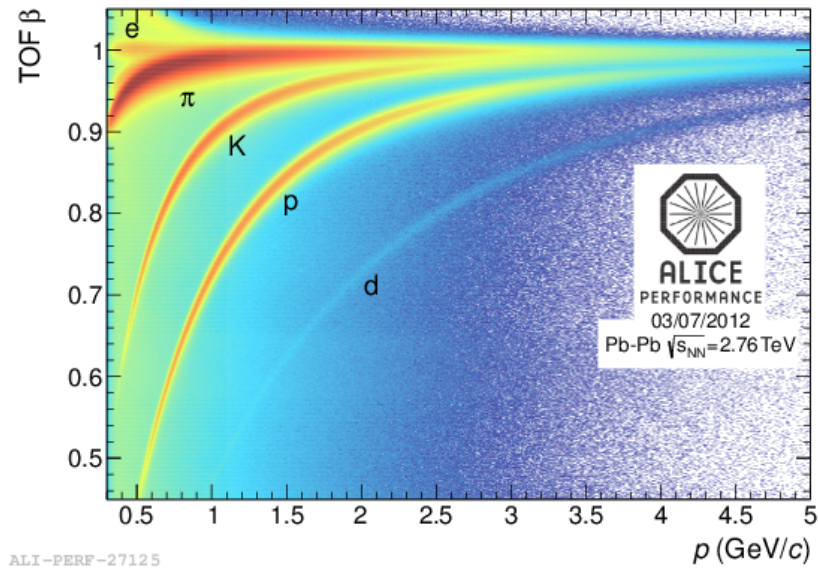


Figure 1.13: The particle velocity β (in unit of the speed of light) measured by TOF as a function of the momentum.

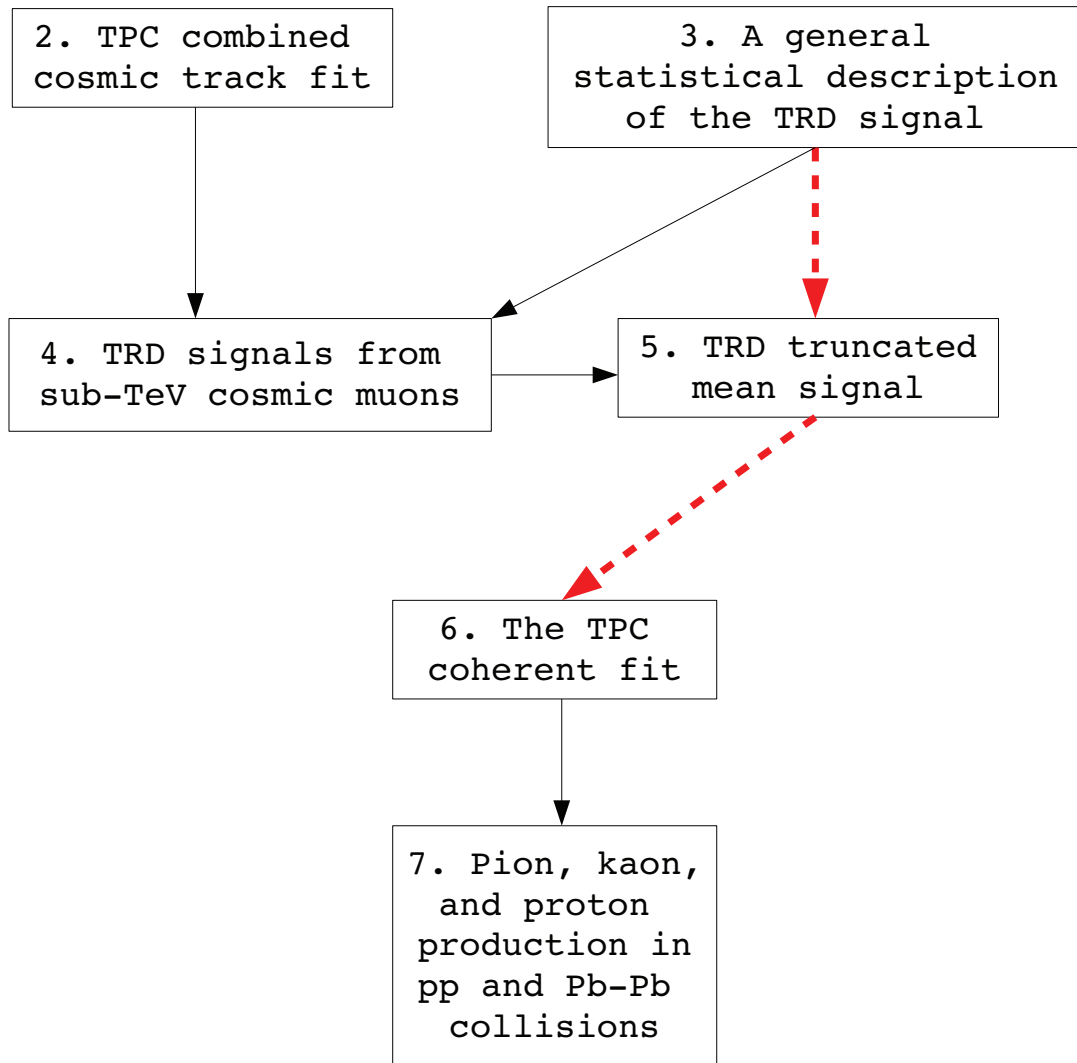


Figure 1.14: Connections between chapters. Black arrows indicate direct dependency in terms of machinery. Red dashed arrows represent logical connections following which the techniques involved can be understood in a general framework based on the fact that the qualitative properties of the TPC signal is the same as for the TRD without transition radiation.

Chapter 2

TPC combined cosmic track fit

In order to improve the ALICE tracking capability for TeV cosmic particles¹, a dedicated track fit project is developed in this work. In this chapter the description of the procedure and the resulting momentum resolution are discussed.

Cosmic particles traverse the TPC volume. In the standard tracking [Aam08], a single cosmic particle is reconstructed as two individual tracks assuming collision geometry. An optimization is seen if both tracks, whose underlying degrees of freedom are the ionization clusters reconstructed by the TPC, are combined into a single track. Because the accuracy of the momentum measurement depends on the lever arm of the track and the number of coordinate measurements, an improvement of about 10 times better resolution is foreseen according to the scaling behavior of the p_t resolution (for $p_t > 10 \text{ GeV}/c$ where multiple scattering can be ignored)

$$\sigma_{\frac{1}{p_t}} \sim \frac{\sigma_x}{BL^2}, \quad (2.1)$$

where $\sigma_{\frac{1}{p_t}}$ is the $1/p_t$ resolution, σ_x is the spatial resolution of the tracking parameters which depends on the number of coordinate measurements N as

$$\sigma_x \propto \frac{1}{\sqrt{N}}, \quad (2.2)$$

L is the lever arm of the track and B is the longitudinal magnetic field strength which is 0.5 T except otherwise explicitly stated. As the combined track doubles the number of coordinate measurements and triples the lever arm², the momentum resolution is improved by a factor of $3^2\sqrt{2} \simeq 13$. Integrated over geometry, this number is about 10, taking into

¹There were actually two physics motivations in this work. One was for the study of the TRD signal (Chapter 4 and 5). The other was to observe neutrinos using TPC. Muons from neutrino scattering in the earth come from below ground. When they traverse the ALICE muon filter (the “**ABSORBER**” in Fig. 1.9) they lose a significant amount of energy. If the momentum resolution is so good that the difference between the track momenta before and after crossing the muon filter can be resolved, the direction of the traversing muons can be determined. Identifying up-going muons would be the signature of neutrino detection at ALICE. First study using the developed cosmic track fit shows no positive results.

²The cross section of the TPC is an annulus with inner and outer radius 0.8 and 2.5 m, respectively (see Section 1.3). The maximum lever arms of the standard track and the combined track are 1.7 and 5 m respectively.

account tracks that do not pass through the TPC inner wall but only remain inside the TPC volume.

Another improvement can be achieved by considering the energy loss used in the track fit. In the standard reconstruction the energy loss is wrongly assigned for cosmic tracks because the direction of the propagation, i.e. the sign of the energy loss, is reversed for the upper tracks with respect to the case in collisions. On the other hand, due to the overburden above ALICE the cosmic rays observed are predominately muons. The energy loss in the combined track fit can be further specified as from muons.

2.1 Implementation

The algorithm of the combined track fit can be summarized as the following stages (for technical documentation see [[Lu11](#)]).

1. An event after standard reconstruction is read in. Reconstructed tracks are looped over. Only those tracks fulfilling minimum quality cuts are selected.
2. Double loop of the selected tracks from the previous step. Select cosmic track pair according to the absolute difference and the pull between the track parameters of the pair candidates.
3. The clusters of the selected track pair are combined and fit by a dedicated cluster-track fitting program (see below). In the end, the parameters of the full cosmic track are stored.

The cluster-track fitting program is based on the existing ALICE Kalman-filter algorithm (cf. [[Bil84](#)] and Section 8.1.2 in [[Aam08](#)]) which dynamically updates the track parameters as the clusters are visited one by one and the difference between the predicted and measured cluster coordinates is collected. The program drives the propagation through all clusters of the combined track pair, and takes into account the energy loss correctly.

The first benchmark of the project is the flow of statistics: the statistics of the collected data sample should be maximally preserved. As is shown in Table 2.1, the loss of nominal statistics³ is about 7% (for TOF back-to-back trigger, events with track multiplicity 2) which is acceptable for general purpose.

The characteristics of the combined cosmic tracks (TOF back-to-back trigger, events with all track multiplicities) is as follows:

- The number of clusters is about 290 ± 20 , out of a maximum of 318.
- The lever arm sharply peaks at about 490 cm.
- The mean and RMS⁴ of $\chi^2/N_{\text{cluster}}$ are about 3.0 and 1.0 respectively.
- The double counting rate (ambiguity in forming a cosmic track from any two standard tracks in events with multiplicity larger than two) is about 0.1%.

³The full sample contains non-usable statistics about 5% which is rejected in stage 1.

⁴The use of “RMS” follows the convention in the community. Throughout this work, the RMS of a random variable x is defined as the standard deviation $\sigma_x = \sigma(x) = \sqrt{\langle x^2 \rangle - \langle x \rangle^2}$.

stage	loss (%)
1	
reject kink daughter	0.8
TPC re-fit	0.2
TPC number of findable cluster $\neq 0$	0.1
findable ratio > 0.5	3.4
has TPC seeds in ESDfriends	0.2
2	
correlation between ϕ	0.7
correlation between θ	0.8
pull cuts, absolute cuts on track parameters	0.2
3	
separation of global y-coordinates of the two standard tracks	0.3
cut on the combined lever arm > 350 cm ($\sim 250\sqrt{2}$ cm)	0.4
full propagation	0.1
cut on $\chi^2/N_{\text{cluster}}$	0.1
all others (e.g. protections against small number of clusters)	0.2
total	7

Table 2.1: Flow of loss of statistics in each step of the combined cosmic track fit. Data was taken in May–June 2011 with 0.5 T B-field and TOF back-to-back trigger. Only events with 2 standard tracks are used.

2.2 Momentum resolution

The momentum resolution is characterized by the $1/p_{\text{T}}$ resolution. As can be seen in Eq. 2.1, $1/p_{\text{T}}$ is directly related to the coordinate measurement, which in general has the following sources of uncertainties [Alm10]:

1. spatial resolution limited by the diffusion of the drift charges,
2. multiple scattering (negligible at high momentum),
3. mis-alignment,
4. systematics of the B- and E-fields in the detector volume.

The first two effects induce symmetric smearing, while the latter two introduce bias and distortion. In the high momentum limit, σ_x , and therefore $\sigma_{\frac{1}{p_{\text{T}}}}$, is a finite constant. The conventional definition of the momentum resolution $p_{\text{measured}}/p_{\text{reference}} - 1$ (given an independently measured reference momentum) is equivalent to

$$\frac{\sigma_{p_{\text{T}}}}{p_{\text{T}}} = p_{\text{T}} \frac{\sigma_{p_{\text{T}}}}{p_{\text{T}}^2} \sim p_{\text{T}} \sigma_{\frac{1}{p_{\text{T}}}}, \quad (2.3)$$

which diverges with large p_{T} and is not suitable when the limit of the tracking capability is probed. Moreover, the difficulty in determining the momentum resolution for the

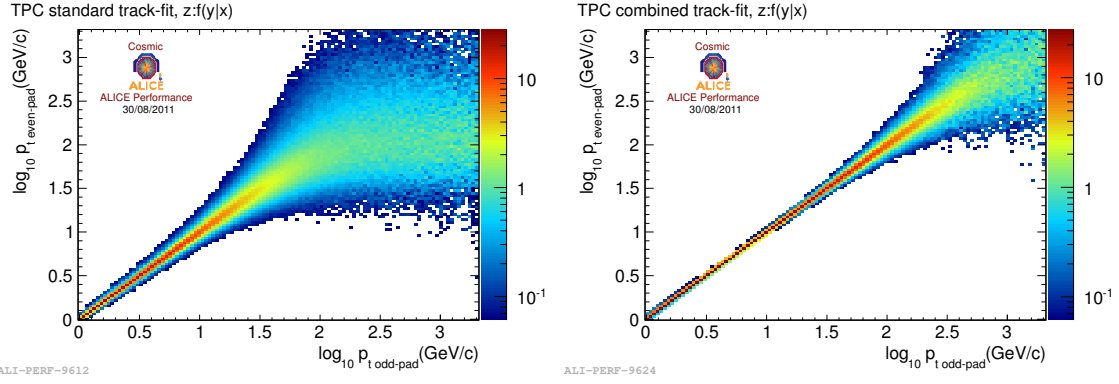


Figure 2.1: Correlation between p_T measured by even- and odd-pads separately. For each x-slice the distribution is normalized to unity so that the interpretation of the z-coordinate is the conditional probability of a p_T from even-pads given a p_T from odd-pads. The *left* panel is using the standard track fit on cosmic tracks of half length, while the *right* one is using the combined track fit on cosmic tracks of full length.

combined cosmic track fit is that there is no proper reference momentum⁵. For a practical estimate, the following approach is developed.

As is discussed in the previous section, the track fit program in general visits each TPC cluster and fits the track. (Quasi-)Independent measurements of the momentum for a given track can be made by fitting separately the clusters read out by the pads on the odd rows and on the even rows. The correlation between these two measurements is shown in Fig. 2.1. As can be seen, with the standard track fit the correlation is lost at high momentum and the measured momentum is entirely subject to random fluctuation, while for the combined track fit the correlation is much improved.

Because the even- and odd-pads, by which the ionization clusters of a given track are read out, are locally connected, the correlation, equivalently the difference, between their measures is not sensitive to global systematic effects like mis-alignment or B- and E-field systematics. From the spread of the correlation, one can only estimate the momentum resolution due to spatial resolution and at low momentum also to multiple scattering. Nevertheless, the accuracy of this approximate estimation of the momentum resolution can be checked for the case of the standard track fit because an independently measured reference momentum can be provided by the combined track fit. The comparison is shown in Fig. 2.2. It can be seen⁶ that the spread of the even-odd correlation well approximate the standard-combined (which is interpreted as the “measured-true”) correlation. The expected difference of the spread at $p_T > 10 \text{ GeV}/c$ is due to the increasing influence of the global systematic effects on measuring nearly straight trajectories. Due to the scaling behavior between the standard and combined track fit, the conclusion above for

⁵The TRD can serve as a reference detector using its signal-momentum correlation. But since this very correlation is to be studied with a precise momentum measurement provided by the cosmic track fit, TRD is only used for a consistency check in this work.

⁶In Fig. 2.2 the correlation between the upper and lower track partners by the standard track fit is also presented. It overestimates the resolution because the irrelevant intrinsic difference between the momenta and qualities of the upper and lower tracks due to the energy loss, the lever arms and the numbers of clusters is also taken into account in this estimate.

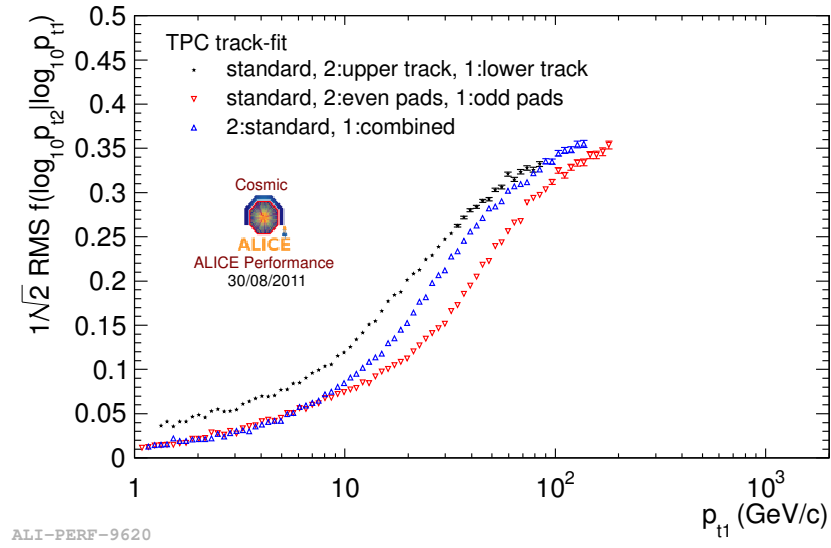


Figure 2.2: RMS of different correlations: even-odd, standard-combined.

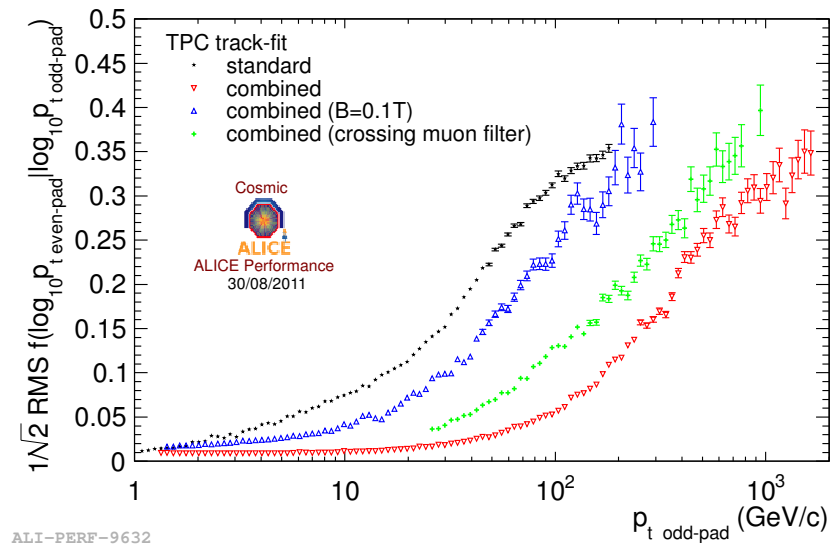


Figure 2.3: RMS of the even-odd correlation for the standard and combined track fits. Cosmic data taking at $B = 0.1$ T and cosmic particles in full acceptance including the region of the muon filter (see Footnote 1) are also compared.

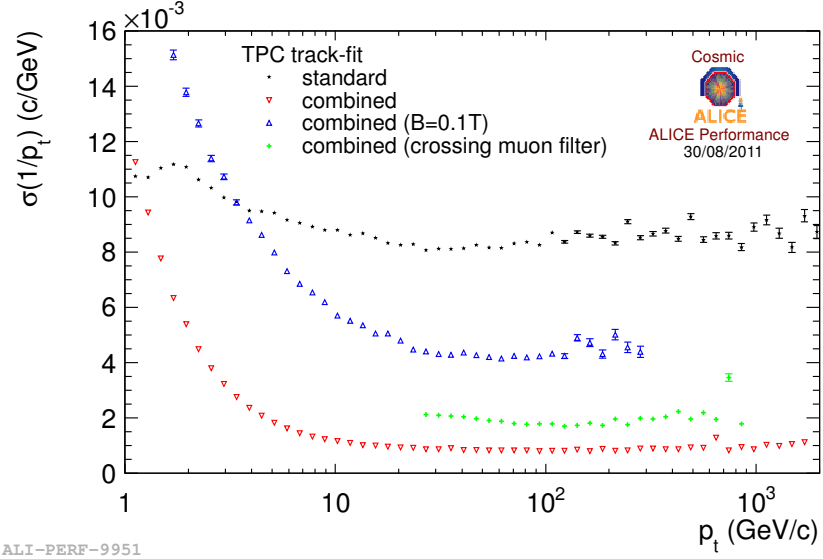


Figure 2.4: Inverse- p_{T} resolution for the standard and combined track fits.

the former is directly applicable to the latter. Figure 2.3 shows the even-odd correlation for different track fits.

The $1/p_{\text{T}}$ resolution is calculated as

$$\sigma_{\frac{1}{p_t}} = \frac{1}{2}\sigma \left(\frac{1}{p_{\text{T even-pad}}} - \frac{1}{p_{\text{T odd-pad}}} \right), \quad (2.4)$$

where the factor $1/2$ counts for the inflation due to on the one hand the addition of two uncorrelated measurements and on the other hand the reduction of the number of clusters compared to the full track fit. The results for different track fits are shown in Fig. 2.4. As can be seen at $p_{\text{T}} \gtrsim 1 \text{ GeV}/c$ where multiple scattering starts to be suppressed, the improvement for the combined track fit due to the increase of the number of clusters and the lever arm becomes significant. The p_{T} resolution is estimated in Table 2.2 using Eq. 2.3. The estimate for the standard track fit is consistent with [Alm10]. It is interesting to note that the results, including also the cosmic data taking at $B = 0.1 \text{ T}$, show a scaling behavior at high p_{T} , consistent with the expectation according to Eq. 2.1. The asymptotic value of $\sigma_{\frac{1}{p_t}}$ for the combined track fit in the high p_{T} limit is $8.1 \times 10^{-4} (\text{GeV}/c)^{-1}$.

p_{T} (GeV/c)	1	10	100
standard track fit	1.1%	8.7%	(not defined)
combined track fit	1.3%	1.2%	8.1%

Table 2.2: Transverse momentum resolution for the TPC standard and combined track fits.

As an extension of the discussion, it is noted that the total momentum resolution is similar to the p_{T} resolution, as can be seen by comparing Fig. 2.5 to Fig. 2.3, where the difference is mostly due to the change of variables.

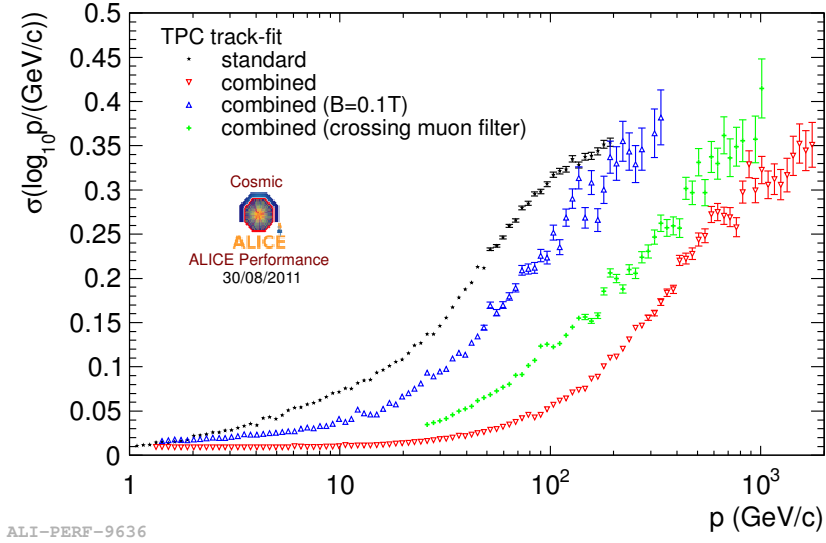


Figure 2.5: RMS of the even-odd correlation for the total momentum, where $\sigma(\log_{10} p / (\text{GeV}/c))$ stands for $(1/\sqrt{2})\text{RMS}f(\log_{10} p_{\text{event-pad}} | \log_{10} p_{\text{odd-pad}})$ as in Fig. 2.3 but for the total momentum.

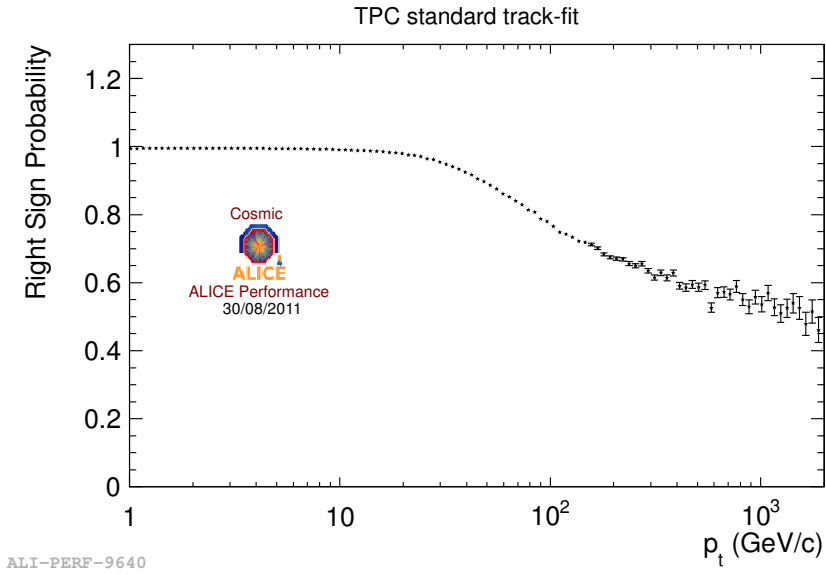


Figure 2.6: Right sign probability (see definition in text) for the standard track fit as a function of p_{T} .

The combined track fit can be further used as a reference measurement for the track sign, i.e the charge of the particle. Figure 2.6 shows the right sign probability for the standard track fit defined as the fraction of standard tracks with correct signs with respect to the reference measurement provided by the combined track fit. At $p_{\text{T}} = 50 \text{ GeV}/c$, 10% of the tracks are sign-flipped due to the limited p_{T} resolution.

Chapter 3

A general statistical description of the TRD signal

A particle traversing the ALICE TRD loses energy in collisions with the gas atoms. For particles with Lorentz factor γ roughly larger than several hundred, additional energy loss takes place – transition radiation (TR) will be emitted along the flight direction of the particle when it passes through the radiator. The TR photons which enter the gas chamber will deposit their energy in the gas volume. After a trigger signal both types of energy loss will be collected. The TRD signal [Cor01, Aam08] – the integrated charge over all drift time corrected for a non-perpendicular incident angle – kinetically depends only on the velocity of the particle and therefore provides separation power among different particle species. This chapter provides a general statistical description of the TRD signals with and without the TR component.

3.1 The Landau distribution

In his seminal paper [Lan44], Landau derived the energy loss distribution function which gives the probability density that a particle traversing a layer of material loses an amount of energy due to collisional ionization. Here this so-called Landau distribution function will be derived in a more general statistical framework which considers the energy transfer between the particle and the medium to be a general process where information of any kind is transferred. It is hoped that in this framework the basic assumptions and the physical content of the distribution could be illustrated in a systematic and universal way.

Consider a particle traversing a slice of material. Assume that the particle either has no interaction with the medium at all or interacts only once with probability τ . Denote an additive observable associated with the interaction as x with $x \in D \supset \{0\}$, where D is the domain of x . x can be the energy transfer of the particle, the azimuthal deflection angle¹, or in the trivial case the number of interactions. Denote the distribution of x as $\eta(x)$ (with normalization $\int_D \eta(x)dx = 1$) in case of an interaction. Here $\eta(x)$ is called

¹The polar deflection angle is correlated to the energy transfer. Its distribution can be deduced from that of the latter.

the distribution kernel. In the case where x is the number of interactions, by definition

$$\eta(x) = \delta(x - 1), \quad x \geq 0, \quad (3.1)$$

where $\delta(x)$ is the Dirac delta function; in the case of an isotropic azimuthal deflection angle²,

$$\eta(x) = \frac{1}{2R}, \quad -R < x < R, \quad R \rightarrow +\infty, \quad (3.2)$$

and in the case of the energy transfer,

$$\eta(x) = \frac{d\sigma(x)/dx}{\int d\sigma}, \quad x \geq 0 \quad (3.3)$$

where σ is the interaction cross-section. With the details of the interaction encapsulated in $\eta(x)$, the total probability density of x , regardless of whether an interaction takes place or not, reads

$$f(x) = (1 - \tau)\delta(x) + \tau\eta(x), \quad (3.4)$$

with $\int_D f(x)dx = 1$ by construction.

Consider now a particle traversing m slices with observable x_i and probability densities $f_i(x_i)$ where i indicates the slice dependence. The sum of the observables is

$$X = \sum_{i=1}^m x_i \quad (3.5)$$

with the corresponding probability density function $F(X)$. Assuming that x_i are uncorrelated, we have

$$F(X) = (f_1 * f_2 * \dots * f_m)(X), \quad (3.6)$$

where “ $*$ ” denotes convolution. Taking an integral transform, either Fourier or Laplace depending on which one is more convenient, on both sides, it reads

$$\mathcal{L}[F] = \mathcal{L}[f_1 * f_2 * \dots * f_m] = \prod_{i=1}^m \mathcal{L}[f_i]. \quad (3.7)$$

With a further assumption that all slices are identical, it reduces to

$$\mathcal{L}[F] = \{\mathcal{L}[f]\}^m. \quad (3.8)$$

Because

$$\mathcal{L}[f](s) = (1 - \tau)\mathcal{L}[\delta](s) + \tau\mathcal{L}[\eta](s) = 1 + \tau[\tilde{\eta}(s) - 1], \quad (3.9)$$

where $\mathcal{L}[\delta](s) = 1$ and

$$\tilde{\eta}(s) \equiv \mathcal{L}[\eta](s), \quad (3.10)$$

²An isotropic distribution of a periodic number has to be defined on the whole real axis.

Equation 3.8 reads

$$\mathcal{L}[F](s) = \{1 + \tau [\tilde{\eta}(s) - 1]\}^m. \quad (3.11)$$

The quantity $N \equiv \sum_{i=1}^m \tau_i$ is the expected number of interactions in the slices. In the limit $m \rightarrow \infty$ with N fixed, the binomial assumption leading to Eq. 3.4 is equivalent to the statement that the interaction is exclusive in time which is generally justified. The problem now is to determine $F(X)$ for the interaction in the bulk of slices in this limit. Using $N = \tau m$ (according to the assumption of identical slices) and taking the limit $m \rightarrow \infty$, we have

$$\mathcal{L}[F](s) = \left\{ 1 + \frac{N}{m} [\tilde{\eta}(s) - 1] \right\}^m = e^{N[\tilde{\eta}(s)-1]}. \quad (3.12)$$

The solution of $F(X)$ for a general $\eta(x)$ is obtained by taking the inverse transform:

$$F(X) = \mathcal{L}^{-1}\{\mathcal{L}[F]\}(X) = \mathcal{L}^{-1}\{e^{N[\tilde{\eta}(s)-1]}\}(X). \quad (3.13)$$

On expanding the exponential function in Eq. 3.12, that is,

$$\mathcal{L}[F](s) = e^{-N} \sum_{k=0}^{\infty} \frac{N^k}{k!} \tilde{\eta}^k(s), \quad (3.14)$$

Equation 3.13 becomes

$$F(X) = \sum_{k=0}^{\infty} P(k; N) \mathcal{L}^{-1}[\tilde{\eta}^k(s)](X) \quad (3.15)$$

$$= \sum_{k=0}^{\infty} P(k; N) F_k(X), \quad (3.16)$$

where $P(k; N) = e^{-N} N^k / k!$ denotes the Poisson probability of k with mean N and $F_k \equiv \underbrace{\eta * \eta * \dots * \eta}_k$ is the distribution of X in case of k interactions.

The following discussions first show the exact solutions of $F(X)$ in the cases of x being the number of interactions and the isotropic azimuthal deflection angle, and then discuss the approximate solution for the energy transfer distribution.

3.1.1 Distribution of the number of interactions

In the case that x is the number of interactions, $\eta(x) = \delta(x - 1)$. Taking the Laplace transform,

$$\tilde{\eta}(s) = \int e^{-sx} \delta(x - 1) dx = e^{-s}, \quad (3.17)$$

we have

$$\tilde{\eta}^k(s) = e^{-ks}, \quad (3.18)$$

whose inverse transform reads

$$\mathcal{L}^{-1} [\tilde{\eta}^k(s)](X) = \frac{1}{2\pi i} \int_{-i\infty}^{+i\infty} e^{sX - ks} ds = \delta(X - k). \quad (3.19)$$

Therefore the solution of $F(X)$ using Eq. 3.15 is

$$F(X) = \sum_{k=0}^{\infty} P(k; N) \delta(X - k), \quad (3.20)$$

which is the Poisson distribution defined in the real domain. Therefore we see that the assumptions that

- (1) there is no correlation among interactions,
- (2) individual interactions are identical,
- (3) and the interaction is exclusive in time,

lead to a Poisson distribution of the number of interactions. In fact, the Poissonian nature of the problem is readily illustrated by Eq. 3.16.

3.1.2 Distribution of the azimuthal deflection angle

The procedure is similar to the case for the number of interactions. For x being the isotropic azimuthal deflection angle, taking the Fourier transform of Eq. 3.2, we have

$$\begin{aligned} \tilde{\eta}(s) &= \lim_{R \rightarrow \infty} \int_{-R}^{+R} e^{-isx} \frac{1}{2R} dx = \lim_{R \rightarrow \infty} \frac{\sin Rs}{Rs} \\ &= \begin{cases} 1, & s = 0 \\ 0, & s \neq 0 \end{cases}. \end{aligned} \quad (3.21)$$

It follows that X is also isotropic (as it should be) because $\tilde{\eta}^k(s) = \tilde{\eta}(s)$ and therefore $F_k(X) = \eta(X) = 1/(2R)$ which leads to $F(X) = 1/(2R) \sum_{k=0}^{\infty} P(k; N) = 1/(2R)$ with $R \rightarrow \infty$ from Eq. 3.16.

3.1.3 Distribution of the energy transfer

In the case of the energy transfer from the particle to the medium due to collisions³, $\eta(\varepsilon)$ is the normalized differential interaction cross-section (Eq. 3.3). Here the Rutherford scattering cross-section with the $1/\varepsilon^2$ dependence is used:

$$\eta(\varepsilon) = \theta(\varepsilon - \varepsilon_0) \frac{A}{\varepsilon^2}, \quad (3.22)$$

³From here on ε and E instead of x and X will be used as the single and total energy transfer, respectively, to represent the physical meaning of the quantities.

where $\theta(x)$ is the step function⁴

$$\theta(x) = \begin{cases} 0 & \text{if } x < 0 \\ 1 & \text{otherwise} \end{cases} \quad (3.23)$$

which provides a cut-off ϵ_0 to avoid the unphysical t-channel singularity corresponding to soft photon exchanges. The normalization constant A is determined to be $A = \epsilon_0$ by requiring $\int_{-\infty}^{\infty} \eta(\varepsilon) d\varepsilon = 1$. The Laplace transform of $\eta(\varepsilon)$ is

$$\begin{aligned} \tilde{\eta}(s) &= \int_{\epsilon_0}^{\infty} e^{-s\varepsilon} \frac{\epsilon_0}{\varepsilon^2} d\varepsilon = \int_1^{\infty} \frac{e^{-zt}}{t^2} dt = E_2(z) \\ &= z \ln z + (C - 1)z + 1 + o(|z|^2), \quad \text{Re}\{z\} > 0, \end{aligned} \quad (3.24)$$

where the second line is obtained via change of variables $t = \varepsilon/\epsilon_0$, $z = s\epsilon_0$ and $E_2(z)$ is the exponential integral $E_n(z)$ with $n = 2$ (cf. for example [Abr72]) and $C = 0.57721\dots$ is Euler's constant. Assuming the smallness of z in the significant integration region of Eq. 3.13 and then neglecting the $o(|z|^2)$ term in Eq. 3.24, Eq. 3.13 then becomes

$$\begin{aligned} F(E) &= \frac{1}{2\pi i} \int_{c-i\infty}^{c+i\infty} \exp(sX + N[\tilde{\eta}(s) - 1]) ds \\ &= \frac{1}{2\pi i \epsilon_0} \int_{c-i\infty}^{c+i\infty} \exp\left(z \frac{E}{\epsilon_0} + N[z \ln z + (C - 1)z]\right) dz \\ &= \frac{1}{2\pi i \epsilon_0 N} \int_{c-i\infty}^{c+i\infty} \exp\left(\left[\frac{E}{\epsilon_0 N} - (\ln N - C + 1)\right] u + u \ln u\right) du \\ &= \frac{1}{2\pi i \xi} \int_{c-i\infty}^{c+i\infty} e^{\lambda u + u \ln u} du, \quad c > 0, \end{aligned} \quad (3.25)$$

with change of variables $u = Nz$ and

$$\xi \equiv \epsilon_0 N, \quad (3.26)$$

$$\begin{aligned} \lambda &\equiv \frac{E}{\epsilon_0 N} - (\ln N - C + 1) \\ &= \frac{E}{\xi} - \left(\ln \frac{\xi}{\epsilon_0} - C + 1\right) \\ &\equiv \frac{E - \Delta}{\xi}. \end{aligned} \quad (3.27)$$

This is the Landau distribution in its original form. It depends on the expected number of interactions N and the cut-off ϵ_0 of the energy transfer, or equivalently on ξ and Δ . Fig. 3.1 shows the Landau distribution with different parameters.

As a mathematical exercise, an alternative model of $\eta(\varepsilon)$ is to modify the small- E behavior instead of the sharp cut-off in Eq. 3.22 by an averaged probability:

$$\eta(\varepsilon) = \theta(\varepsilon)\theta(\epsilon_0 - \varepsilon)\frac{1}{2\epsilon_0} + \theta(\varepsilon - \epsilon_0)\frac{\epsilon_0}{2\varepsilon^2}. \quad (3.28)$$

⁴The behavior of $\theta(x)$ at $x = 0$ is not relevant here.

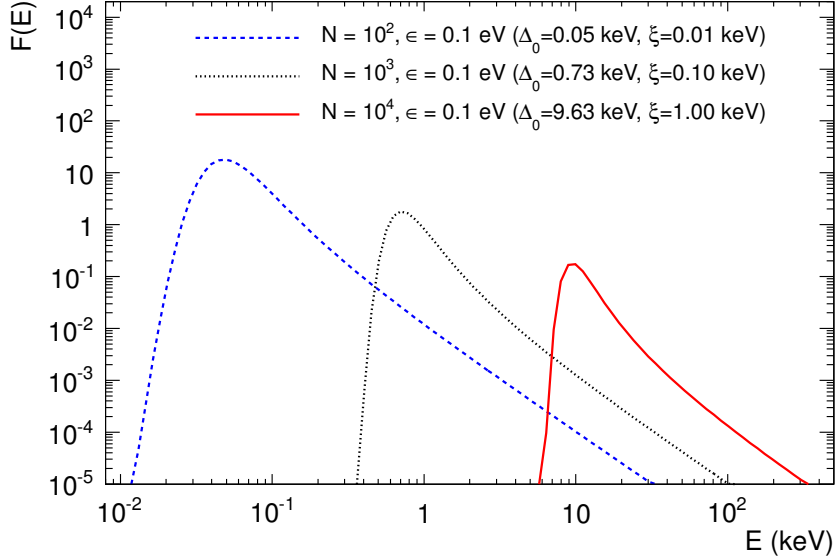


Figure 3.1: Landau distribution with different parameters. Eq. 3.25 is evaluated with the program ROOT [Bru97].

This leads to the same form as Eq. 3.25 but with different definitions of ξ and λ :

$$\xi \equiv \epsilon_0 \frac{N}{2}, \quad (3.29)$$

$$\begin{aligned} \lambda &\equiv \frac{E}{\epsilon_0 \frac{N}{2}} - \left(\ln \frac{N}{2} - C + \frac{3}{2} \right) \\ &= \frac{E}{\xi} - \left(\ln \frac{\xi}{\epsilon_0} - C + \frac{3}{2} \right). \end{aligned} \quad (3.30)$$

The model used by Landau was based on Livingston and Bethe's calculation (cf. [Lan44] and reference therein) with the following physical cut-off for Eq. 3.22:

$$\ln \epsilon_0 = \ln \frac{(1 - \frac{v^2}{c^2}) I^2}{2mv^2} + \frac{v^2}{c^2}, \quad (3.31)$$

where ϵ_0 is measured in electron volts, m is the mass of electron, v the velocity of the traversing particle, c the speed of light and $I = 13.5Z$ eV is a certain ionization potential with the atomic number Z of the material. For a minimum ionizing particle in xenon gas, ϵ_0 is about 0.1 eV. A general discussion about the cut-off can be found in [Jac99].

The Landau distribution, as we have seen so far, is based on further assumptions in addition to the previous Poissonian assumptions. The validity of the model and the assumed smallness of the $o(|z|^2)$ term in Eq. 3.24 limit the applicability of the distribution. The physical energy transfer cannot attain arbitrarily large values. There is a maximum transferable energy determined by the energy and mass of the traversing particle and the electron mass. Moreover the Poissonian assumption of identical interactions requires the energy transfer be so small that the change of the magnitude of the particle velocity is negligible. On the other hand, when the energy transfer is comparable to the ionization

potential of the atom, the atomic structure has to be taken into account. Finally, neglecting the $o(|z|^2)$ term requires that the cut-off is significantly small ($z = s\epsilon_0$). This is not always physically justified because the cut-off is determined by the ionization potential, see Eq. 3.31. In practice, some numerical form of Eq. 3.25 is used to fit the measured collisional ionization distribution, with ξ and Δ being treated as free parameters.

3.2 Distribution of the collisional ionization signal

In Section 3.1.3, the distribution kernel $\eta(\varepsilon)$ is taken to be the differential cross-section in the energy transfer ε (Eq. 3.22) and the resulting $F(E)$ (Eq. 3.25) describes the collisional ionization distribution of the traversing particle. Now we consider the distribution of the measured signal, which is subject to the fluctuation due to the efficiency of the ionized-charge collection and the symmetric fluctuations in the signal collection and amplification. The latter can be modeled as an addition of a Gaussian random variable to the collected signal⁵. In the following we discuss an approximate treatment of the first effect.

There are several reasons leading to the loss of the ionized charges. Firstly, after the electron-ion pairs are created during the collision between the projectile and the atoms, the ionized particles drift in the electric-magnetic field. They have certain probability to recombine with other oppositely charged particles, or to be attached to molecules like H₂O. Secondly, ionization electrons can be knocked out of the atom with large kinetic energies and they are the so-called δ -electrons. They may escape the detector volume or fail to be reconstructed. Thirdly, after the ionized charges are collected, their origins are reconstructed to form the trajectories of the projectile. This procedure, the so-called cluster attachment, has some inefficiency in associating correctly all charges to the corresponding track.

Denote the survival probability against these processes as P_s . The distribution kernel for the measured collisional ionization signal reads

$$\eta(q) = \int d\varepsilon \frac{d\sigma(\varepsilon)/d\varepsilon}{\int d\sigma} B(q; \frac{\varepsilon}{W}, P_s), \quad (3.32)$$

where q is the measured ionized charges, W is the mean energy needed to create an electron-ion pair, and

$$B(q; \frac{\varepsilon}{W} \equiv q_c, P_s) = \frac{q_c!}{q! (q_c - q)!} P_s^q (1 - P_s)^{q_c - q} \quad (3.33)$$

is the binomial probability of q with mean $q_c P_s$.

In case that the deficit in the charge collection is small, i.e. $1 - P_s \ll 1$, it is only when $q_c = q$ that $B(q; q_c, P_s)$ has non-negligible contribution to the integral in Eq. 3.32.

⁵This includes the noise and the fluctuation of the gas gain [Blu08]. The latter depends on the detailed properties of the electric field and the gas, and to a first approximation can be considered as a Gaussian fluctuation. In fact all Gaussian fluctuations, at both the cluster and the total signal levels, effectively combine as one single Gaussian fluctuation.

Therefore we have⁶

$$\begin{aligned}\eta(q) &\simeq W \frac{d\sigma(\varepsilon)/d\varepsilon}{\int d\sigma} \Bigg|_{\frac{\varepsilon}{W}=q} B(q; q, P_s) \\ &= W \frac{d\sigma(\varepsilon)/d\varepsilon}{\int d\sigma} \Bigg|_{\frac{\varepsilon}{W}=q} P_s^q \\ &= \eta_\varepsilon(q) e^{-\kappa q},\end{aligned}\tag{3.34}$$

where $\kappa = -\ln P_s > 0$ and $\eta_\varepsilon(q)$ is the collisional ionization distribution kernel, for example Eq. 3.22, with change of variable $\varepsilon \rightarrow q/W$. The Laplace transform of Eq. 3.34 is

$$\tilde{\eta}(s) = \tilde{\eta}_\varepsilon(s + \kappa),\tag{3.35}$$

where $\tilde{\eta}_\varepsilon = \mathcal{L}[\eta_\varepsilon]$. Note that generally P_s depends on the location of the ionization. Assuming the smallness of this dependency, which is justified when the inefficiency of the cluster attachment is dominant over other charge loss processes, Eq. 3.35 can be inserted into Eq. 3.13 which then reads

$$\begin{aligned}F(Q) &= \frac{1}{2\pi i} \int_{c-i\infty}^{c+i\infty} \exp\{sQ + N[\tilde{\eta}_\varepsilon(s + \kappa) - 1]\} ds, \\ &= e^{-\kappa Q} F_E(Q)\end{aligned}\tag{3.36}$$

$$= P_s^Q F_E(Q)\tag{3.37}$$

where Q is the total measured ionized charges and $F_E(Q)$ is the collisional ionization distribution, for example Eq. 3.25, with change of variable $E \rightarrow Q$. It shows that a small deficit in the charge collection leads to a geometric damping.

Figures 3.2 shows the measured collisional ionization distributions in the TRD from test-beam measurement [Bai06]. The distributions are well described by

$$F(Q) = \frac{1}{A} \int e^{-\kappa x} L(x; \Delta, \xi) G(Q; x, \sigma) dx,\tag{3.38}$$

where A is the normalization, $L(x; \Delta, \xi)$ is the Landau distribution of x with the parameters Δ and ξ (Eq. 3.25– 3.27), and $G(x; \mu, \sigma)$ is the Gaussian distribution with mean μ and standard deviation σ . In order to reduce the correlations between the parameters and eliminate the dimensions, the following parametrization is used in the fitting

$$F(Q) = p_0 \frac{\int \exp\left(-p_4 \frac{x}{p_1}\right) L(x; p_1, p_1 p_2) G(Q; x, p_1 p_3) dx}{\int \exp\left(-p_4 \frac{x}{p_1}\right) L(x; p_1, p_1 p_2) dx},\tag{3.39}$$

with

$$(p_1, p_2, p_3, p_4) \equiv (\Delta, \xi/\Delta, \sigma/\Delta, \kappa\Delta).\tag{3.40}$$

The parameters for pions and electrons of different momenta in the testbeam measurements are summarized in Fig. 3.3. It can be seen that

⁶The normalization has to be restored in the end, see Eq. 3.38.

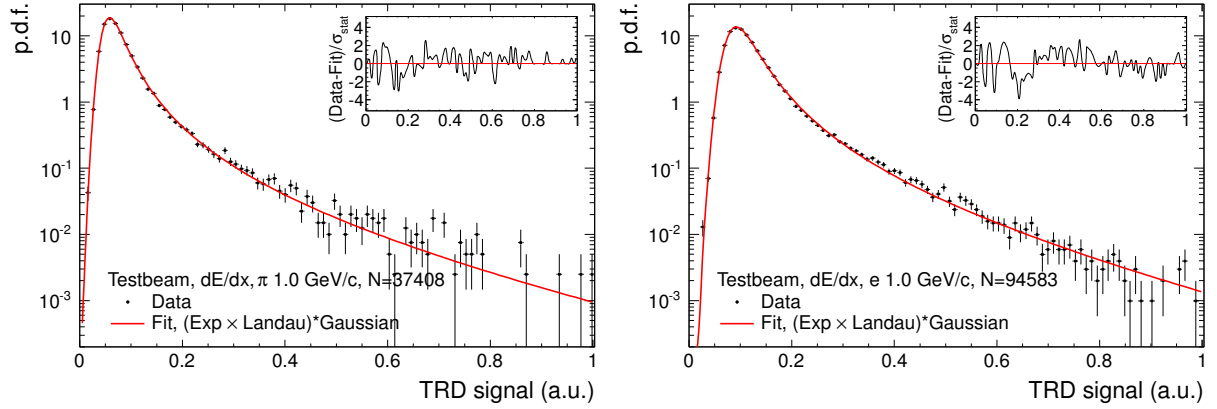


Figure 3.2: Distributions of measured collisional ionization (dE/dx) in TRD by pions (left) and electrons (right) with momentum $1 \text{ GeV}/c$. N is the statistics.

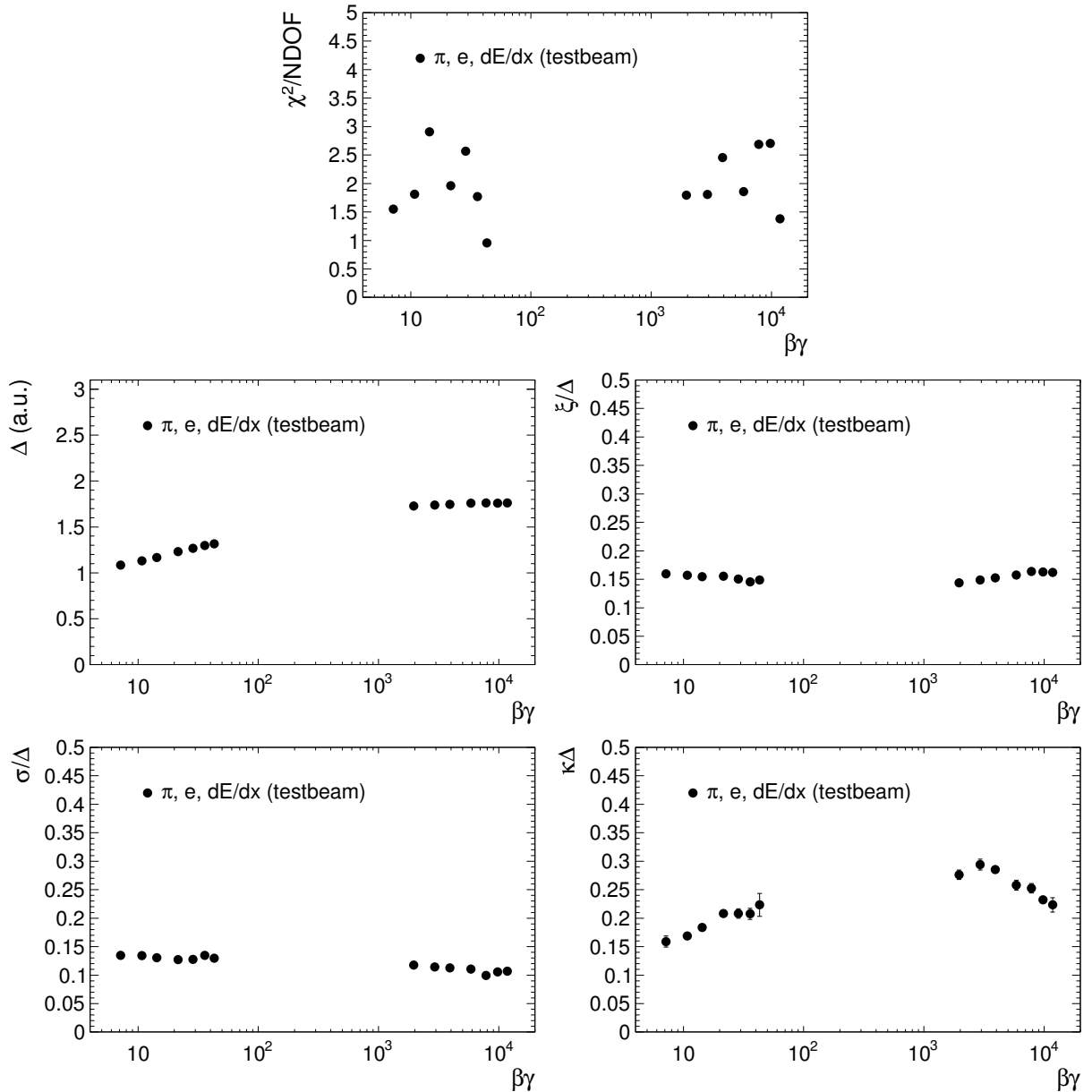


Figure 3.3: Summary of the fitting results for measured collisional ionization (dE/dx).

- χ^2/n_{DOF} lies between 1 and 3,
- ξ/Δ is almost flat as a function of $\beta\gamma$, which agrees with the expectation $1/(\ln N - C + 1)$ (Eq.3.27) from the Landau distribution , where $\ln N$ only has a slight kinematic dependence,
- σ/Δ is about 12%,⁷
- and the damping $e^{-\kappa\Delta} = P_s^\Delta$ is about $e^{-0.2} \simeq 0.8$, from which P_s can be derived:

$$P_s \simeq 0.8^{\frac{1}{\langle Q \rangle}}, \quad (3.41)$$

where $\langle Q \rangle$ is the expected physical number (following the definition $q = \varepsilon/W$) of the measured ionized charge. If $\langle Q \rangle = 10$, then the charge collection inefficiency is $1 - P_s \simeq 2\%$.

3.3 Distribution of the combined signal of collisional ionization and transition radiation

When the TR photons induced by particles with high Lorentz factor γ are collected in the TRD gas chamber, the TRD signal is the convolution of the measured collisional ionization (Eq.3.37) and the collected energy deposit from the TR photons. Instead of exploring the energy spectrum of the TR photons, it is interesting to note that the parametrization of Eqs. 3.39–3.40 is also applicable to this combined signal. This leads to a general and practical modeling of the full TRD signal including the TR component.

Figure 3.4 shows the distributions of the measured TRD signal with TR by electrons in the testbeam measurement [Bai06]. The fitting quality ($\chi^2/n_{\text{DOF}} \sim 3$) is slightly worse than that for the collisional ionization. Fig. 3.5 is a summary of the fitting results. As can be seen from the value of σ , the convolution with the Gaussian distribution in the parametrization is redundant. The fitting results remain the same without it.

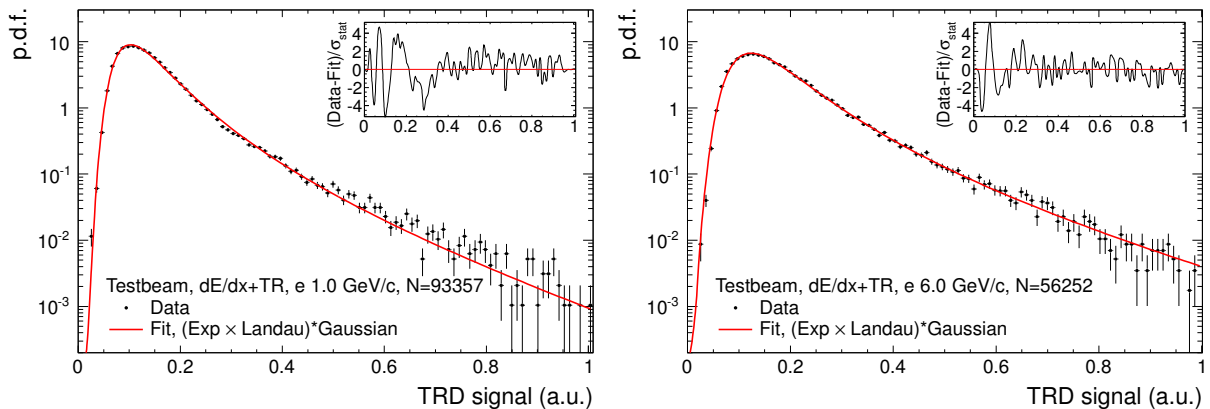


Figure 3.4: Distributions of measured TRD signal with TR component ($dE/dx+TR$) by electrons with momentum $1 \text{ GeV}/c$ (left) and $6 \text{ GeV}/c$ (right). N is the statistics.

⁷This includes Gaussian fluctuations at all levels. See Footnote 5.

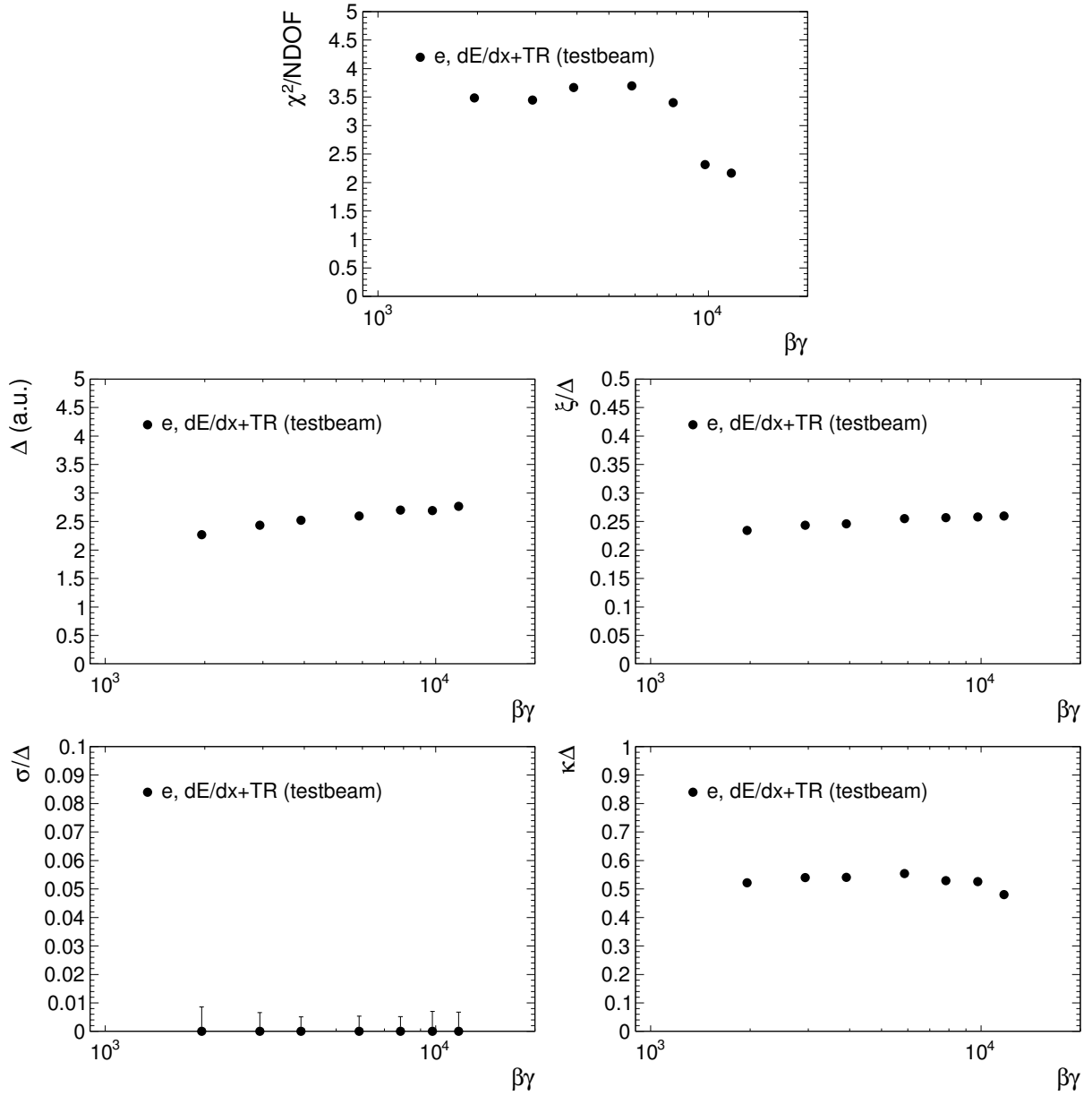


Figure 3.5: Summary of the fitting results for measured TRD dE/dx+TR signal. The fitted values of σ is consistent with zero, indicating that the convolution with the Gaussian distribution is redundant.

Chapter 4

TRD signals from sub-TeV cosmic muons

Because of the large mass of muons – compared to the usual transition radiation (TR) inducer, the electron – it is expected that muons can induce an observable TR signal when their energies are above several hundred GeV. In fact the first observation of TR was made with cosmic muons (see [Dol93] and reference therein), where the signature was the characteristic K-line X-ray of the krypton gas which was used to absorb the TR photons from the muons. With the assumption that the TR production depends only on the Lorentz factor γ of the inducer, TR from muons has been used for the energy measurement of high energy cosmic muons [Amb03]. However, an *ab initio* measurement of the kinematic dependence of the TR from muons generally has the following technical difficulties.

1. *Muon sources:* the most common stable sources of high energy muons above the sub-TeV scale are cosmic rays which are produced by charged pion decays. These pions originate from the hadronic interactions between extraterrestrial cosmic nuclei and the atmosphere of the earth. Because cosmic rays also contain other particles like electrons, filtering must be applied to select pure muons. Only ground-based measurements, where massive background shielding could be practical, could have a good sample of muons and therefore have the possibility to observe muon-induced TR.
2. *Momentum measurement:* cosmic muons are dominantly low momentum particles. The measurement needs to be able to resolve momenta up to sub-TeV where the onset of TR is believed to occur.
3. *Background:* for muons with energies above the sub-TeV scale, the production of TR is accompanied by an increase of collisional ionization, the so-called relativistic rise. An unambiguous signal of TR from muons needs to be resolved from the large collisional ionization background.

This chapter shows that the ALICE TRD, together with the TPC, is able to measure distinctively the kinematic dependence of the TR production by muons. The idea is based on the following observations (Fig. 4.1).

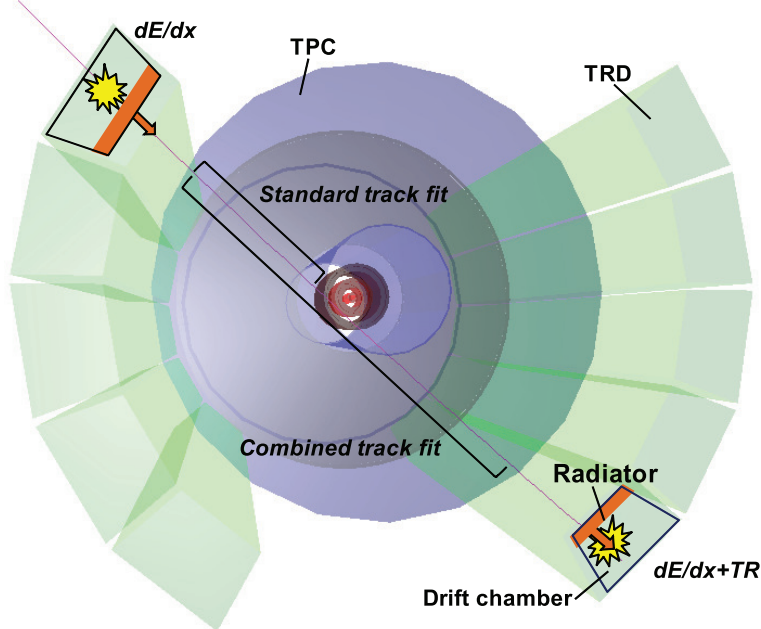


Figure 4.1: One cosmic event in ALICE TPC and TRD (3D view along the beam pipe).

- Because the ALICE experiment is situated underground with 28 meters of material above, cosmic rays which leave long trajectories in the TPC are predominantly muons.
- The momentum measurement for cosmic particles using the TPC can be improved by a factor of 10 with respect to the standard tracking, achieving a resolution of about 8% at 100 GeV/c (see Chapter 2).
- Cosmic rays traversing the TRD chamber along the gas-radiator and the radiator-gas directions have different signal compositions due to the characteristics of the emission of TR photons. Because TR photons are emitted in the forward direction along the particle momentum (emission angle $\theta_{\text{TR}} \simeq 1/\gamma$ [Ber12]), if the particle traverses in the gas-radiator direction then the TR photons produced in the radiator do not enter the gas volume and are therefore not measured. Pure TR production can be inferred by comparing these two types of signals. This work utilizes this feature for the first time.

4.1 Measurement

The measurement was based on 1.5×10^6 and 4.8×10^6 TOF-TRD triggered cosmic events with the ALICE solenoidal magnetic field 0.1 T and 0.5 T at rate 28 Hz and 17 Hz, respectively. The $B = 0.1$ T data taking was proposed in this work¹ for the measurement of the minimum ionizing muons, after an inspection on the B-field dependence of

¹This was the first ALICE running at 0.1 T.

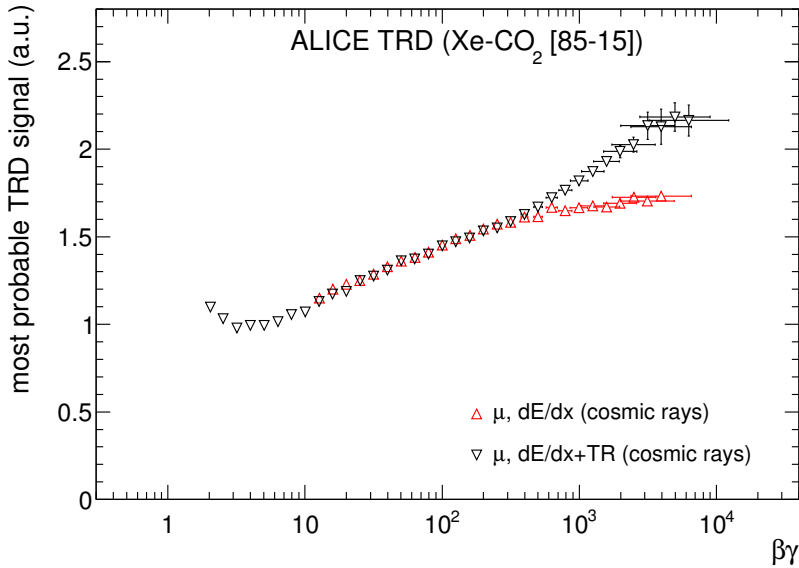


Figure 4.2: Most probable TRD signals from cosmic muons. Horizontal error bars are obtained from the estimated momentum resolution (see Chapter 2).

the low momentum cut-off in the cosmic ray spectra measured in previous data taking with $B = 0.2$ T and 0.5 T. The cut-off is due to the deflection of minimum ionizing muons out of the TPC before leaving reconstructible trajectories.

The data analysis imposes a requirement on the acceptance to avoid the particles crossing the muon filter (see Footnote 1 in Chapter 2). Only events with exactly 2 standard tracks (in the default reconstruction one cosmic particle is reconstructed as 2 tracks) are selected in order to avoid the matching ambiguity between the upper and lower tracks. In total 1.5×10^5 and 3.4×10^5 events are selected for $B = 0.1$ T and 0.5 T, respectively.

The particle momentum at $B = 0.5$ T is determined by the TPC cosmic combined track fit described in Chapter 2, while for $B = 0.1$ T only low momentum muons are selected and their momenta are determined by the standard TPC-TRD tracking. Due to the cylindrical placement of the TRD layers, the collisional ionization (dE/dx) signals are associated with the in-coming passages of the muons, while the combined ($dE/dx+TR$) signals of collisional ionization and TR are associated with the out-going ones (Fig. 4.1). Accordingly, the TRD signals from the upper and low modules are studied separately assuming the muons are coming from above². The TRD signal shape is analyzed by the statistical approach discussed in Chapter 3. The most probable signals are shown in Fig. 4.2. As can be seen, as the muon momentum increases, the dE/dx signal increases, upon which the distinct contribution from TR is observed with an onset at $\beta\gamma$ around 500.

²In practice there is no existing reliable method to distinguish between particles coming from below and from above. TOF or the momentum difference between the upper and lower tracks are not accurate enough for this purpose. In order to justify this assumption, the combined track fit in Chapter 2 is used to determine the momenta before and after traversing the absorber. No muon coming from below is observed.

4.2 Discussion

The most probable TRD signals from cosmic muons, testbeam measurements and proton-proton collisions are compiled in Fig. 4.3. The testbeam measurements [Bai06] used secondary beams consisting of pions and electrons with momentum $1 - 10 \text{ GeV}/c$ for the dE/dx and $dE/dx + \text{TR}$ measurements with prototype chambers. The collision data [Fas12] provides low momentum pions, protons and electrons from K_s^0 , Λ decays and γ -conversions. The testbeam and collision data cover the $\beta\gamma$ range $\beta\gamma \lesssim 70$ and $\beta\gamma \gtrsim 10^3$, while the region in between, where the onset of TR is observed, is only covered by the cosmic data.

The dE/dx and $dE/dx + \text{TR}$ signals of the TRD are well described by the ALEPH parametrization [Dec90] and with an additional logistic function, respectively.

The ALEPH parametrization for the dE/dx signal is (in unit of minimum ionization)

$$\frac{dE}{dx}(\beta\gamma) = p_0 \frac{p_1 - \beta^{p_3} - \ln(p_2 + \frac{1}{(\beta\gamma)^{p_4}})}{\beta^{p_3}}, \quad (4.1)$$

with the fitted parameters shown in Table 4.1. This model describes the dE/dx with a saturation yield of 1.8 unit of minimum ionization in the high momentum limit.

	p_0	p_1	p_2	p_3	p_4
value	0.31	3.0	0.026	2.17	0.65
error	0.03	0.2	0.007	0.04	0.03

Table 4.1: Fitted parameters of the ALEPH parametrization to the dE/dx TRD signal.

The ALEPH+logistic parametrization for the $dE/dx + \text{TR}$ signal is (in unit of minimum ionization)

$$\left(\frac{dE}{dx} + \text{TR} \right)(\beta\gamma) = \frac{dE}{dx}(\beta\gamma; p_0, \dots, p_4) + \frac{p_5}{1 + \exp(-p_6(\ln \gamma - p_7))}, \quad (4.2)$$

with parameters shown in Table 4.2. In this model the saturation yield of $dE/dx + \text{TR}$ is 2.4 unit of minimum ionization. The 10%--, 50%- and 90%-saturation points of the logistic function are

$$\gamma_{0.1} = 4.2 \times 10^2, \quad (4.3)$$

$$\gamma_{0.5} = 2.2 \times 10^3, \quad (4.4)$$

$$\gamma_{0.9} = 1.2 \times 10^4, \quad (4.5)$$

respectively.

	p_0	p_1	p_2	p_3	p_4	p_5	p_6	p_7
value	0.313	3.05	0.035	2.17	0.66	0.72	1.33	7.70
error	0.003	0.02	0.002	0.04	0.01	0.03	0.07	0.06

Table 4.2: Fitted parameters of the ALEPH+logistic parametrization to the $dE/dx + \text{TR}$ TRD signal.

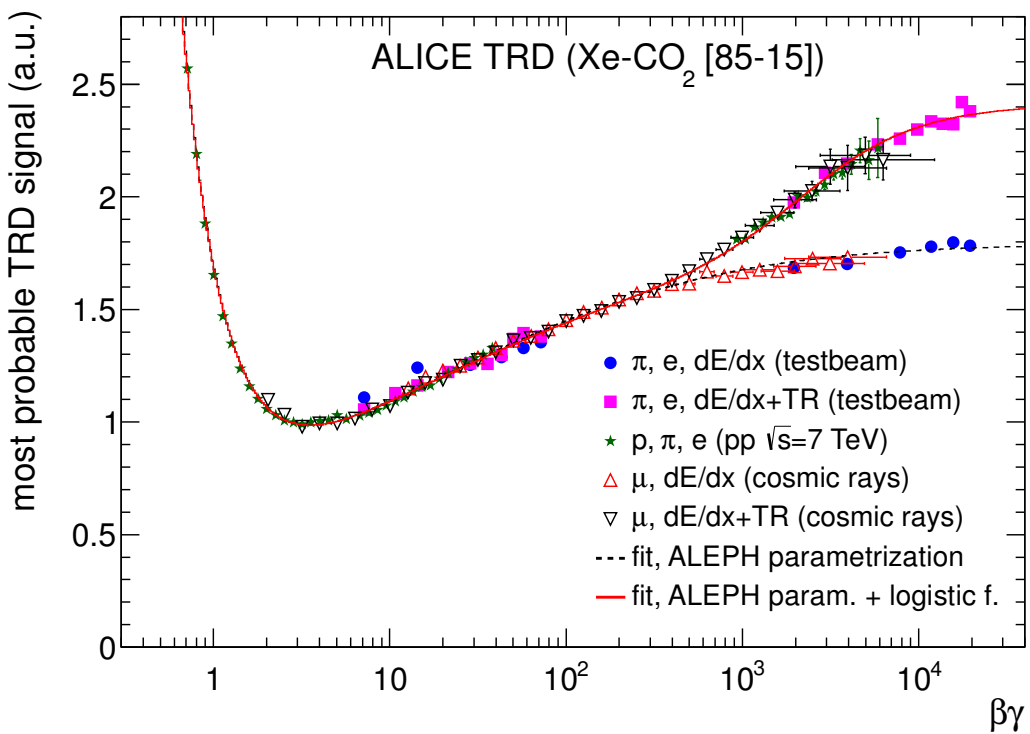


Figure 4.3: Most probable values of the TRD signals from different data sets as a function of $\beta\gamma$.

Chapter 5

TRD truncated mean signal

The signal of a particle in the TRD is measured in six layers of detector chambers, in each of which the induced charges are collected every 100 ns. After baseline subtraction, pad gain calibration, and correction for non-perpendicular incident angles, the collected charges in each time-bin form the so-called cluster signal [Cor01, Aam08]. These signals are characterized by the heavy tail originating from the Landau distribution (see discussions in Chapter 3).

The truncated mean signal of a particle is defined as the truncated mean (also called the trimmed mean [Mar06]) of its associated N above-baseline cluster signals [Blu08]:

$$\langle Q \rangle_f \equiv \sum_{i=1}^M Q_i / M, \quad (5.1)$$

where Q_i is the i -th smallest one among all time-bins, $f \in (0, 1]$ is the truncation fraction and M is the largest integer smaller than Nf . It is an estimator for the expected signal at the cluster level. Its advantage is robustness and high efficiency (namely small variation) for heavy-tailed distributions [Mar06]. The truncated mean signals of a sample of particles follow a distribution which depends on the particle velocity and thus provide information on the particle types. Complementary to the design capability of the TRD, which is optimized for the electron–hadron separation [Cor01, Loh13], this method allows separation between different particle species, enabling the TRD for robust identification of electrons and hadrons.

This chapter presents the technical principle and performance of this newly established method as follows. Section 5.1 discusses the influence of the time-bin dependence of the cluster signals and the resulting physical signal composition in terms of collisional ionization and transition radiation (TR). Section 5.2 describes the so-called time-bin gain calibration. Section 5.3 shows the optimization by tuning the truncation fraction f . Section 5.4 discusses the properties of the truncated mean signal as a function of the number of clusters N . In the end, the particle identification capability of the truncated mean signal is presented in Section 5.5.

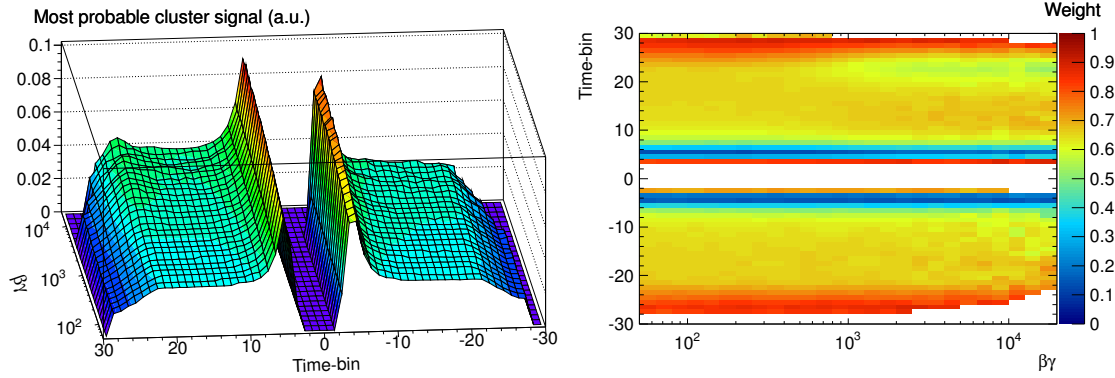


Figure 5.1: Development of the most probable cluster signals (*left*) and the weight (*right* panel, see text for definition, $f = 0.6$) with an increasing velocity of cosmic muons. Positive and negative time-bins are for the lower and upper TRD sectors, respectively.

5.1 Influence of the time-bin dependence of the cluster signals

Suppose in the ideal case when all cluster signals followed the same distribution, the rejection of the heavy tail which is subject to large fluctuations would improve the estimation of the mean cluster signal. However, in the TRD the distribution of the cluster signals depends on the radial position (represented by the time-bin) of the cluster. This is due to the combined effects of the drift field configuration and the varying composition of the combined signal of the collisional energy loss and the transition radiation. The time-bin dependence introduces nonuniform weights via the ordering required by Eq. 5.1 in such a way that large signals under small fluctuations can also be frequently rejected from the summation, leading to a deteriorated estimation. On the other hand, despite this weighting effect, the summation in Eq. 5.1 is still sensitive to the expected sum of all time-bin contributions. This is because for a given truncation fraction, a larger rejection probability for some signals means a larger survival probability for the others (for illustration see the *right* panels of Figs. 5.1 and 5.4 and the corresponding text). As a consequence, even though the late time-bin signals with a large TR component is more often rejected, the loss of TR is compensated by the collisional ionization in early time-bins, preserving the TR signature.

The time-bin dependence of the cluster signals is best illustrated with the cosmic data (see Chapter 4). Depending on the detector position, either the collisional ionization or the combined signal with TR can be measured. Figure 5.1 (*left*) shows the development of the most probable cluster signals with an increasing velocity of cosmic muons. The time-bins for the detector sectors in the upper half of the TRD cylindrical placement, which measure the pure collisional ionization, are multiplied by -1. The positive time-bins are for the lower sectors which measure the combined signals. The amplification peaks in early time-bins dominate the signal spectra. At high velocity TR contributions in late positive time-bins are visible.

The definition of the truncated mean requires a sorting and a partial sum. This is equiv-

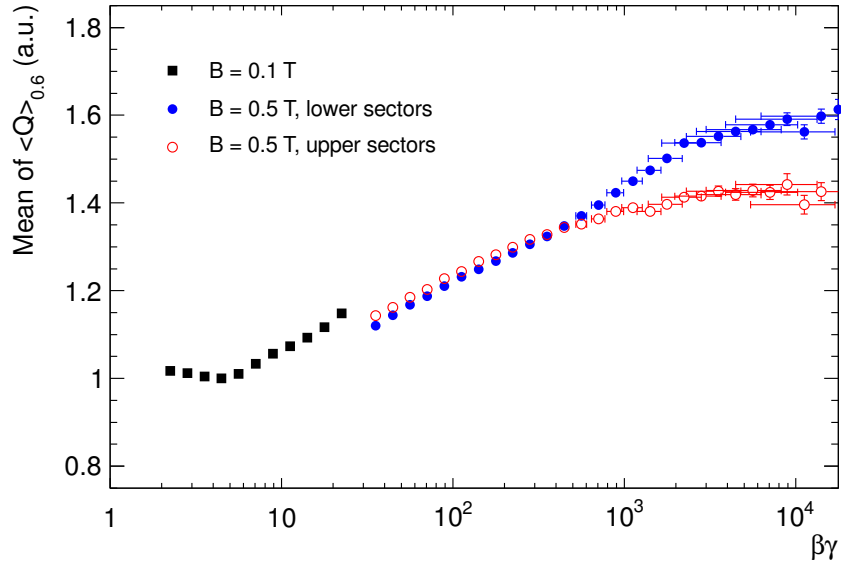


Figure 5.2: Mean values of $\langle Q \rangle_{0.6}$ from two cosmic data taking periods with $B = 0.1$ T and $B = 0.5$ T. Note that the y -scale is chosen such that the minimum ionizing signal is around 1. Signals from upper and lower sector at $B = 0.5$ T are separately shown. The discrepancy between data sets is due to uncalibrated detector effects at the cluster level (see Section 5.2).

alent to assigning to individual cluster signals the following weights:

$$\epsilon(t) \equiv \frac{N_{\text{summed}}(t)}{N_{\text{total}}(t)}, \quad (5.2)$$

where $N_{\text{summed}}(t)$ is the frequency for the cluster signal $Q(t)$ at time-bin t being summed in Eq. 5.1 and $N_{\text{total}}(t)$ is the frequency of an above-baseline $Q(t)$. If Q at different time-bins had identical distributions, ϵ would be independent of t and equal to the truncation fraction f . The larger a most probable value $Q(t)$ has, the smaller $\epsilon(t)$ becomes. Figure 5.1 (right) shows the development of $\epsilon(t)$ with an increasing velocity of cosmic muons (the time-bin convention is the same as in Fig. 5.1). It can be seen that in the amplification region the weights are much smaller than in the tail region.

The compensation effect, which preserves the physical sensitivity, is also visible in Fig. 5.1 (right). In the late positive time-bins at high velocity where TR is present, the weights are smaller than in the adjacent earlier time-bins. As a result, the TR signature is preserved, as can be seen in Fig. 5.2 where high- γ cosmic signals in the upper and lower TRD sectors are compared.

5.2 Time-bin gain calibration

The advantage of the truncated mean is to reject contributions with large fluctuations so as to obtain a more precise estimation of the mean cluster signal. This is based on the assumption that the summands in Eq. 5.1 follow the same distribution. The time-bin

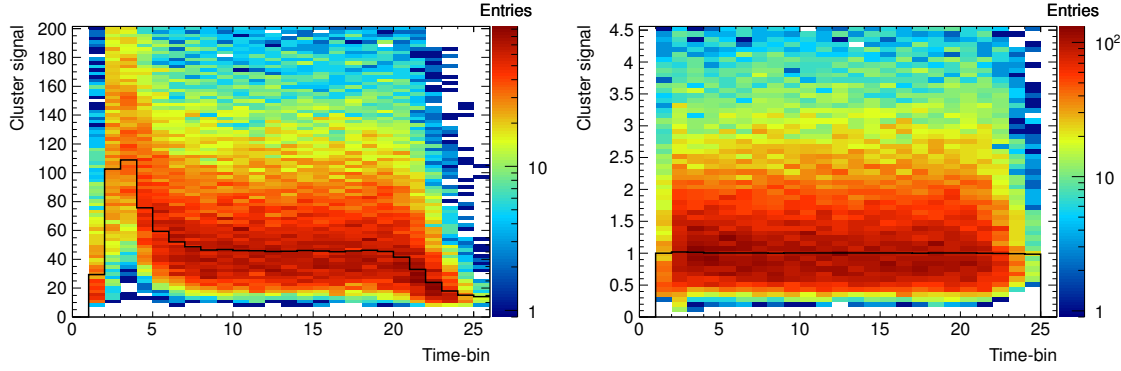


Figure 5.3: Cluster signal distributions in different time-bins (*left*) before and (*right*) after the time-bin gain calibration. The black line indicates the most probable values.

dependence of the cluster signals imposes a necessity for a gain equalization among time-bins. This so-called time-bin gain calibration is also needed because at the cluster level several detector effects governing different time-bin regions start to show up, for example,

- the gas density and the drift velocity whose inhomogeneity will distort the drift charge density per time bin,
- the electric field line configuration which determines the amplification peak in the early time-bins,
- and the detector time response which characterizes the shape of the ion tails in the late time-bins.

The idea of the calibration is to equalize the $Q(t)$ distributions in different time-bins to a common scale. As can be seen in Fig. 5.3 (*left*), which shows the cluster signal distributions in different time-bins, the most probable values $Q_M(t)$ differ among time-bins. The calibration procedure scales $Q(t)$ with $1/Q_M(t)$, resulting in the distribution shown in Fig. 5.3 (*right*).

In practice, $Q_M(t)$ is derived from a data sample in a small $\beta\gamma$ interval to eliminate the large variation due to the kinematic dependence. For the cosmic data the sample is restricted to $1.65 < \log_{10} \beta\gamma < 2.5$. Figure 5.4 (*left*) shows the resulting development of the most probable cluster signal after the calibration (see Fig. 5.1 for comparison). Since the scale is set to $\beta\gamma$ around 100, far below the onset of TR, we see an increase of the collisional ionization uniform among negative time-bins (upper TRD sectors) and the TR development in the positive time-bins (lower TRD sectors). The remaining non-uniformity over time-bins only exists due to this TR component. The corresponding non-uniformity in weight is within $\pm 15\%$, as can be seen in Fig. 5.4 (*right* panel, see Fig. 5.1 for comparison). In the same figure the compensation effect is more visible.

Because the calibration is performed per time-bin, namely as a function of the radial position, differentially it equalizes the combined effect of the multiple detector systematics. The time-bin gain calibration guarantees the consistency between the truncated mean signals in different detector parts and data taking periods. This is shown in Fig. 5.5 as

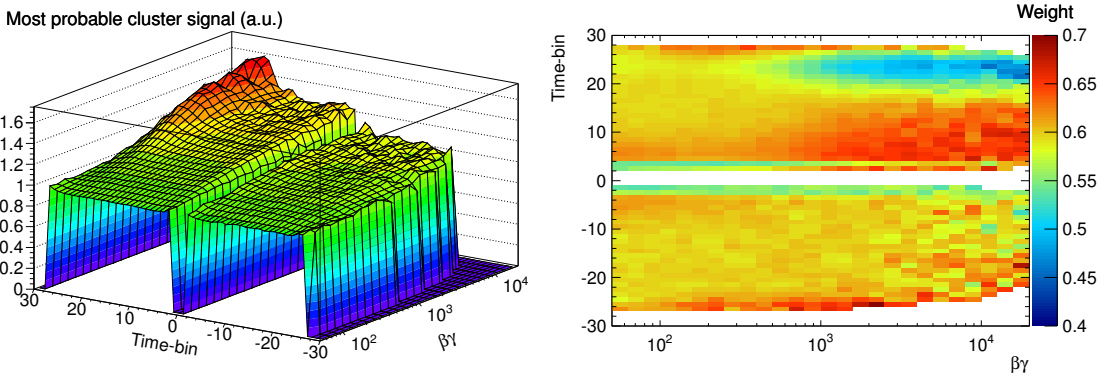


Figure 5.4: Development of the most probable cluster signals (*left*) and the weight (*right*) after the time-bin gain calibration.

an updated version after the time-bin gain calibration compared to Fig. 5.2. As can be seen besides the elimination of the discrepancy, the separation between the mean signals at low and high $\beta\gamma$ is improved.

The performance of the calibration can be characterized by the separation power:

$$s(\beta; \beta_0) \equiv \frac{\Delta m}{\bar{\sigma}} \equiv \frac{m(\beta) - m(\beta_0)}{\frac{1}{2} [\sigma(\beta) + \sigma(\beta_0)]}, \quad (5.3)$$

where $m(\beta)$ and $\sigma(\beta)$ are the mean and the standard deviation of $\langle Q \rangle_f$ (the f -dependence is implicit), respectively, as functions of the velocity β (in unit of the speed of light). For pp and Pb–Pb collision data, further optimization of the following degrees of freedom is performed according to the separation power:

- Calibration scale: the common scale for the calibration can be chosen in different ways.
 1. With a sample of identified particles from known decays, for example, protons from Λ , π^\pm from K_s^0 and electrons from photon conversions [Fas12], the particle velocity (β_0) can be restricted. The most probable cluster signal $Q_M(t; \beta = \beta_0)$ can be used as the scale. This method provides the most physically accurate scale but suffers from limited statistics due to the inefficiency of particle identification and the narrow velocity interval required to reduce the kinematic dependence. In practice the statistical fluctuation of $Q_M(t; \beta = \beta_0)$ cannot be neglected.
 2. By assuming that the whole data sample has a stable composition of particles with constant momentum distributions, one can use $Q_M(t)$ from the whole data sample as the scale. However the assumption is generally not valid for different triggers.
 3. As an improvement [Iva12] of method 2, the most probable values of $Q(t)/Q_{\text{TPC}}$ from the whole data sample can be used as the scale, where Q_{TPC} is the TPC energy loss signal. Due to the good resolution of the TPC signal, this method provides a practically accurate scale with minimum statistical fluctuation.

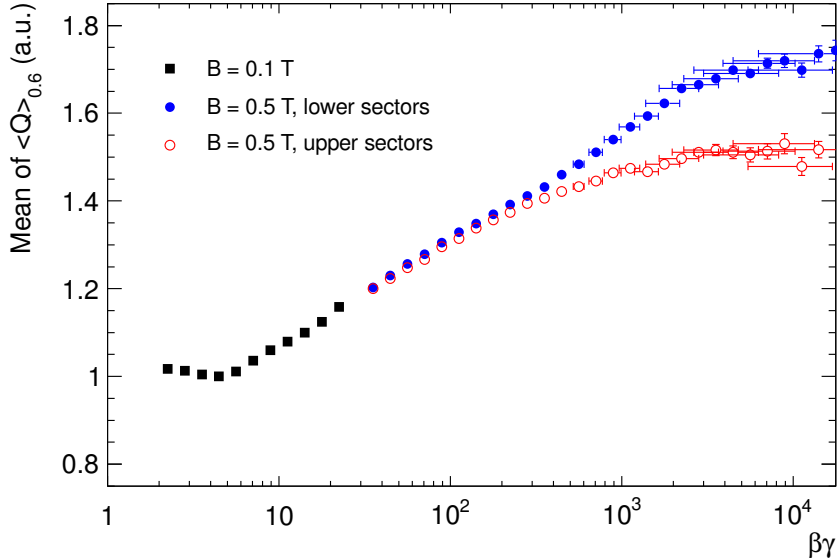


Figure 5.5: Mean values of $\langle Q \rangle_{0.6}$ after the time-bin gain calibration. The y -scale is chosen such that the minimum ionizing signal is around 1.

The trade-off among these methods is accuracy against statistics. Comparison between method 1 and 3 using collision data shows that the latter (scaling to TPC) has a better performance by a 4% relative increase in the separation power.

- Particle charge dependence: the calibration is done separately for different magnetic field and particle charge combinations, in which way the performance is improved by 0.6% for pp data and 1.3% for Pb–Pb data.

5.3 Tuning the truncation fraction

The truncation fraction f is defined between 0 and 1. Hence there is a degree of freedom to optimize the truncated mean signal according to the separation s defined in Eq. 5.3. As f increases, larger number of contributions are summed in Eq. 5.1, leading to an increase of m , namely $d\Delta m/df > 0$. Yet $d\Delta m/df = \Delta(dm/df)$ is generally not determined. It depends on the particular cluster signal distributions at the given velocities. The f -dependence of σ is relatively straightforward. Note that $\bar{\sigma} \simeq \sigma \simeq \sigma_c/\sqrt{M}$ where σ_c is the standard deviation of the Q_i sample included in the summation in Eq. 5.1. As f increases, cluster signals with larger and larger fluctuations are included while M also increases. Therefore $d\bar{\sigma}/df$ is the competing results of the increasing fluctuation and statistics. It may attain a minimum by tuning f .

The f -dependence of Δm , σ and s is obtained in data samples from two pp runs taken in two different periods. The particle velocities are measured via identified electrons from γ -conversions and charged pions from K_s^0 decays [Fas12]. The velocities to compare at are $\log_{10} \beta_0 \gamma_0 = 0.55$ and $\log_{10} \beta \gamma = 3.15$, which are obtained with minimum ionizing charged pions with momentum 0.5 GeV/c and electrons with momentum 0.7 GeV/c, respectively. The choice of the high velocity is made so as to use the maximum statistics

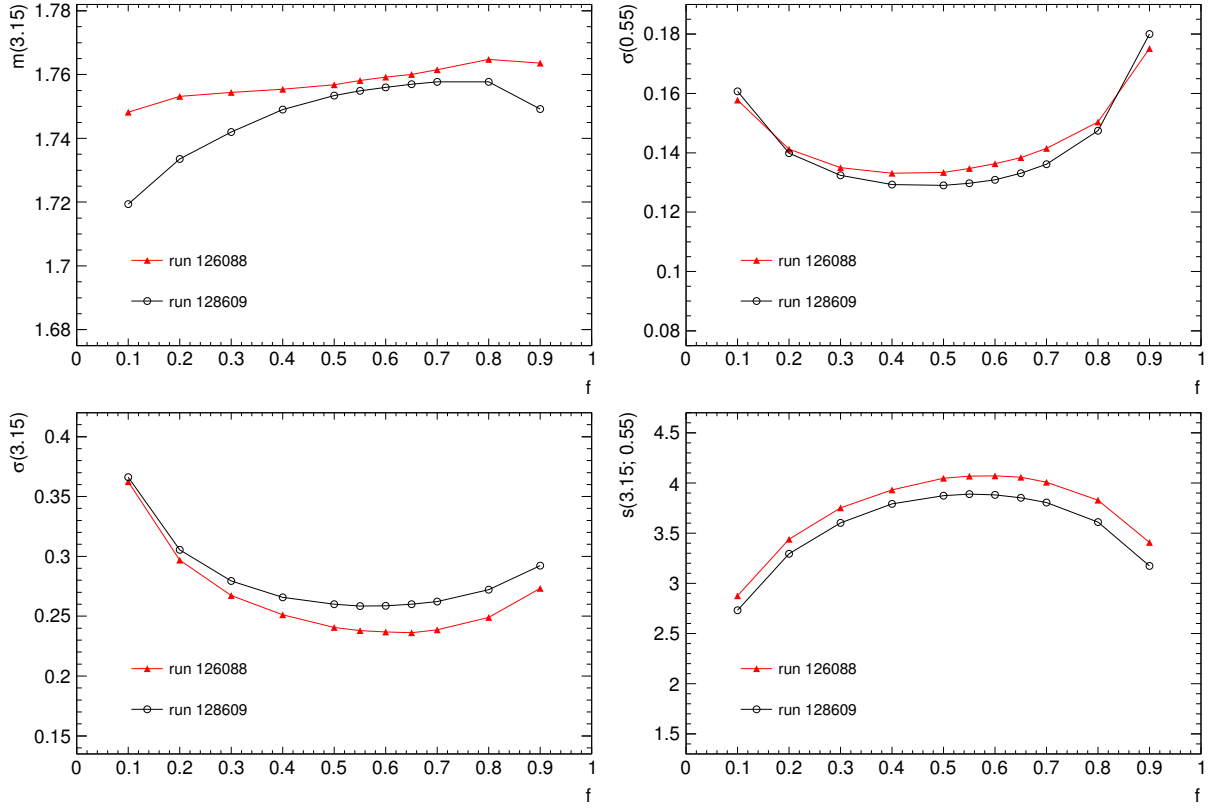


Figure 5.6: The mean, the standard deviation and the separation of the truncated mean signal as a function of the truncation fraction. Note that the arguments of all y -axis functions are $\log_{10} \beta \gamma$ and that the scale of the signal is chosen in such a way that $m(\log_{10} \beta \gamma = 0.55) = 1$ for all f .

of the electron sample. The tuning results are shown in Fig. 5.6. It is observed that

- Δm increases with f for $f < 0.8$,
- σ attains a global minimum in f between 0.4 and 0.5,
- and the resulting separation s is maximum at about $f = 0.55$.

Accordingly, the optimum value $f = 0.55$ is used for further studies.

5.4 Dependence on the number of clusters

The effect related to N , the number of above-baseline cluster signals, is both statistical and systematical. While the statistical fact, that with larger N the relative spread of $\langle Q \rangle_f$ becomes smaller, is basic, the N -dependence of the mean of $\langle Q \rangle_f$ is non-trivial. The essence of the problem is, that the expected N is determined by the cumulative

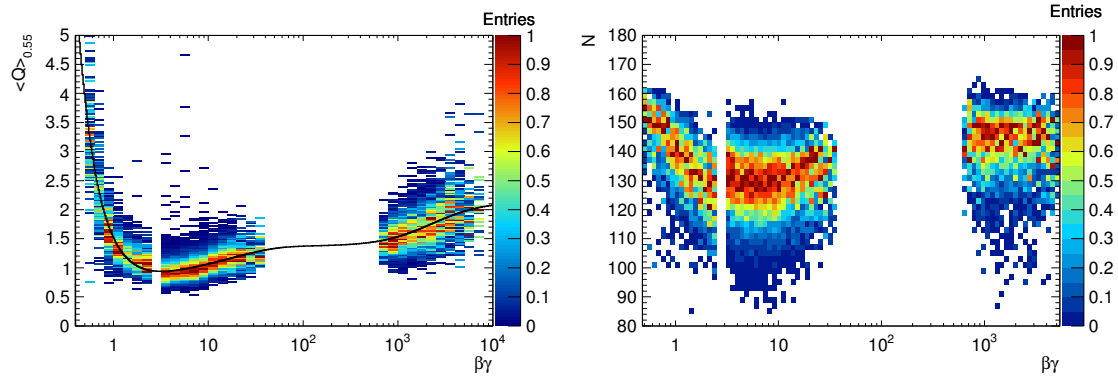


Figure 5.7: Truncated mean signals (*left*) and the number of above-baseline clusters (*right*) as a function of the velocities of the identified particles from Λ , K_s^0 decays and γ conversions [Fas12] from pp collisions at 7 TeV. The three distinct regions in $\log_{10} \beta\gamma$ are from left to right exclusively populated with protons, charged pions and electrons. The black curve is an ALEPH+logistic fit to the mean of $\langle Q \rangle_{0.55}$ (see Section 4.2).

distribution function of the cluster charge Q ,

$$N \sim \int_{\text{baseline}}^{\infty} g(Q) dQ, \quad (5.4)$$

where g is the probability density function of Q . Generally the baseline is not dynamically adjusted and the particle velocity dependence comes in via the distribution function g . In this sense N also provides separation power as the energy loss does. However its realization involves complicated systematics. On the other hand, the common velocity dependence introduces a correlation between N and $\langle Q \rangle_f$. Figure 5.7 shows the kinematic dependence of both quantities.

The broad distribution of the number of clusters at given $\beta\gamma$ is due to the following reasons beside the intrinsic fluctuation of the number of primary collisions.

- The constant baseline is subject to gain variation.
- The number of clusters is proportional to the number of primary collisions which depends on the path length (Fig. 5.8).
- Cluster signals in neighboring time-bins are correlated due to the time response in the readout electronics. Signal tails smear out the distribution of the number of clusters.

In order to study how the number of clusters affects the truncated mean signal, the kinematic dependence has to be factored out by scaling down the signal by the expected value as a function of $\beta\gamma$. The expected value is evaluated by an ALEPH+logistic fit (see Section 4.2) to the mean of the signals in each $\beta\gamma$ bin as is shown in Fig. 5.7 (*left*). The correlation between the scaled signal and the number of clusters is shown in Fig. 5.9 (*left*). It shows that there is a systematic deviation of the signal with respect to the expected value as the number of clusters varies. As a result, the signal is broadened due

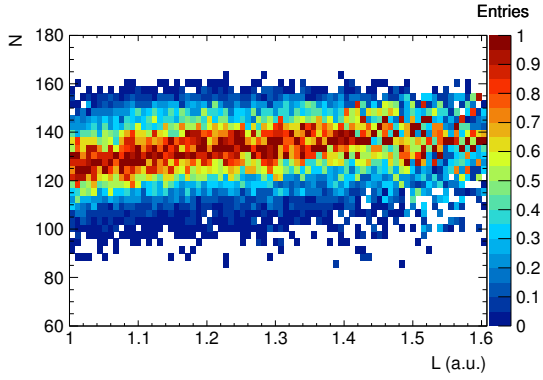


Figure 5.8: Number of clusters as a function of the particle path length in the TRD.

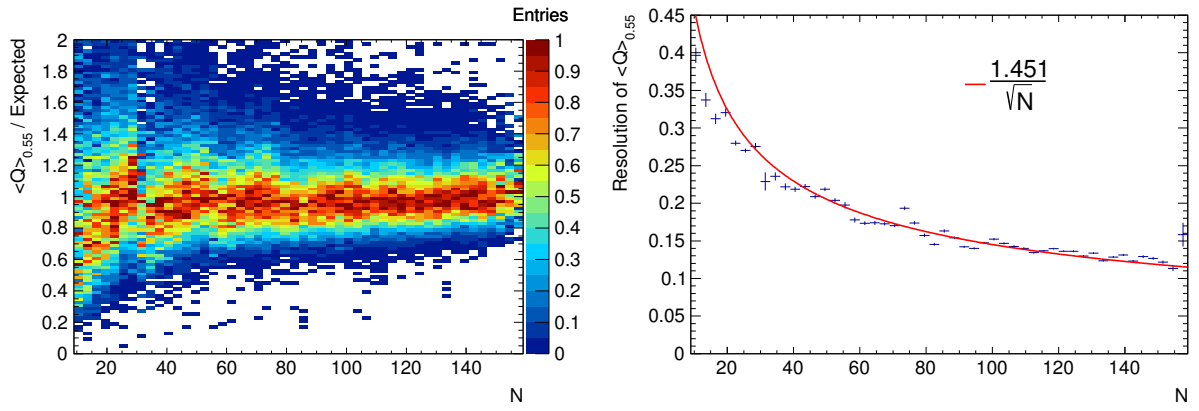


Figure 5.9: (*Left*) Scaled truncated mean signal and (*right*) the signal resolution as a function of the number of clusters.

to its correlation with the number of clusters which is subject to non-trivial systematic variations.

The resolution of the signal, σ/m , calculated as the width of the scaled signal, also changes with the number of clusters, see Fig. 5.9 (*right*). The resolution is well approximated by

$$\frac{\sigma}{m} = \frac{1.451}{\sqrt{N}}, \quad (5.5)$$

indicating that the number of above-baseline clusters N is in a good approximation proportional to the number of primary ionization collisions N_p ,

$$N_p \sim kN, \quad (5.6)$$

where the coefficient k is independent of N .

Due to the dependence of the signal performance on the number of clusters, it is recommended to cut on the number of chambers that have signals and the number of clusters per chamber to reduce the spread of the signal.

5.5 Particle identification with the truncated mean signal

The kinematic dependence of the truncated mean signal provides separation power between different particle types. The combined signal of collisional ionization and TR enables identification among hadrons and also between electrons and hadrons. As can be seen in Figure 5.10 and 5.11, electrons, pions, kaons, and protons can be identified. The electrons signal is seen to rise with momentum as expected because of the increasing TR yield. A further application of the truncated mean signal is to identify light nuclei, for example, the deuteron as is shown in Fig. 5.10.

The identification capability of the truncated mean signal is quantified at a given momentum p by the electron and pion efficiencies $E_{e,\pi}(p; q_{\text{cut}})$, which are simultaneously calculated from the distributions of the truncated mean signal q for a given cut q_{cut} :¹

$$E_{e,\pi}(p; q_{\text{cut}}) = \int_{q_{\text{cut}}}^{\infty} f_{e,\pi}(q; p) dq, \quad (5.7)$$

where $f_{e,\pi}(q; p)$ are the probability densities of the signal q at momentum p for electrons and pions, see Fig. 5.12 for instance. The correlation between the pion and electron efficiencies is shown in Fig. 5.13. The momentum ordering² of the performance is due to the decreasing separation at high momentum because of the relativistic rise of the pion signal. It can be seen that at momentum around 1 GeV/c a signal cut selecting 90% of the electrons will select about 1.5% of the pions³, resulting in a pion rejection factor of about $1/0.015 \simeq 67$.

¹Note that the calculation relies on the purity of the electron and pion samples. Impurity will introduce outliers in the distributions, leading to worse performance.

²The crossings between the correlation curves for $p \leq 2$ at low electron efficiencies (50–60%) are due to the improvement of the performance at high momentum because of larger TR yields.

³The ratio between the selected electrons and pions depends on their total yields.

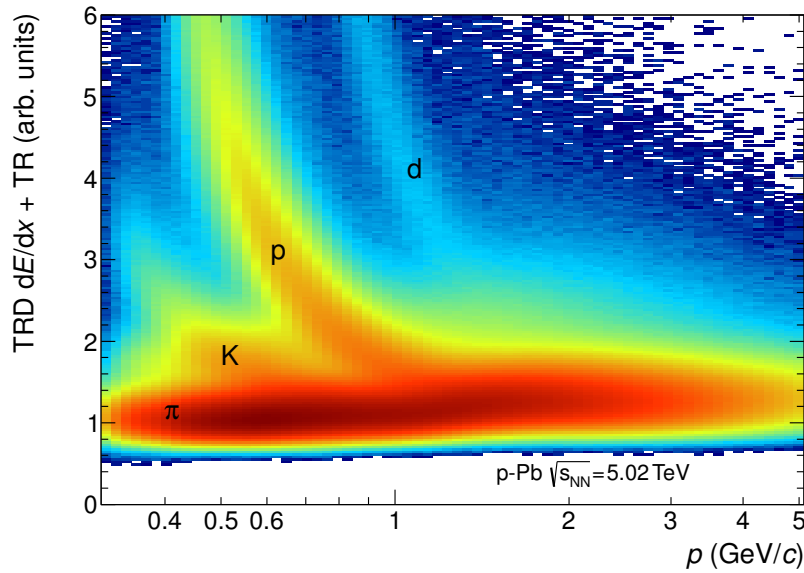


Figure 5.10: Truncated mean signals as a function of momentum for charged particles in minimum bias data from p-Pb collisions at $\sqrt{s_{NN}} = 5.02$ TeV (LHC period 13c).

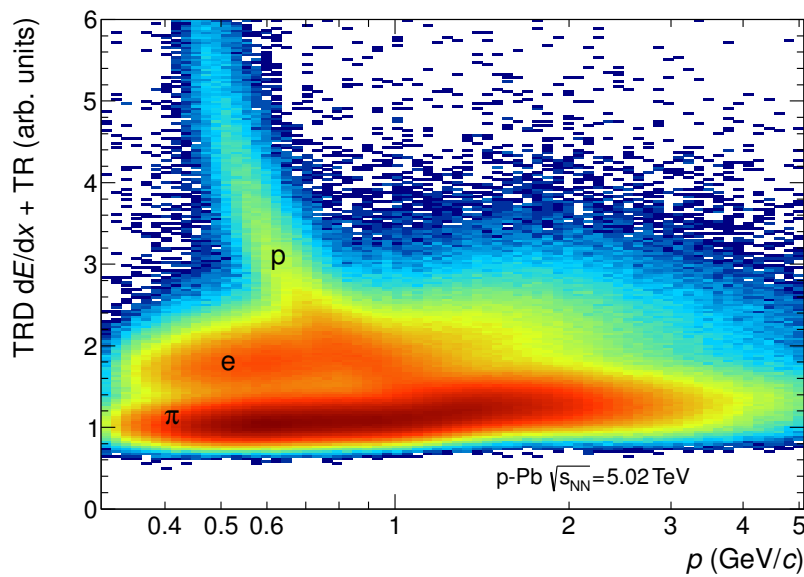


Figure 5.11: Truncated mean signals as a function of momentum for protons from Λ , charged pions from K_s^0 , and electrons from γ -conversions [Fas12] from p-Pb collisions at $\sqrt{s_{NN}} = 5.02$ TeV (LHC period 13c).

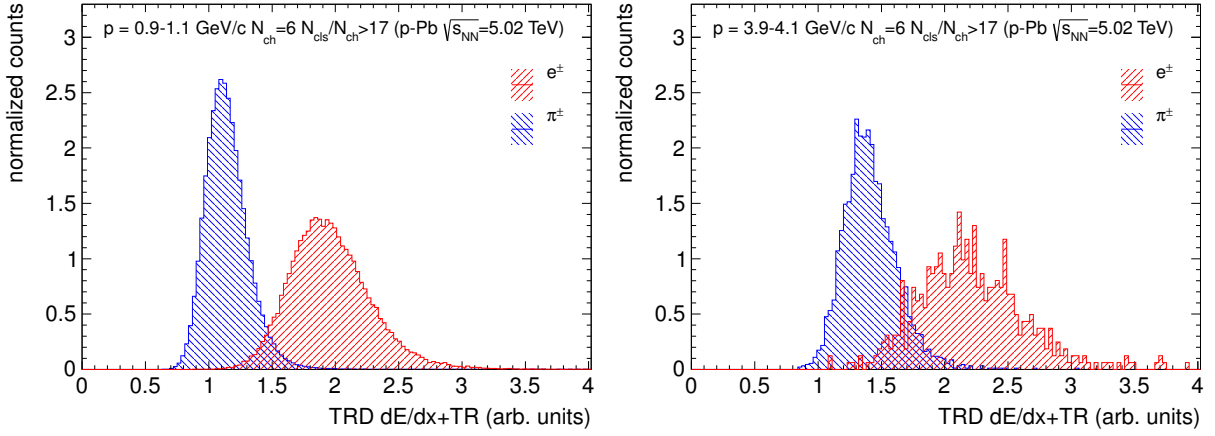


Figure 5.12: Probability densities of the truncated mean signal for pions from K_s^0 and electrons from γ -conversions [Fas12] from p-Pb collisions at $\sqrt{s_{NN}} = 5.02 \text{ TeV}$ (LHC period 13c) in the momentum bins (left) $0.9\text{--}1.1 \text{ GeV}/c$ and (right) $3.9\text{--}4.1 \text{ GeV}/c$. It is obtained by requiring signals in six TRD chambers for each track and the number of (above-baseline) clusters per chamber larger than 17.

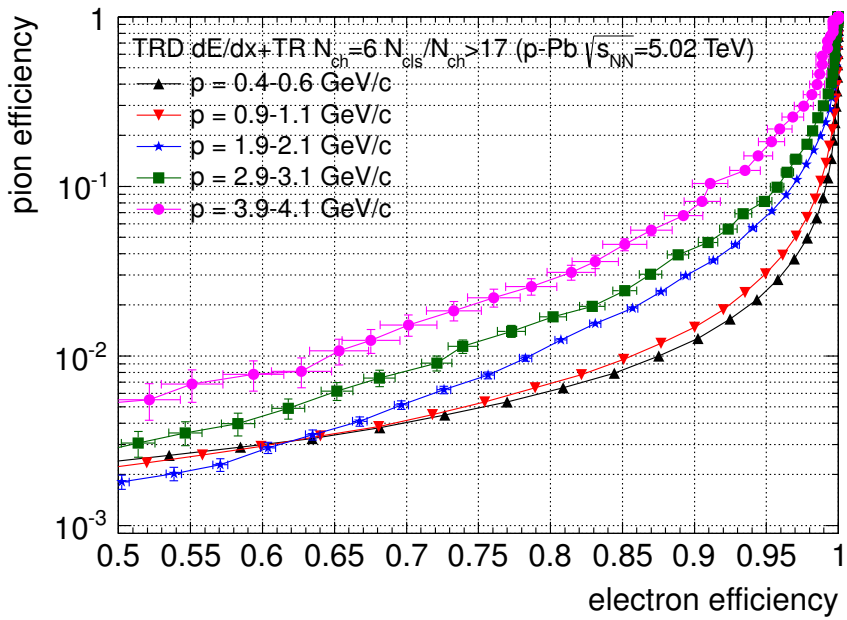


Figure 5.13: Correlation between pion and electron efficiencies (see text for definition) at different momenta (p-Pb collisions at $\sqrt{s_{NN}} = 5.02 \text{ TeV}$, LHC period 13c). Error bars are statistical only.

Chapter 6

The TPC coherent fit

The ALICE TPC measures the energy deposit of the traversing particles. For different particle species, the TPC signal [Alm10], which is the truncated mean ionization energy loss per path length, shows different momentum dependence (Fig. 6.1). With a resolution of about 5%, the TPC signal provides separation power among different particle types from momentum of several hundred MeV/c (limited by acceptance) up to above 20 GeV/c. This chapter shows how one can extract the yield of a given particle type using the TPC signal alone in this momentum range. Technically, the method disentangles the particle contents in a two-dimensional observable space (p, Δ) as in shown in Fig. 6.1, where Δ is the TPC signal and p is the momentum of the traversing particle.

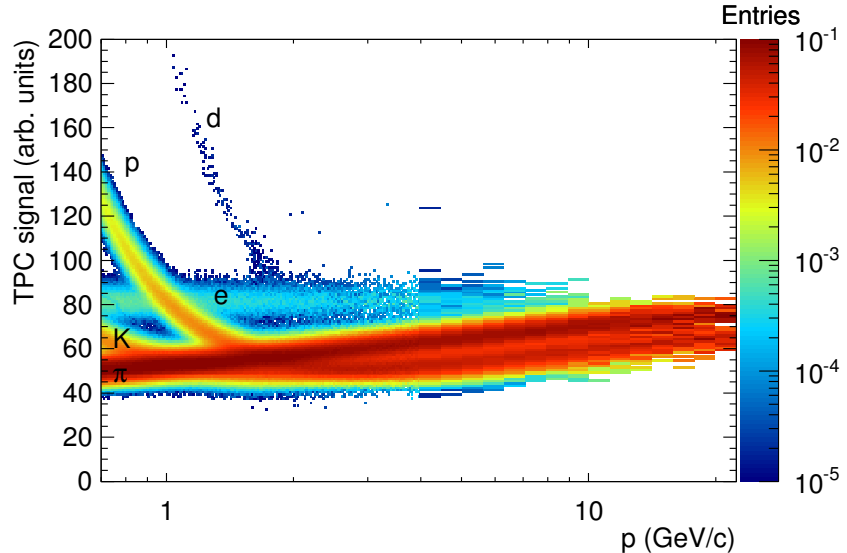


Figure 6.1: TPC signal as a function of the momentum of traversing particles.

The method relies on the following observations:

- The statistically dominant particle species are protons¹, kaons, pions and electrons².

¹In this chapter no charge distinction is made and therefore protons refer to protons and antiprotons.

²The TPC signal resolution is not good enough to resolve muons and pions. The measured pion

Light nuclei, like the deuteron, can be ignored.

- The signal shape for a given particle species can be well approximated by a Gaussian distribution $G(\Delta; \mu, \sigma)$ with mean μ and standard deviation σ . The overall signal shape at a given momentum p is therefore the weighted sum of 4 Gaussian distributions (particle type dependence of μ and σ is implicit)

$$\sum_k A_k(p) G(\Delta; \mu, \sigma), \quad (6.1)$$

where the sum is made over particle type- k and A_k is the corresponding fraction normalized at p , namely

$$\sum_k A_k(p) = 1. \quad (6.2)$$

- The signal mean μ is a function of the particle velocity³

$$\mu = \mu\left(\frac{p}{m}; \mathbf{a}\right), \quad (6.3)$$

with parameters \mathbf{a} .⁴ The particle mass is denoted as m .

- The signal spread σ can be well approximated by a function of μ

$$\sigma = \sigma(\mu; \mathbf{b}), \quad (6.4)$$

with parameters \mathbf{b} .

- The fraction of a given particle species, A_k , is a continuous function of the momentum.

With appropriate models for the signal mean and spread, particle fractions and signal properties can be simultaneously extracted by fitting the constructed particle distribution with free parameters $A_k(p)$, \mathbf{a} and \mathbf{b} to the measured one. Because information between momentum bins are used coherently in one single likelihood maximization, this fitting procedure is called the TPC *coherent* fit.

This chapter is organized as follows. We first set the stage for the method with definitions. Then the full machinery will be described, followed by discussions of error estimation and data analysis.

6.1 Setting the stage

6.1.1 Definition of the momentum observable

The TPC coherent fit disentangles particle species in the two-dimensional observable space (p, Δ) . It provides an estimate for the fraction of a given particle type $A_k(p)$ as a

fraction, to be precise, is contaminated with muons, the fraction of which after cuts for primary particles is at most at per mil level in minimum bias data.

³Other dependencies according to the detailed experimental setup can be treated as higher order systematic uncertainties or corrections.

⁴A quantity \mathbf{x} is a compact notation for a set of quantities x_1, x_2, \dots

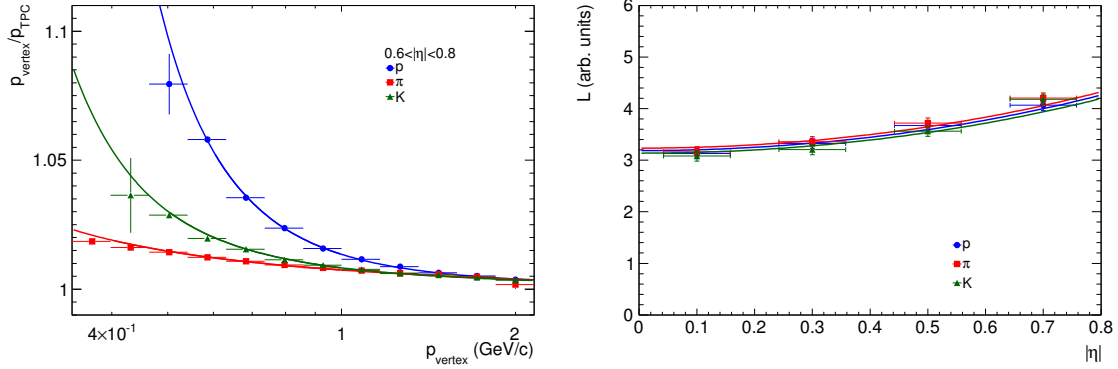


Figure 6.2: Energy loss between the collision vertex and the TPC. *Left:* fitting the momentum ratio $p_{\text{vertex}}/p_{\text{TPC}}$ in a single pseudo-rapidity $|\eta|$ window. The points are experimental data and the curves are the fitting results of Eq. 6.5 with the material budget L as a free parameter. *Right:* material budget L as a function of $|\eta|$. The points are the fitting results of L in different $|\eta|$ windows and the curves are Eq. 6.6 fitted to the points with parameter B .

function of the momentum which can either be the one measured at the collision vertex or at the TPC inner wall. Due to the material in between, a particle loses some energy before entering the TPC⁵:

$$E_{\text{miss}} = \sqrt{p_{\text{vertex}}^2 + m^2} - \sqrt{p_{\text{TPC}}^2 + m^2} = L\langle\delta\rangle \simeq L\delta\left(\frac{p_{\text{vertex}}}{m}\right), \quad (6.5)$$

where m is the particle mass, L is the material budget between the vertex and the TPC and $\langle\delta\rangle$ is the mean specific energy loss, which can be estimated with the standard Bethe-Bloch formula $\delta(\beta\gamma)$ [Ber12] calculated with p_{vertex} and m . This effect can be evaluated from data. As can be seen in Fig. 6.2 (*left*), the momentum bias is about 5% below 1 GeV/c and can be ignored above 2 GeV/c. Even though the TPC signal is determined by p_{TPC} , $A_k(p_{\text{vertex}})$ is eventually needed for physics study (for a precise conversion to $A_k(p_{\text{T}})$, see discussion in Section 6.1.2). In this work, the observable space $(p_{\text{vertex}}, \Delta)$ is used and during the coherent fit, p_{vertex} is internally converted to p_{TPC} using Eq. 6.5 with

$$L = \frac{B}{\sin(2\tan^{-1}(e^{|\eta|}))}, \quad (6.6)$$

where

$$\eta = -\ln \tan \frac{\theta}{2} \quad (6.7)$$

is the pseudo-rapidity of the particle with the polar angle θ with respect to the collision axis and B is a free parameter obtained from data (Fig. 6.2 *right*). Namely the signal mean internally has this form:

$$\mu = \mu\left(\frac{p_{\text{TPC}}}{m}; \mathbf{a}\right). \quad (6.8)$$

From here on the subscript of the momentum will be suppressed unless in case of potential confusion.

⁵The energy loss integrated in the TPC volume is significantly smaller and can be neglected.

6.1.2 η -window restriction

The observable space (p, Δ) has to be restricted in a small window of $|\eta|$. The reason is two-fold:

- The mean and spread of the TPC signal depend on the inclination angle of the traversing particle with respect to the drift field. This is because the ionization energy loss of the particle in the gas depends on the path length⁶, and the drift length of the ions depends on the location of the primary ionization. Signals of particles with large $|\eta|$ have better resolution due to a larger number of primary ionization and a shorter drift length. As will be shown in Section 6.4, signals from different $|\eta|$ -windows exhibit different systematics.
- From the physics point of view, particle production is often studied as a function of the transverse momentum p_T instead of p . In a small $|\eta|$ -window the one-to-one correspondence between p_T and $p_{(\text{vertex})}$ is manifest (Fig. 6.3). The fraction of particle- k $A_k(p)$ can be precisely converted to $A_k(p_T)$.⁷

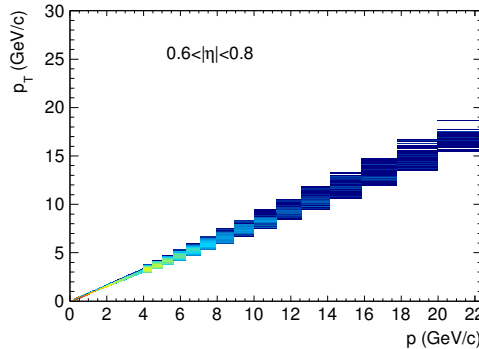


Figure 6.3: Correlation between p_T and p in $0.6 < |\eta| < 0.8$.

6.1.3 η dependence of particle fractions

Particle production as a function of p_T is independent of the particle rapidity:

$$y = \sinh^{-1} \frac{\sinh \eta}{\sqrt{1 + \frac{m^2}{p_T^2}}}. \quad (6.9)$$

Therefore for a given particle type with a given momentum, the particle yield scales with the rapidity width Δy defined as

$$\Delta y|_{\eta_1 < \eta < \eta_2} = y(\eta_2) - y(\eta_1). \quad (6.10)$$

⁶The path length dependence can not be fully removed by normalizing the energy loss to path length due to the residual $\ln N$ dependence in Eq. 3.27.

⁷In the correlation plot, for each momentum bin, the p_T mean ($\langle p_T \rangle$) and the standard deviation (σ_{p_T}) are calculated and related to the fraction A_k measured in the same momentum bin. The x-variable of the plot of A_k vs. p_T is thus $\langle p_T \rangle \pm \sigma_{p_T}$

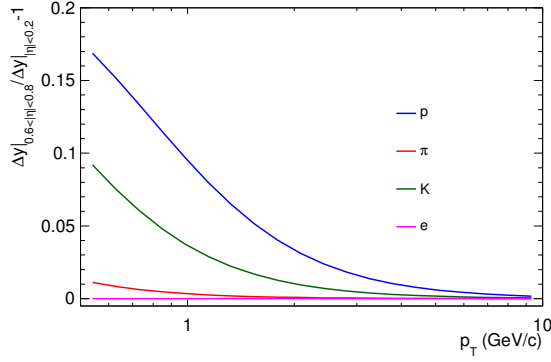


Figure 6.4: Relative difference of rapidity width at $0.6 < |\eta| < 0.8$ with respect to that at $|\eta| < 0.2$.

As can be seen in Fig. 6.4, for equal-width η -windows, the rapidity width is greater in larger rapidity region. For protons with p_T lower than 1 GeV/ c , the difference between $0.6 < |\eta| < 0.8$ and $|\eta| < 0.2$ is larger than 10%. As will be seen in Section 6.4, this effect is visible. For physical measurements in η -windows, this Δy -scaling has to be taken into account and corrected for (see Section 7.1.5).

6.2 Machinery

The TPC coherent fit is based on the maximum likelihood estimation method [Ken79]. It maximizes the function l . It is calculated with the measured two-dimensional particle distribution $f(p, \Delta)$ in bins of the momentum p and signal Δ (Fig. 6.1):

$$l = l_{\text{stat}} + l_{\text{reg}}, \quad (6.11)$$

with the statistical likelihood function

$$l_{\text{stat}} = \sum_i \sum_j \ln P \left(w_i f(p_i, \Delta_j); w_i \sum_k A_k(p_i) G(\Delta_j; \mu, \sigma(\mu, \mathbf{b})) \right), \quad (6.12)$$

$$\mu = \mu \left(\frac{p_i}{m_k}, \mathbf{a} \right), \quad (6.13)$$

and the local regularization term

$$l_{\text{reg}} = - \sum_i \sum_k \frac{\left[A_k(p_i) - \hat{A}_{ki} \right]^2}{2\delta_{ki}^2}. \quad (6.14)$$

Here the measured distribution f is normalized at each p , namely

$$\sum_j f(p_i, \Delta_j) = 1, \quad (6.15)$$

and w_i is the statistical weight of the integrated momentum bin i

$$w_i = \min\{C, N_i\}, \quad (6.16)$$

where C is a pre-defined number and N_i is the actual integrated count in the bin. The signal mean μ is parametrized with the ALEPH parametrization⁸ [Dec90]:

$$\mu(\beta\gamma; a_0, \dots, a_4) = a_0 \frac{a_1 - a_2 - \beta^{a_3} - \ln \left[1 + \frac{1}{(\beta\gamma)^{a_4} e^{a_2}} \right]}{\beta^{a_3}}. \quad (6.17)$$

The signal spread σ is similar to the one commonly used for the energy resolution of an electromagnetic calorimeter [Ber12]:

$$\sigma(\mu; b_0, \dots, b_2) = \left(\frac{b_0}{\sqrt{\mu}} + b_1 + \frac{b_2}{\mu} \right) \mu. \quad (6.18)$$

With the arguments $n \equiv wf$ and $\bar{n} \equiv w \sum_k A_k G$, the function $P(n; \bar{n})$ is the Poisson probability density function (p.d.f.)

$$P(n; \bar{n}) = \frac{\bar{n}^n e^{-\bar{n}}}{n!}. \quad (6.19)$$

In the regularization term Eq. 6.14, \hat{A}_{ki} is the particle- k fraction interpolated from neighboring values $A_k(p_{i-1})$ and $A_k(p_{i+1})$ using Neville's algorithm of polynomial interpolation [Wil92], and δ_{ki} is the error of $A_k(p_i)$ calculated as

$$\delta_{ki} = \frac{\sqrt{w_i \frac{A_k(p_i) + \hat{A}_{ki}}{2}}}{w_i}. \quad (6.20)$$

The minimization procedure is performed with the program TMinuit of the ROOT software [Bru97]. An algorithm, *the guided convergence*, is developed for an optimized convergence. It introduces an additional parameter λ as a guiding parameter in a series of iterative maximization of $l(\lambda) = l_{\text{stat}} + \lambda l_{\text{reg}}$ with λ increasing from 0 to 1.

In the following discussion the static and dynamic features of the method will be described. The regularized likelihood function and the models for the signal mean and spread will be investigated in Section 6.2.1, followed by the introduction of the guided convergence in Section 6.2.2.

6.2.1 Static features

The introduction of the statistical weight w_i instead of the direct use of N_i provides the functionality to cut off the dominant statistics, which affects the data sensitivity at bins of low statistics, without loss of information. For example, this is needed in case of a steeply falling spectrum. Such value of C of Eq. 6.16 can be chosen that they represent the equivalent statistics as an estimate of the combined statistical and systematic uncertainty of the fit, see discussion in Section 6.3.

⁸Compared to the original form, a_2 is redefined for a better numerical stability.

The ALEPH parametrization (Eq. 6.17) describes the hadron and electron signals at small and large $\beta\gamma$, respectively, with a smooth transition in between. In order to investigate the systematic effect due to the mean signal parametrization, an alternative model which decouples the hadrons and electrons is developed:

$$\mu(\beta\gamma; a_0, \dots, a_4) = \begin{cases} g(\beta\gamma; a_0, \dots, a_3), & \beta\gamma < s, \\ \min\{a_4, g(\beta\gamma, a_0, \dots, a_3)\}, & \beta\gamma > s, \end{cases} \quad (6.21)$$

where s is a pre-defined number and

$$g(\beta\gamma; a_0, \dots, a_3) = a_0 \frac{1 + a_2 \ln \beta\gamma + a_3 \ln \beta}{\beta^{a_1}}. \quad (6.22)$$

The hadron part Eq. 6.22 is based on the velocity-dependence of the Bethe-Bloch formula [Ber12] and s can be safely chosen as any value between the minimum ionizing and the relativistic rise regions. As will be shown in Section 6.4, the difference between the ALEPH and the modified Bethe-Bloch parametrizations is only relevant at the highest pion momentum region where for the latter there is no constraint from the higher $\beta\gamma$ region by the electrons.

For the signal spread we compare Eq. 6.18 to the following model

$$\sigma(\mu; b_0, \dots, b_2) = b_0 \mu^{b_1} + b_2. \quad (6.23)$$

The first model mimics the energy resolution of an electromagnetic calorimeter while the latter is motivated by a general statistical consideration. Both turn out to be consistent in the parameter space covered by the signal and therefore are considered equivalent.

The p.d.f. $P(n; \bar{n})$ gives the probability of an observed bin-count n with the expected value \bar{n} . The maximization of the likelihood function l_{stat} with a Poisson p.d.f. of bin-counts is the so-called binned maximum likelihood estimation (BML) [Ber12]. As an alternative, the Gaussian p.d.f.

$$P(n; \bar{n}, \sigma_n) = \frac{1}{\sigma_n \sqrt{2\pi}} e^{-\frac{(n-\bar{n})^2}{2\sigma_n^2}}, \quad (6.24)$$

which would have reduced l_{stat} to a χ^2 function, is only applicable for large \bar{n} . The χ^2 estimation at small statistics is problematic, as is shown in Fig. 6.5 from toy Monte Carlo simulations (ToyMCs) where binned distributions with different counts N_{true} are generated. The estimated counts N_{fit} by the χ^2 estimation are biased and more at smaller N_{true} , while the BML estimation gives unbiased results.

The maximization of the statistical term l_{stat} drives the free parameters $A_k(p_i)$, \mathbf{a} and \mathbf{b} so that the constructed one-dimensional distribution Eq. 6.1 describes the observed distribution in every p -bin simultaneously. As a comparison, an alternative method – the incoherent fit – will be discussed here. The incoherent fit fits the distribution in each p -bin individually. One can either treat the fraction, mean and spread in each p -bin as free parameters (type I), or treat the mean and spread instead as functions of the mass using Eqs. 6.3 and 6.4 with free parameters \mathbf{a} and \mathbf{b} locally defined in each p -bin (type II). The statistical likelihood functions (the momentum dependence of each quantity is implicit)

$$l_{\text{stat-I}} = \sum_j \ln P \left(w f(\Delta_j); w \sum_k A_k G(\Delta_j; \mu_k, \sigma_k) \right), \quad (6.25)$$

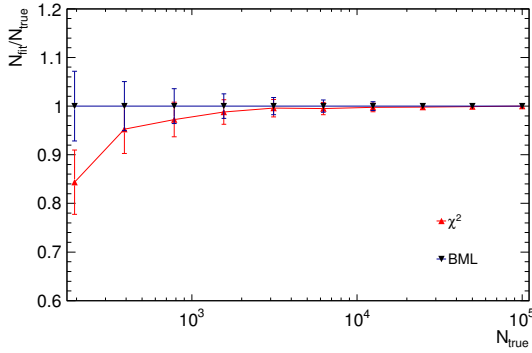


Figure 6.5: Comparison of the unbiasedness between the χ^2 and BML estimations. ToyMCs of binned distributions with different counts are used.

and

$$l_{\text{stat-II}} = \sum_j \ln P \left(wf(\Delta_j); w \sum_k A_k G(\Delta_j; \mu, \sigma(\mu, \mathbf{b})) \right), \quad (6.26)$$

$$\mu = \mu \left(\frac{p_i}{m_k}, \mathbf{a} \right), \quad (6.27)$$

respectively, are to be maximized for each p -bin, hence being *incoherent*. In practical models of μ and σ , the number of parameters is of the order of 10. Therefore type II is to be preferred due to a stronger constraint only if the number of particle species is considerably larger than 5, which is not the case in our problem and so we consider both incoherent treatments equivalent.

The advantage of the coherent fit (without regularization) over the incoherent one is demonstrated in a ToyMC where a (p, Δ) -distribution is generated with given realistic forms of μ and σ and constant but realistic fractions. The same forms are used in maximizing the coherent and incoherent (type II) l_{stat} so that the comparison between the extracted fractions is parametrization-independent and only depends on the mechanism how the intra-bin information is organized. Figure 6.6 a-b compares the corresponding extracted fractions to the true values. It shows a dramatic improvement of the unbiasedness when the intra-correlation between p -bins is used. Inspecting the generated distribution at a given momentum (Fig. 6.6 c-d) it is observed that the bias is due to the ambiguity of two overlapping distributions. If the two distributions have the same mean, the unregularized coherent fit becomes also biased. It can be seen in Fig. 6.6b that large biases happen at the signal crossings of p-e, π -K, π -p and p-K (see also Fig. 6.1). This motivates the introduction of the regularization term.

The regularization term l_{reg} reduces the fluctuations of the fractions $A_k(p_i)$ caused by the ambiguity of overlapping distributions. It uses the correlation between neighboring p -bins and require $A_k(p_i)$ to be continuous modulo statistical fluctuations: the χ^2 -form of l_{reg} requires that the deviation of $A_k(p_i)$ from the expectation is Gaussian (the factor 2 in the denominator of l_{reg} is for a consistent log-likelihood interpretation which is necessary for a proper error definition). The expected value \hat{A}_{ki} is the interpolated one from neighboring points using polynomial interpolation with the degree determined by the number of

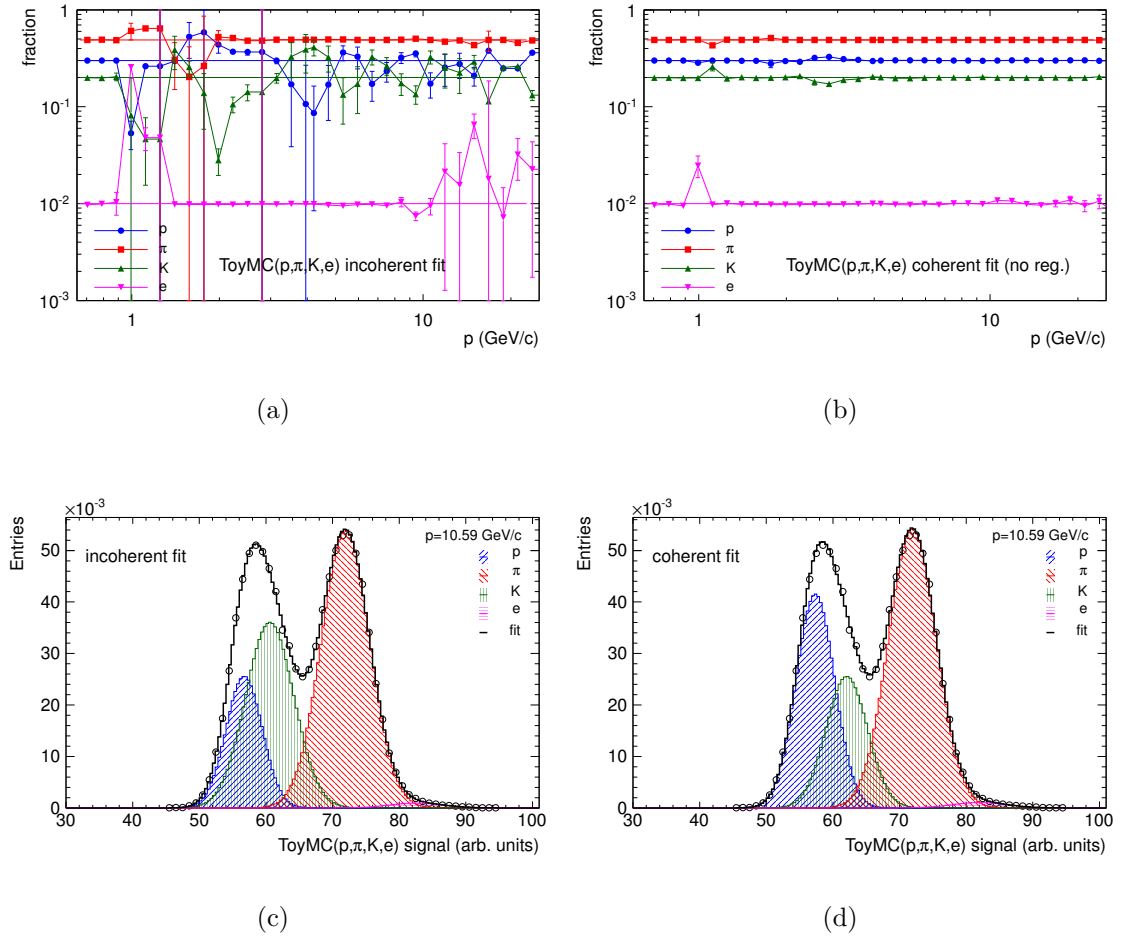


Figure 6.6: (a)-(b) Extracted fractions as functions of momentum. Connected points are the extracted values and lines are ToyMC input. (c)-(d) Fit to generated distribution at a given momentum. (a) and (c) are by the incoherent fit. (b) and (d) are by the coherent fit without regularization. A ToyMC of a (p, Δ) -distribution is used.

involved points⁹ [Wil92], namely the range of the neighborhood, which also determines the correlation length of the regularized $A_k(p_i)$. In order to avoid artificial correlation, short range of neighborhood is preferred. Different short ranges, $\pm n$ bins with $n = 1, 2$, have been studied and it turns out that higher order polynomial is too flexible and can easily follow unphysical spike structures of the unregularized $A_k(p_i)$. Therefore direct neighbors, namely ± 1 bins, are used. Because of additional statistics from neighboring bins, the statistical errors of $A_k(p_i)$ are reduced. Figure 6.7 compares the extracted fractions by the coherent fit with and without regularization using an ALICE MC production (LHC11b10a), where the dependence of the particle fraction on the momentum is non-trivial. The δ -function-like unphysical estimates at the signal crossing points are smoothed out and the statistical fluctuation is clearly reduced at large momenta where

⁹An alternative procedure [Iva12] which fits the neighboring points with polynomials of fixed order is tested and yields equivalent results.

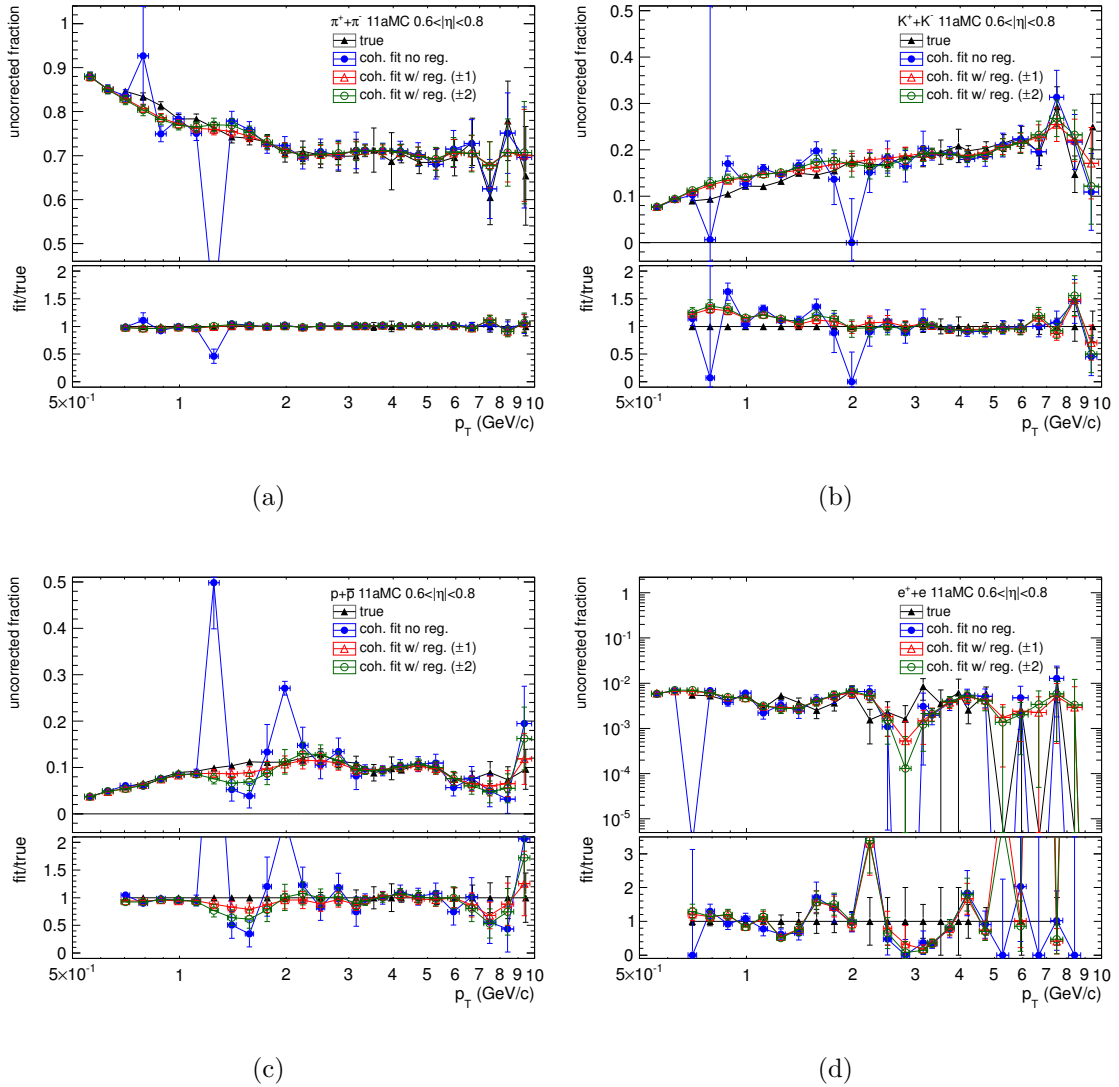


Figure 6.7: Extracted fractions by the coherent fit with and without regularization. (a)-(d) compare the extracted fractions for pions, kaons, protons and electrons, respectively, to the MC truth at the reconstruction level. Different regularization ranges ($n \pm 1, 2$) are compared. The biases at the signal crossing points are reduced to less than 20%. The ALICE MC production LHC11b10a is used.

less statistics is available. As is shown in Figs. 6.7 (b) and (c), between two crossing points there can be a residual bias of about 20% because this region spans over several bins without a solid internal constraint¹⁰ (see Section 6.5 for more discussion). Note that outside the signal crossing region the regularized and unregularized results are consistent.

¹⁰An MC study is performed, where the true signal mean and width are plugged in in Eq. 6.11 and held fixed in the maximization procedure. In this case a residual bias of a similar order persists, which indicates that the residual bias is due to the diminishing separation power rather than imperfect parametrizations of the signal mean and width.

6.2.2 Dynamic features

The convergence of the maximization of the regularized likelihood function Eq. 6.11 with a total number of free parameters about $N_s N_p \sim 120$ is non-trivial, where the number of particle species $N_s = 4$ and the number of momentum bins $N_p \sim 30$. The strategy is to first use the incoherent fit to obtain the initial values¹¹ of the fractions $A_k(p_i)$, and then to maximize

$$l(\lambda) = l_{\text{stat}} + \lambda l_{\text{reg}} \quad (6.28)$$

in iterations with λ increasing from 0 to 1. The parameters at the l -maximum obtained with λ_j will be used as the initial values in the next iteration for $l(\lambda_{j+1})$. The evolution of λ is determined by the ratio of $l_{\text{stat}}/l_{\text{reg}}$ right after the first iteration where $\lambda_0 = 0$, namely where only l_{stat} is maximized:

$$\lambda_1 = \min \left\{ \frac{1}{2}, 2^{\lceil \ln_2 \frac{l_{\text{stat}}}{l_{\text{reg}}} \rceil} \right\}, \quad (6.29)$$

$$\lambda_{j+1} = 2\lambda_j, \text{ for } \lambda_j \neq 1, \quad (6.30)$$

where $\lceil x \rceil$ is the operator to calculate the smallest integer larger than x . The evolution is designed in such a way that the influence of the regularization term gradually increases and λ guides the parameters from the minimum of l_{stat} to that of $l_{\text{stat}} + l_{\text{reg}}$.

To illustrate the convergence behavior of the maximization, Table 6.1 shows λ , l_{stat} and l_{reg} of Eq. 6.28 after each iteration of the guided convergence, obtained from a fit to real data (Section 6.4). It can be seen that the regularization term l_{reg} is gradually maximized at an expense of smaller l_{stat} , resulting in an overall increase of the regularized likelihood function $l = l_{\text{stat}} + l_{\text{reg}}$.

j	λ_j	$-l_{\text{stat}}$	$-l_{\text{reg}}$	$-(l_{\text{stat}} + l_{\text{reg}})$
0	0	4671	3093	7764
1	$1/2$	4685	11	4696
2	1	4688	6	4694

Table 6.1: Iterations in the guided convergence. Note the minus signs in front.

6.3 Error definition

First we consider the case where there is no effective weighting, namely $w_i \equiv N_i$ (Eq. 6.16). The covariance matrix of the estimated parameters provided by TMinuit is the inverse of the Hessian matrix of $-l$ (Eq. 6.11) at the l -maximum. It approximates the minimum variance bound in the large sample limit (which we assume to be always the case). These errors are statistical.

¹¹The initial values of the parameters **a** (Eq. 6.17) for the signal mean can be obtained from a fit of Eq. 6.17 to 5 points of (Δ, p) , which are read off from the signal distribution. Those of the parameters **b** (Eq. 6.18) for the signal spread can be taken initially for a constant resolution.

When effective weighting sets in, the TMinuit errors correspond to the nominal statistics set by C ($< N_i$) and therefore we see an artificial inflation of the statistical errors. Even though the true statistical errors can be calculated [Sol64], we can use this equivalent statistics approach to roughly estimate the systematic error of the coherent fit. By fitting to a simulated sample with very large statistics one can estimate the systematic errors by comparing the fit results and the simulation input. Then adjust the weight so that the TMinuit errors represent the difference. When this weight is applied to data, the TMinuit errors represent the combined statistical and systematic uncertainties of the fit.

Another way to estimate the systematic error of the coherent fit is to use different acceptable configurations (signal mean and spread models, for example) to probe the parameter space which is constrained by data. The variation of the extracted fractions defines the range of the acceptable results.

6.4 Data analysis results

The TPC coherent fit is applied to a data sample of primary particles from the LHC proton-proton collisions at the center-of-mass energy $\sqrt{s} = 2.76$ TeV (period LHC11a). The results will be discussed systematically in this section.

The statistical weight w_i with $C = 10^4$ is shown in Fig. 6.8.

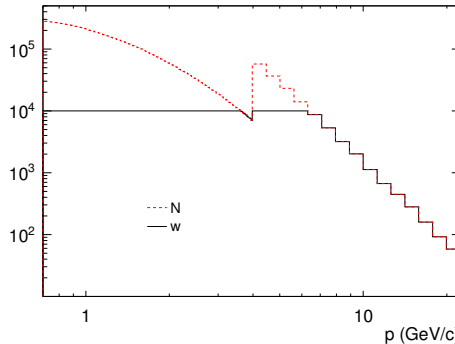


Figure 6.8: Statistical weight w with $C = 10^4$ (black) as a function of momentum ($0.6 < |\eta| < 0.8$). The actual count N is shown as the red dashed histogram. The bin width below 4 GeV/ c is 1/10 of the one above.

The extracted parameters for the mean signal with the ALEPH parametrization Eq. 6.17 are shown in Table 6.2. The corresponding mean signals are shown in Fig. 6.9. Figure 6.10 (*left*) compares the extracted mean signals to those by the modified Bethe-Bloch parametrization Eqs. 6.21–6.22. As can be seen, the difference is less than 0.2% except in the $\beta\gamma$ -region between 20 GeV pions and electrons ($10^2 < \beta\gamma < 10^3$). Figure 6.10 (*right*) compares the extracted mean signals in the $|\eta|$ ranges 0–0.2 and 0.6–0.8. The latter is larger by 2% due to the residual path length dependence (see Footnote 6).

i	0	1	2	3	4
a_i	3.75(9)	10.3(2)	-12.6(3)	2.441(5)	2.23(6)

Table 6.2: Fitted parameters of the ALEPH parametrization ($0.6 < |\eta| < 0.8$). The number in the parenthesis is the statistical uncertainty in the last digit.

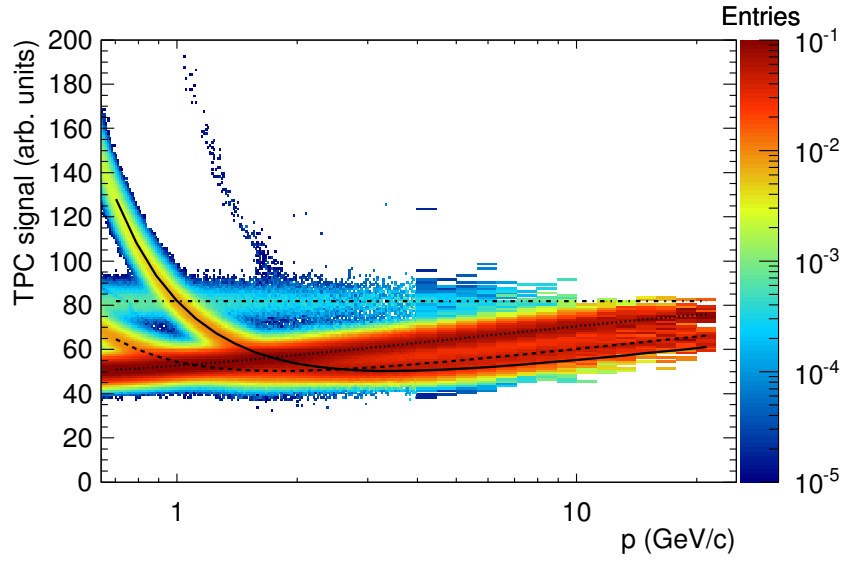


Figure 6.9: Mean signal obtained by the coherent fit, shown as the black curves overlaid on top of the measured signal distribution ($0.6 < |\eta| < 0.8$).

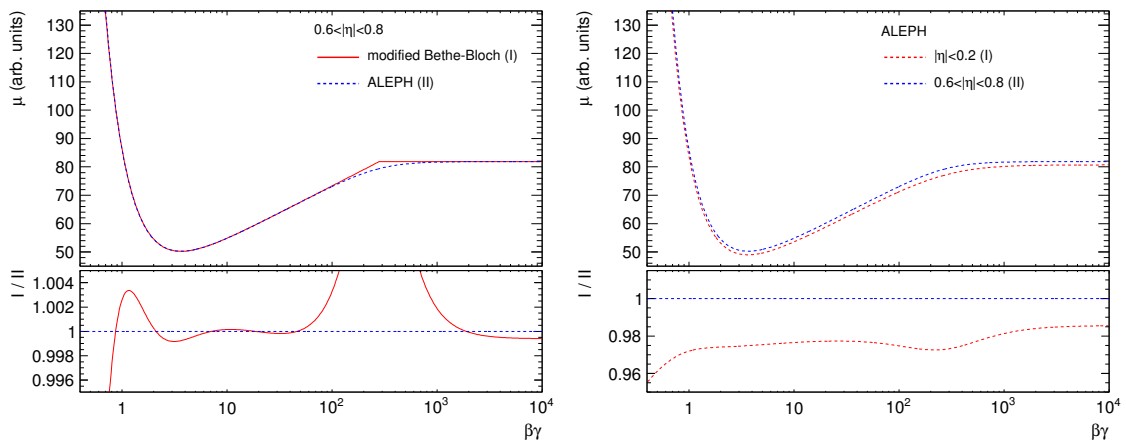


Figure 6.10: Comparison of the fitted mean signals (*left*) between the ALEPH and the modified Bethe-Bloch parametrizations and (*right*) between different η -windows.

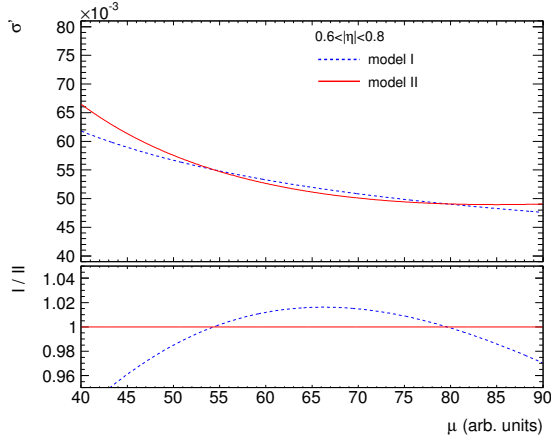


Figure 6.11: Comparison of the fitted resolutions between the two parametrizations, Eqs. 6.18 and 6.23 (model I and II, respectively).

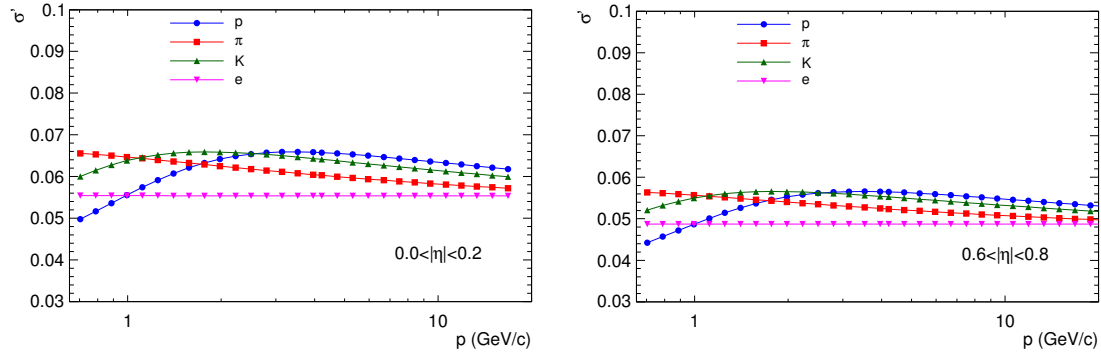


Figure 6.12: TPC signal resolution obtained by the coherent fit as a function of momentum for different particle species in (*left*) $|\eta| < 0.2$ and (*right*) $0.6 < |\eta| < 0.8$.

The extracted signal resolution, $\sigma' \equiv \sigma/\mu$, by the two models, Eqs. 6.18 and 6.23 (model I and II, respectively), are shown in Fig. 6.11. The corresponding extracted fractions are not sensitive to the 2% difference in the region $40 < \mu < 80$ of dominant statistics and are thus consistent. The resolution in different η -windows are shown in Fig. 6.12. The difference is due to the systematic effects discussed in Section 6.1.

A comparison between the unregularized and regularized particle fractions is shown in Fig. 6.13. As can be seen the statistical errors are reduced by regularization as expected from the discussion in Section 6.2.1. On the other hand, no bias due to the regularization is observed.

The fit results are projected in different momentum bins in Fig. 6.14. As can be seen the fit describes the data well in both the positions and the shapes of the signals.

The fractions of pions, kaons, protons and electrons in the η -windows are shown in Fig. 6.15. The error bar represents a combination, using the equivalent statistics approach with $C = 10^4$ in w_i (Section 6.3), of the statistical error and the partial systematic error estimated from MC. It is mostly systematical at low p_T and statistical at high p_T . The errors box represents an additional estimate of the systematic error by variations to the mean signal model (ALEPH and the modified Bethe-Bloch) and the signal spread model (model

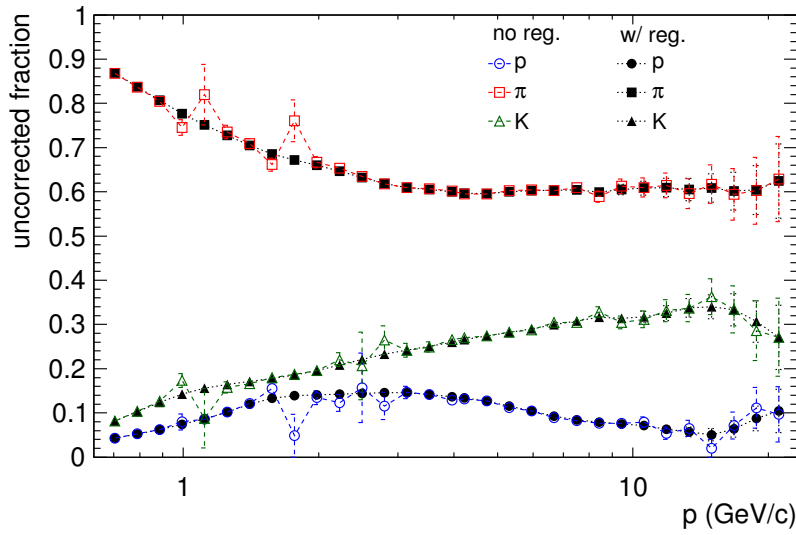


Figure 6.13: Comparison between unregularized and regularized particle fractions ($0.6 < |\eta| < 0.8$, the electron fraction which is at per mil level is not shown).

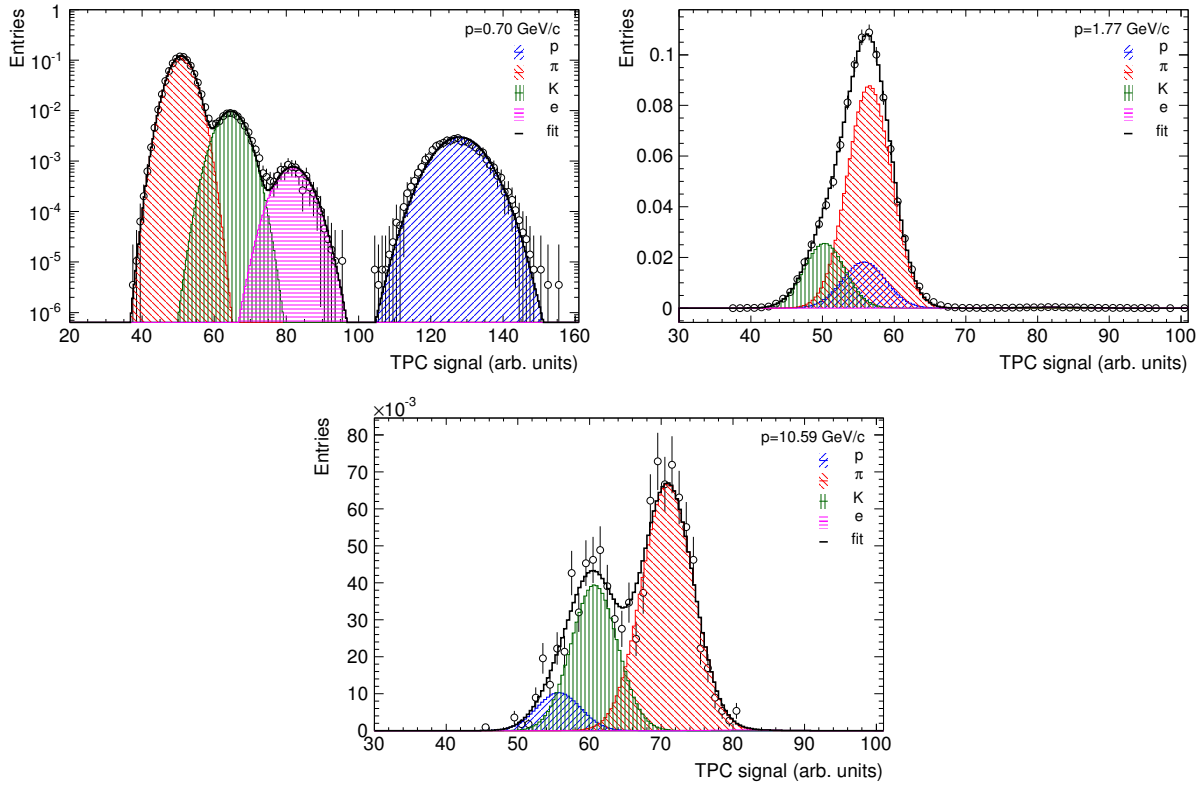


Figure 6.14: The coherent fit results projected at different momentum bins ($0.6 < |\eta| < 0.8$).

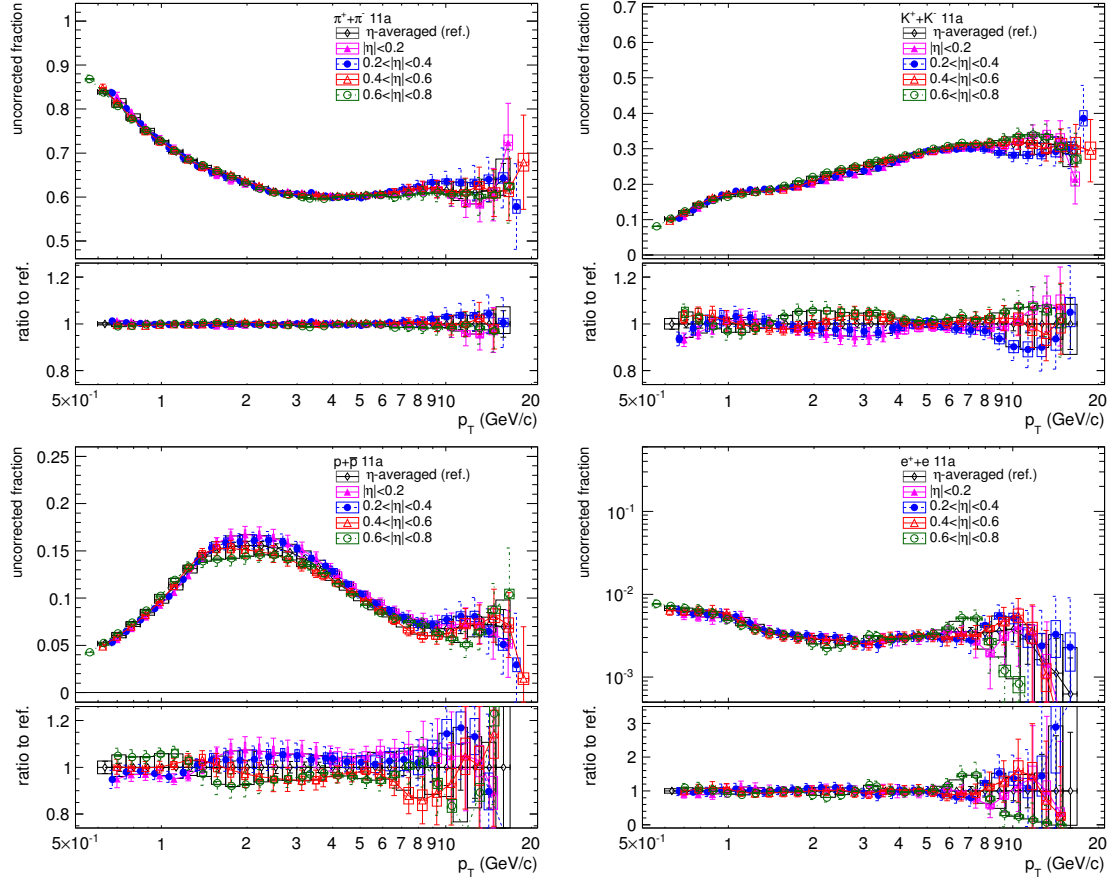


Figure 6.15: Uncorrected particle fractions from proton-proton collisions at $\sqrt{s} = 2.76$ TeV in η -windows. See text for the interpretation of the error bars and error boxes.

I and II). The fractions are not corrected for detection efficiencies (see Section 7.1.4) nor for Δy -scaling (see Section 6.1.3). The relative η -dependent variation of the detection efficiencies is smaller than 3% while the variation of the Δy -scaling at $p_T < 1 \text{ GeV}/c$ is larger than 10%. As a result we see Δy -ordering at low p_T when comparing the uncorrected fractions, for protons at $p_T < 1 \text{ GeV}/c$ and kaons around $p_T 0.5 \text{ GeV}/c$ — the fraction in larger $|\eta|$ is higher than that in lower $|\eta|$. At larger p_T the η -variation of the uncorrected fractions is less than 5% and 10% at p_T below and above 10 GeV/c , respectively. It is mainly due to the systematic uncertainties of the fit and therefore provide a realistic estimate of the systematic error with the help of the cross reference between η -windows.

Without the $\Delta y/\Delta\eta$ correction, the η -averaged fraction only serves as a technical observable for performance because of the intrinsic η -dependence of the particle fractions, especially at low p_T for protons. Nevertheless the principle of the averaging technique is the same through out this work. The averaged value is the arithmetic mean of individual values in η -windows. The individual error bars are propagated to the averaged ones assuming uncorrelated measurements. The averaged error box is the quadratic sum of two parts: the η -variation of the fractions and the propagated mean error from individual error boxes. The averaged error bars represent the combination of partial systematic uncertainty and statistical uncertainty, dominating at low and high p_T , respectively. The averaged error boxes represent a realistic estimate of the systematic uncertainty of the fit.

6.5 TPC coherent fit with subsidiary particle identification

The TPC coherent fit is a method using only the TPC signals of particles in the momentum range from hundred MeV/c to above 20 GeV/c. In ALICE, there are other particle identification detectors optimized for different momentum regions. In the momentum range 1 – 3 GeV/c, where the fraction estimated by the TPC coherent fit can have residual bias up to 20% due to the TPC signal crossings, the TOF detector [Del00a, Aam08] is designed to provide precise particle identification. This section discusses how the TPC coherent fit can be combined with other particle identification detector(s), which in the current case is the ALICE TOF detector. Note that the method discussed below is general for any subsidiary particle identification. For example, the TRD truncated mean signal (see Chapter 5), which has a different $\beta\gamma$ dependence due to a different gas composition, can be used in the same procedure once it is integrated in the ALICE data production.

Suppose at an arbitrary momentum p , out of a sample of N^{tot} particles, the TOF detector identifies N_k^{TOF} particles of type- k uniquely. One can remove the TOF-identified samples for different particle types from N^{tot} , perform the TPC coherent fit in the remaining sample, which is denoted as $N^{\text{TOF}} \equiv N^{\text{tot}} - \sum_k N_k^{\text{TOF}}$, and estimate the remaining fraction of particle type- k to be A_k^{TOF} . The overall fraction of particle type- k in N^{tot} reads

$$A_k^{\text{tot}} = \frac{N_k^{\text{TOF}} + N_k^{\text{TOT}}}{N^{\text{tot}}} = \frac{A_k^{\text{TOF}} N^{\text{TOF}} + N_k^{\text{TOT}}}{N^{\text{tot}}} \quad (6.31)$$

$$= A_k^{\text{TOF}} \left(1 - \sum_i A_i^{\text{TOT}} \right) + A_k^{\text{TOT}}, \quad (6.32)$$

where $N_k^{\text{TOF}} \equiv A_k^{\text{TOF}} N^{\text{TOF}}$ and the TOF fraction A_k^{TOF} is defined as

$$A_k^{\text{TOF}} \equiv N_k^{\text{TOF}} / N^{\text{tot}}. \quad (6.33)$$

In the case of perfect TOF identification, the statistical uncertainty of the estimated overall particle fraction scales as $\sqrt{N^{\text{TOF}}}/N^{\text{tot}}$, while the systematic uncertainty is weighted by a factor of $N^{\text{TOF}}/N^{\text{tot}}$ (assuming $\delta_{\text{stat.}} A_k^{\text{TOF}} \sim 1/\sqrt{N_k^{\text{TOF}}}$ and $\delta_{\text{sys.}} A_k^{\text{TOF}} \sim \text{const.}$). In this sense, compared to the pure TPC coherent fit (“no TOF” analysis) where $N^{\text{TOF}} = N^{\text{tot}}$, both statistical and systematic uncertainties of A_k^{tot} are reduced by increasing N^{TOF} . In terms of relative uncertainties, starting from Eq. 6.32, we have

$$\begin{aligned} \frac{\delta A_k^{\text{tot}}}{A_k^{\text{tot}}} &= \frac{\delta A_k^{\text{TOF}}}{A_k^{\text{TOF}}} \frac{A_k^{\text{TOF}} (1 - \sum_i A_i^{\text{TOT}})}{A_k^{\text{tot}}} \\ &= \frac{\delta A_k^{\text{TOF}}}{A_k^{\text{TOF}}} \frac{A_k^{\text{tot}} - A_k^{\text{TOT}}}{A_k^{\text{tot}}} \\ &= \frac{\delta A_k^{\text{TOF}}}{A_k^{\text{TOF}}} \left(1 - \frac{A_k^{\text{TOT}}}{A_k^{\text{tot}}} \right) \\ &= \frac{\delta A_k^{\text{TOF}}}{A_k^{\text{TOF}}} (1 - \epsilon_k^{\text{TOT}}). \end{aligned} \quad (6.34)$$

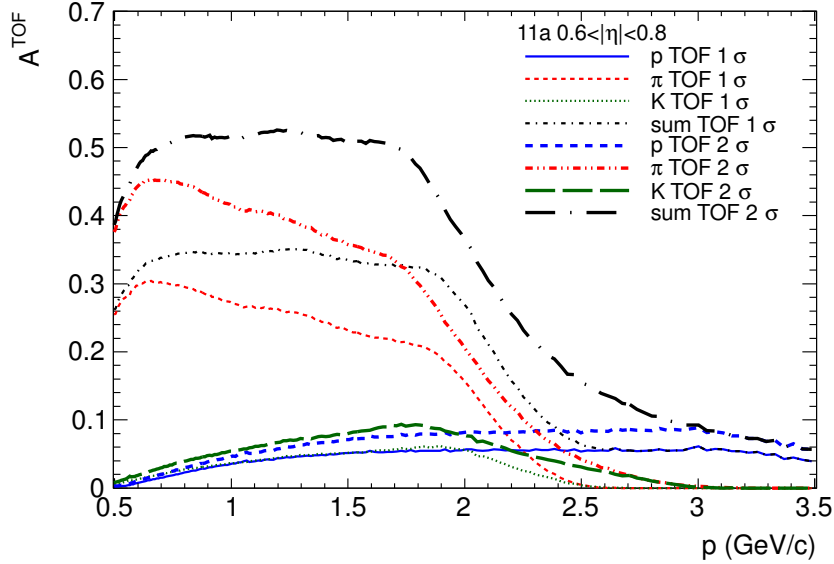


Figure 6.16: TOF fractions (defined in Eq. 6.33) obtained from data (period 11a $0.6 < |\eta| < 0.8$) as a function of momentum for the cuts (see text for details) with 1– and 2– σ inclusion, respectively. Also shown are the sum of TOF fractions of pions, kaons and protons.

where

$$\epsilon_k^{\text{TOF}} \equiv A_k^{\text{TOF}} / A_k^{\text{tot}} \quad (6.35)$$

is the TOF identification efficiency for particle type- k . Equation 6.34 implies that the relative uncertainty by the TPC coherent fit, when propagated to that of the overall fraction, is reduced by a factor equal to the TOF efficiency.

On the other hand, in practice the TOF identification deteriorates as N^{TOF} goes up, as a consequence of increasing contamination as one loses the TOF particle identification cuts. Therefore, the inclusion of the TOF identification to the TPC coherent fit is necessary only if the TOF identification efficiency is large when the contamination is kept under the TPC coherent fit systematic uncertainty. This condition is assumed to hold for the equivalent class of the TOF identification cuts used in this work (described later in this section) and the variation within this class is taken to be a systematic uncertainty.

The advantage of this method to include TOF in the framework of TPC coherent fit, compared to the conventional treatment of using single detector in different momentum regions, is that, firstly the requirement on statistics is minimum while the use of information is maximum, and secondly there is no need for the efficiency correction (including detection and reconstruction efficiencies and acceptance) of the TOF detector because the overall sample N^{tot} does not depend on the TOF identification.

In the following the details of the method including the TOF identification cuts and the method performance are presented.

In this work, the TOF identification is used for pions, kaons and protons¹². The cut for

¹²Not for electrons because an exclusion cut for the electron, despite its small amount (per mil level),

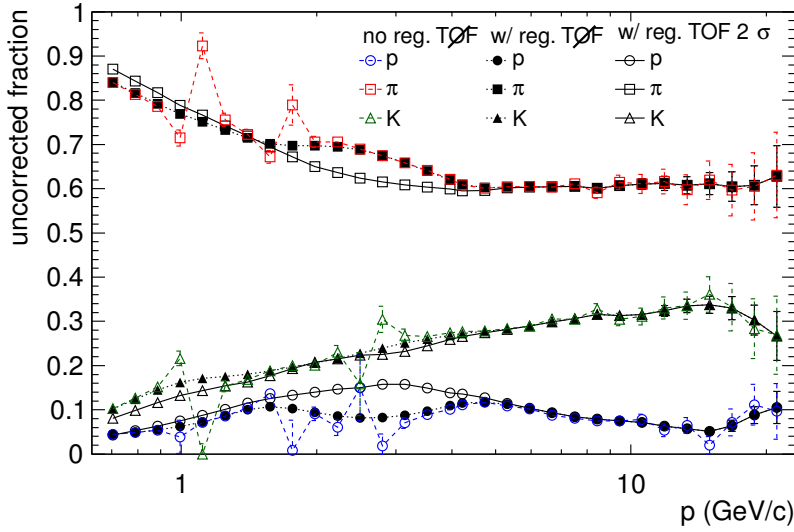


Figure 6.17: The extracted remaining fractions by the TPC coherent fit A_k^{TOF} with (“w/ reg. TOF”) and without (“no reg. TOF”) regularization and the resulting calculated overall fractions A_k^{tot} (“w/ reg. TOF 2σ ”). The TOF cut with 2σ inclusion is used. (period 11a $0.6 < |\eta| < 0.8$)

any particle type- k is the intersection of a $n\sigma$ ($n = 1, 2$) inclusion cut for type- k and a 4σ exclusion cut for other particle types. The TOF fraction defined in Eq. 6.33 is shown in Fig. 6.16 for the cuts with $1-$ and $2-$ σ inclusion.

For the TOF cut with 2σ inclusion, the remaining fractions A_k^{TOF} and the overall fractions A_k^{tot} are shown in Fig. 6.17. Also shown is the pre-regularized A_k^{TOF} which indicates the positions of TPC signal crossings. It can be seen that the TOF identification is effective in these crossing regions.

According to Eq. 6.35, the TOF identification efficiency ϵ_k^{TOF} can be estimated from Figs. 6.16 and 6.17. The values are shown in Table 6.3, indicating that with the TOF identification, the relative uncertainty of the kaon estimates is reduced by about 40% below 2 GeV/ c and that of the protons by 50 – 60% below 3 GeV/ c .

p (GeV/ c)	1	2	3
π	0.51	0.31	0
K	0.43	0.38	0
p	0.63	0.57	0.49

Table 6.3: TOF identification efficiency (defined in Eq. 6.35) after a cut of 2σ inclusion and 4σ exclusion in period 11a $0.6 < |\eta| < 0.8$.

The overall fractions A_k^{tot} obtained by the TOF inclusion with cuts with $1-$ and $2-\sigma$ cuts, respectively, and also by the “no TOF” method are compared in Fig. 6.18. The variation

will much reduce the TOF efficiencies for other particle types. However electrons are still modeled in the TPC coherent fit and their fraction can be extracted.

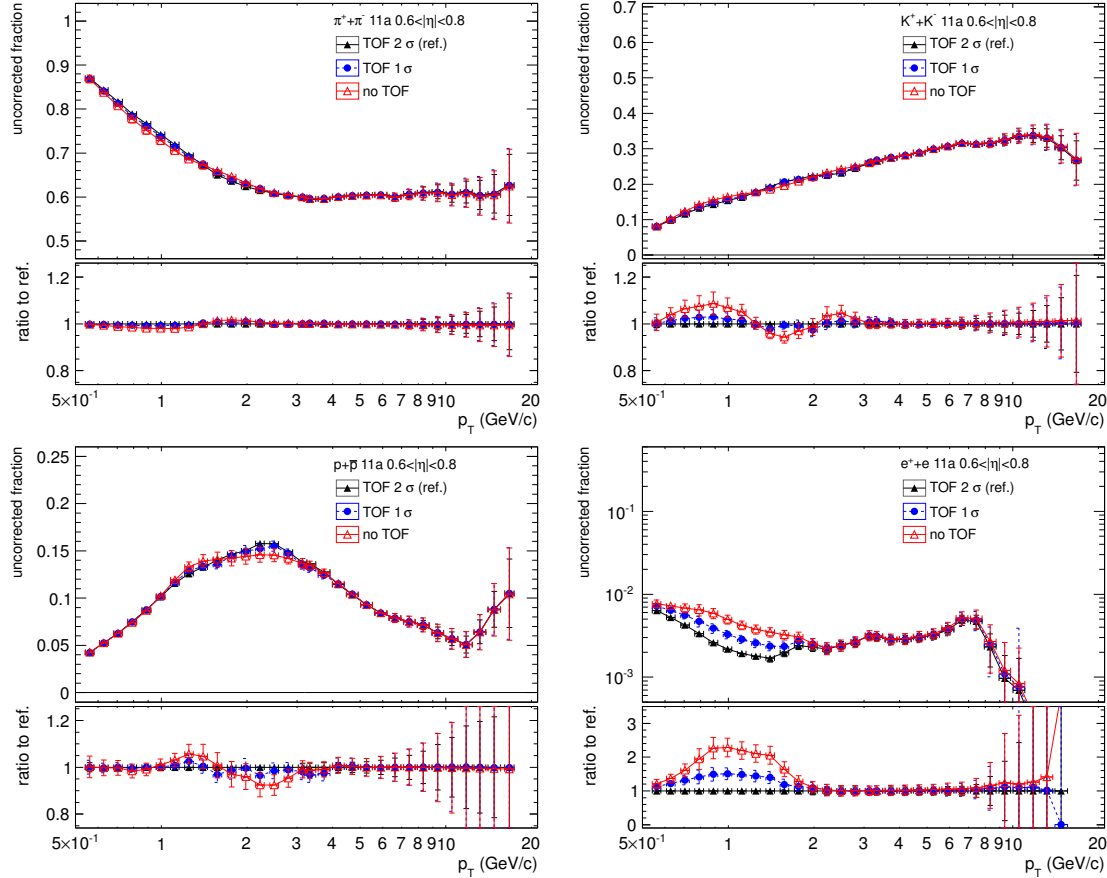


Figure 6.18: Comparison among overall fractions A_k^{tot} obtained by TOF inclusion with cuts with 1– and 2– σ inclusion, respectively, and also by the “no TOF” method (period 11a $0.6 < |\eta| < 0.8$).

due to the TOF inclusion cuts is smaller than 2%¹³. The two TOF cuts are considered to be equivalent and this variation is taken as a systematic uncertainty. The change introduced by the TOF inclusion with respect to the “no TOF” method is up to 10% for kaons and protons in the crossing regions, as is expected as a reduction of the residual bias.

As a technical comparison, the η -averaged fractions with TOF inclusion and by the “no TOF” method are compared in Fig. 6.19. In addition to the systematic error discussed in Section 6.4, the fraction variation in a given η -window due to the change of the TOF cuts is included as another systematic uncertainty which is in the end propagated to the η -averaged error box. The difference between the two methods resembles that in Fig. 6.18.

As a further proof of principle, the improvement by the TOF identification is shown in MC as follows. The same procedure of the TPC coherent fit with TOF inclusion is performed. The resulting TOF fractions by different TOF cuts are shown in Fig. 6.20. Considering also the overall particle fractions in MC (see Fig. 6.7), it can be concluded

¹³The large variation for electrons due to different TOF cuts stems from the contamination of electrons in other particle types. Because there is not electron exclusion cut, the $N_{\pi,K,p}^{\text{TOF}}$ samples contains electrons which can be ignored for the hadron fractions, but is significant for the electron fraction.

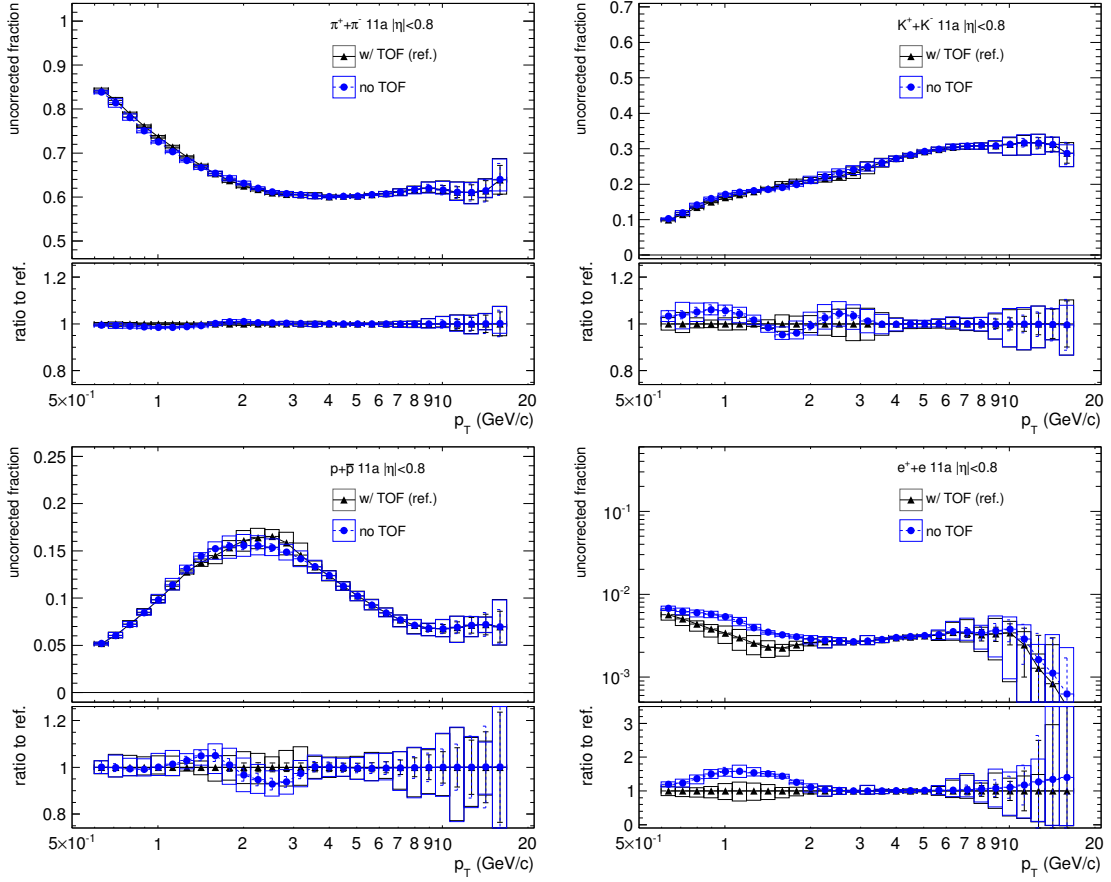


Figure 6.19: Comparison between the η -averaged fractions by the TOF inclusion and the “no TOF” method.

that the TOF efficiencies in MC is consistent with those in data by the same TOF cuts. The extracted particle fractions are compared to the “no TOF” method and to the MC truth in Fig. 6.21. As can be seen the residual bias is much reduced¹⁴.

6.6 Summary

Before applying the TPC coherent fit in physics analysis (Chapter 7), a short summary is in order. Whenever TOF information is available, the TPC coherent fit is applied with TOF identification as discussed in Section 6.5. The machinery of the fit is summarized in Section 6.2 and discussions of the error definition can be found in Section 6.3 and the last part of Section 6.4. In case with TOF identification, the TOF cut variation defines additional systematic errors.

¹⁴The introduced bias on the electron fraction is expected as discussed previously for Fig. 6.18.

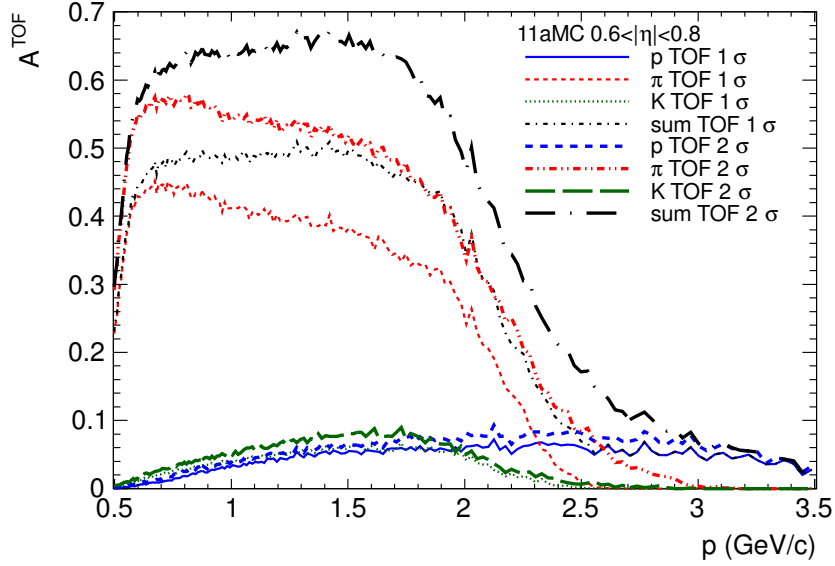
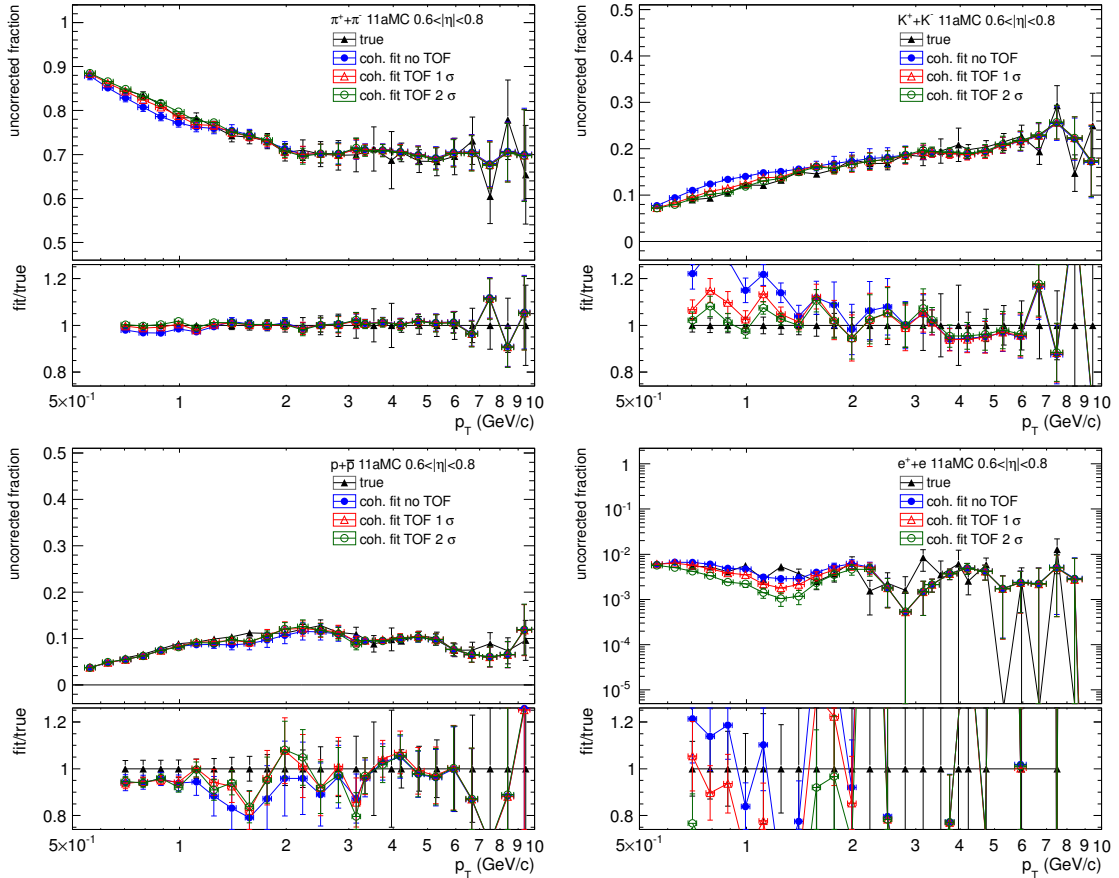

 Figure 6.20: TOF fractions obtained from MC (LHC11b10a $0.6 < |\eta| < 0.8$).


Figure 6.21: Extension of the comparison in Fig. 6.7. Extracted fractions by the “no TOF” method and by the TOF inclusion with different cuts are compared to the MC truth.

Chapter 7

Pion, kaon, and proton production in pp and Pb–Pb collisions

The production of (unidentified) charged particles in Pb–Pb collisions at $\sqrt{s_{\text{NN}}} = 2.76$ TeV has been measured in the transverse momentum p_{T} range $0.3 < p_{\text{T}} < 20$ GeV/ c (see Fig. 1.8) [Aam11a] and $0.15 < p_{\text{T}} < 50$ GeV/ c [Abe13d] in ALICE. Measurements of π^{\pm} , K^{\pm} , p and \bar{p} production in the p_{T} regions from 100, 200, 300 MeV/ c up to 3, 3, 4.6 GeV/ c , respectively, have been performed [Abe13a]. In this work the measurements for the identified particles are extended to pp collisions at $\sqrt{s} = 2.76$ and 7 TeV, as well as to Pb–Pb collisions at $\sqrt{s_{\text{NN}}} = 2.76$ TeV in the p_{T} range from 600 MeV/ c to about 20 GeV/ c , with focus on the moderate and high p_{T} regions, where baryon anomaly and jet quenching, respectively, are the characteristic phenomena (see Section 1.2).

The measurement is performed with the TPC coherent fit as described in Chapter 6 (for a short summary see Section 6.6). The p_{T} spectra of primary pions, kaons, and protons, which are produced from the collisions and are not weak decay products, are derived from the extracted particle fractions. This measurement offers a unified picture of identified particle production in an unprecedentedly large p_{T} range covering regions dominated differently by multi-parton soft processes and/or parton-parton hard scattering. The following sections describe the procedure and present the results of the measurements.

7.1 Procedure

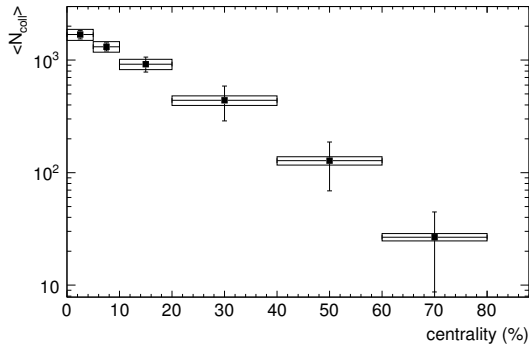
7.1.1 Data sets and cuts

Individual data sets from the LHC periods 10d, 10h and 11a are used. The following sequential event cuts (abbreviations in parentheses) select the minimum bias collision candidates:

1. minimum bias trigger selection (MB),
2. successful primary vertex reconstruction (Vtx),

period	10d	10h	11a
system	pp	Pb–Pb	pp
$\sqrt{s_{(NN)}}$ /TeV	7	2.76	2.76
data $N_{\text{ev}} _{(\text{MB} \& \text{Vtx} \& Z_{\text{vtx}})} / 10^6$	127	15	53
MC id.	10f6a + 10f6	11a10a_bis	11b10a
MC $N_{\text{ev}} _{(\text{MB} \& \text{Vtx} \& Z_{\text{vtx}})} / 10^6$	169	1.3	2.8

Table 7.1: Summary of data sets used in the particle production analysis.

Figure 7.1: $\langle N_{\text{coll}} \rangle$ as a function of the event centrality. Data from [Abe13b].

3. the reconstructed primary vertex being located within ± 10 cm along the beam axis about the nominal collision point (Z_{vtx}).

Table 7.1 summarizes the collision systems, the center of mass energies, the number of the selected minimum bias events $N_{\text{ev}}|_{(\text{MB} \& \text{Vtx} \& Z_{\text{vtx}})}$ (recorded after the Z_{vtx} cut) and the corresponding ALICE MC production used in this analysis. The minimum bias Pb–Pb events are divided into six centrality intervals [Abe13b] from the 0–5% to the 60–80% most central collisions, in terms of the percentage of the total hadronic cross section. The event centrality is related to the average number of binary nucleon-nucleon collisions $\langle N_{\text{coll}} \rangle$ as is shown in Fig. 7.1.

In order to select primary particles and ensure tracking and PID qualities, standard track cuts are applied. The details are shown in Appendix B.

7.1.2 Systematic effects of the event cuts on the p_{T} -spectra

The p_{T} -distribution of the particles from the events selected by the event cuts may be distorted with respect to the original one produced in the collisions¹. The change of the normalized p_{T} -distribution in pp collisions due to the event cuts is demonstrated in Fig. 7.2 using MC productions. The ratios of $1/N_{\text{ev}} \cdot dN/dp_{\text{T}}$ between the generated primary particles recorded after different cuts are shown. As can be seen, the Vtx and Z_{vtx} cuts change the shape of the p_{T} -spectra only at the per mil level which can be ignored, while the Vtx cut additionally changes the normalization.

¹The discussion here generalizes the so-called “bin-0” issues, where events without reconstructed vertexes are considered.

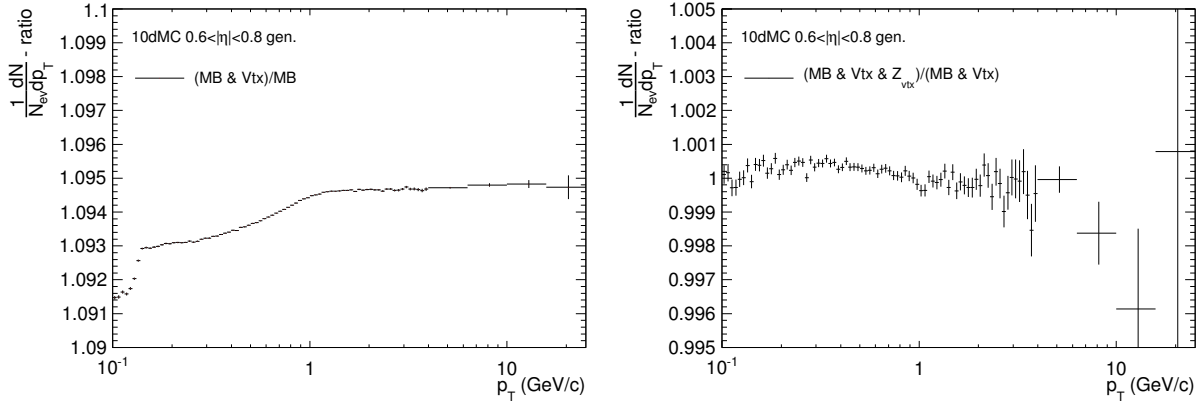


Figure 7.2: Ratios between normalized p_T -distributions after different event cuts. Generated primary particles in MC are used.

The approximately p_T -independent ratio of the normalized p_T -distributions before and after the Vtx cut can be estimated by the inverse ratio of the corresponding numbers of events as is shown in Tab. 7.2. As a comparison, Tab. 7.3 shows that the effect of the Z_{vtx} cut on the spectrum is simply a scaling with the number of events.

MC	$r_1 \equiv \frac{1}{N_{\text{ev}}} \frac{dN}{dp_T}$ -ratio (MB & Vtx)/MB	$r_2 \equiv N_{\text{ev}} _{\text{MB}} / N_{\text{ev}} _{(\text{MB} \& \text{Vtx})}$	$r_2/r_1 - 1 (\%)$
10d	1.093581	1.095088	1.4
11a	1.146103	1.151197	4

Table 7.2: Comparison between the ratio of the normalized p_T -distributions and the inverse ratio of the event numbers ($0.6 < |\eta| < 0.8$). The former is obtained by a fit of a constant to the ratio. Effect of the Vtx cut is shown.

MC	$\frac{1}{N_{\text{ev}}} \frac{dN}{dp_T}$ -ratio (MB & Vtx & Z_{vtx})/(MB & Vtx)	$N_{\text{ev}} _{(\text{MB} \& \text{Vtx})} / N_{\text{ev}} _{(\text{MB} \& \text{Vtx} \& Z_{\text{vtx}})}$
10d	1.000228	1.113619
11a	1.001680	1.063987

Table 7.3: Comparison between the ratio of the normalized p_T -distributions and the inverse ratio of the event numbers ($0.6 < |\eta| < 0.8$). The former is obtained by a fit of a constant to the ratio. Effect of the Z_{vtx} cut is shown.

In Pb–Pb collisions, $N_{\text{ev}}|_{\text{MB}} / N_{\text{ev}}|_{(\text{MB} \& \text{Vtx})} = 1$ and $N_{\text{ev}}|_{(\text{MB} \& \text{Vtx})} / N_{\text{ev}}|_{(\text{MB} \& \text{Vtx} \& Z_{\text{vtx}})} - 1 \sim 10^{-4}$ are observed in both data and MC. Therefore it can be concluded that there is no distortion effect in Pb–Pb collisions.

7.1.3 Contamination by secondary particles

The effect of the track cuts to reject secondary particles originating from weak decays and interaction with detector materials is studied using MC productions. The contamination is shown in Fig. 7.3. As can be seen, pions and kaons have secondary contamination below 1% for $p_T > 0.5$ GeV/ c . Protons and antiprotons have different non-negligible

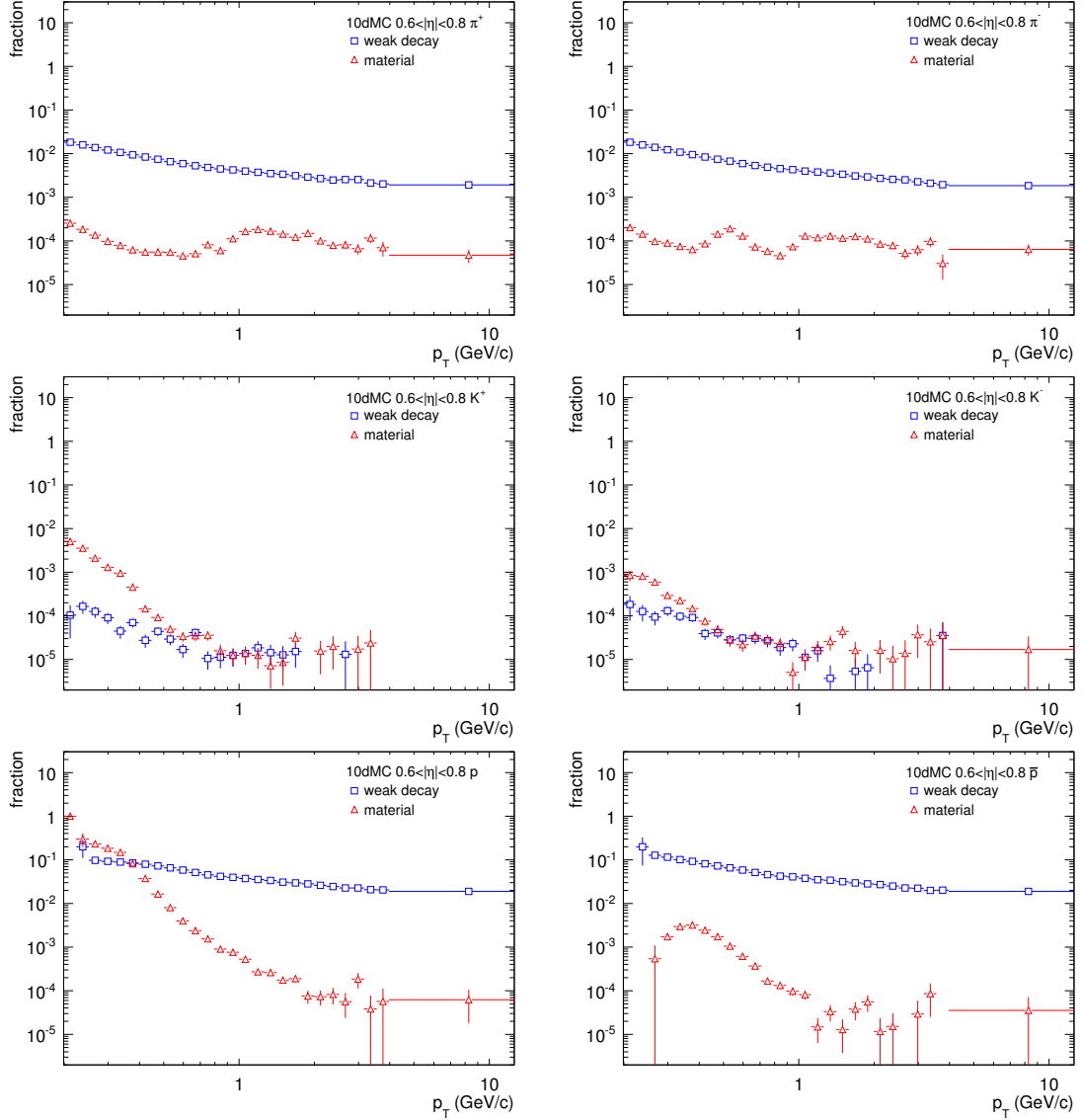


Figure 7.3: Comparison among contributions of secondary particles in the MC track sample selected by the track cuts.

contributions from material, especially at $p_T < 1 \text{ GeV}/c$. The contributions from weak decays are similar, both at a few per cent level. The difference in the contamination between positively and negatively charged secondary particles is due to a larger absorption of the latter in the material and to the isospin effects. As a side remark, the selected electrons turn out to be mostly originating from material and therefore are not further discussed, their presence in the fitting being only part of the machinery.

7.1.4 Tracking efficiency

The tracking efficiency for detector acceptance, track reconstruction and selection is estimated in MC for primary pions, kaons and protons in pseudo-rapidity η windows. It is defined as the ratio between the reconstructed p_T spectrum after the track cuts and the

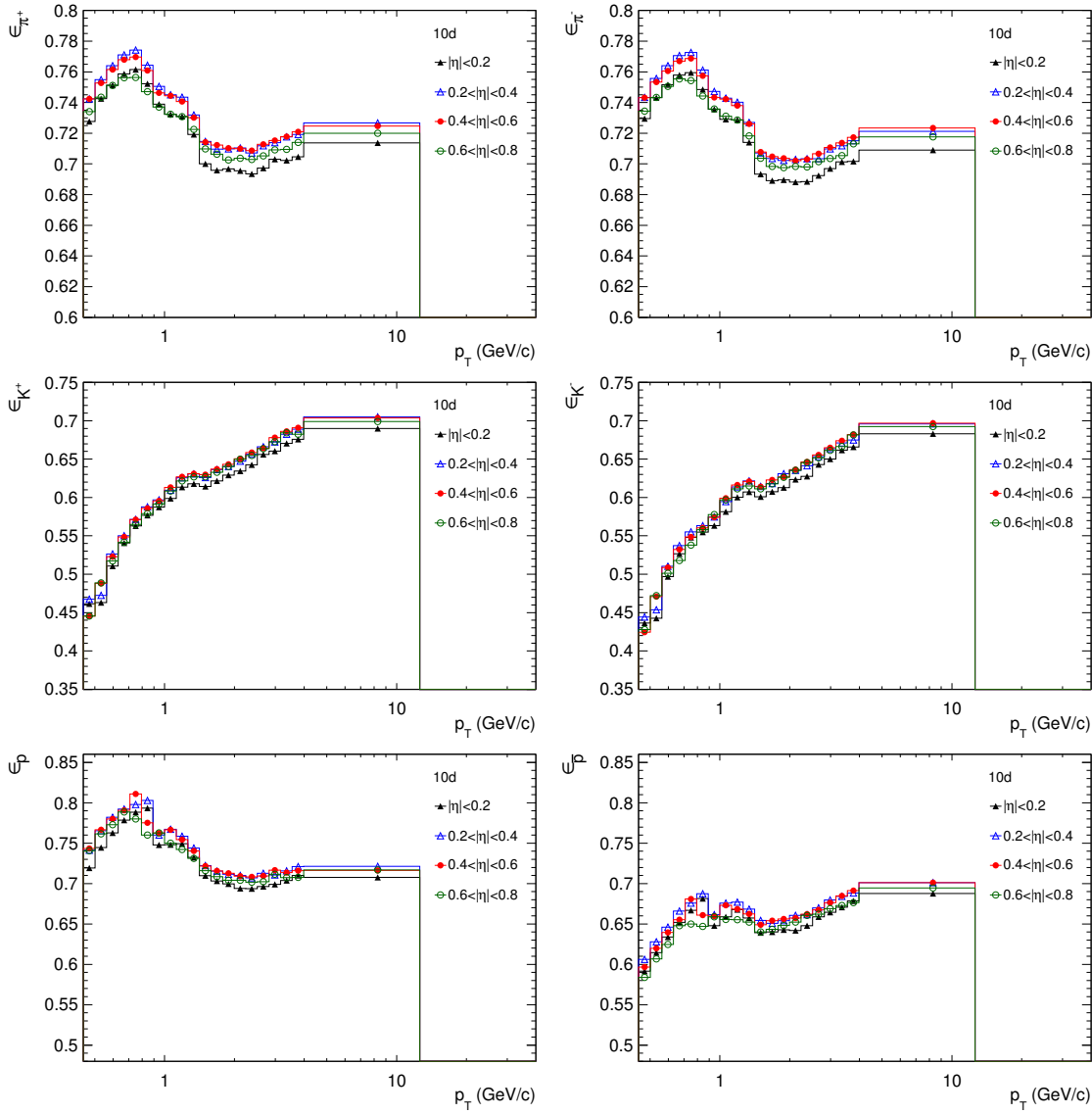


Figure 7.4: Tracking efficiencies estimated in MC (10d period, pp collisions at 7TeV) for positively charged particles (*left*) and negatively charged particles (*right*).

generated p_T -spectrum after the event cuts. As can be seen in Fig. 7.4, the efficiencies in different η -windows are consistent for $p_T > 0.5$ GeV/ c with maximum absolute difference 2–3%. The efficiencies from different data samples are also compared, the absolute sample dependent variation being about 7%. The common increasing trend of the efficiencies is a consequence of decreasing energy loss in the detector material and weaker bending in the magnetic field, while the slight decrease at $p_T \gtrsim 0.8$ GeV/ c is due to a larger fraction of undetected track segments when the part of the azimuthal projection of particle trajectories falling in the dead zones between the TPC readout sectors increases with p_T . As is the case for secondary contamination, the difference in efficiencies between positively and negatively charged particles is due to absorption in material and isospin effects. The efficiency deficit of the low momentum kaon is due to the fast decay. At high p_T the efficiency trends to be particle-type independent and is about 70%.

A study [Abb13] shows that the reaction cross sections for negative kaons and antiprotons

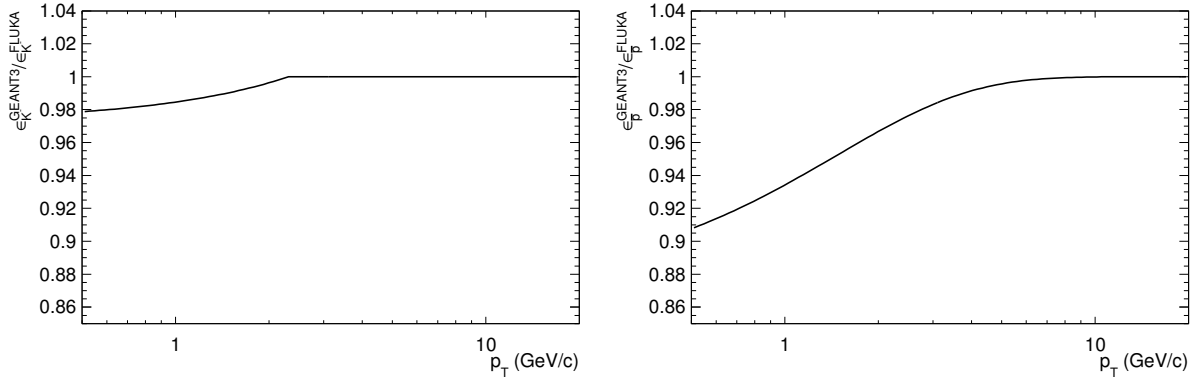


Figure 7.5: Ratios between the GEANT3 and FLUKA tracking efficiencies for negative kaons (*left*) and antiprotons (*right*).

in the detector material is overestimated in the transport model, GEANT3 [Bru94], of the MC simulations . Correspondingly the ratio between the tracking efficiencies estimated with GEANT3 and another transport model FLUKA [Fer05], which has been shown to be more accurate, is used as a correction. This ratio is parametrized [Abb13] (Fig. 7.5) by fitting to measurements:

$$R_k \equiv \frac{\epsilon_k^{\text{GEANT3}}(p_T)}{\epsilon_k^{\text{FLUKA}}(p_T)} = \begin{cases} \min \{0.97 + 0.012p_T, 1\}, & k = K^- \\ 1 - 0.13e^{-0.68p_T}, & k = \bar{p} \\ 1, & \text{otherwise} \end{cases}. \quad (7.1)$$

It can be seen that the correction for antiprotons is significant: about 10% at $p_T = 0.5 \text{ GeV}/c$ and decreasing to below 1% at $5 \text{ GeV}/c$.

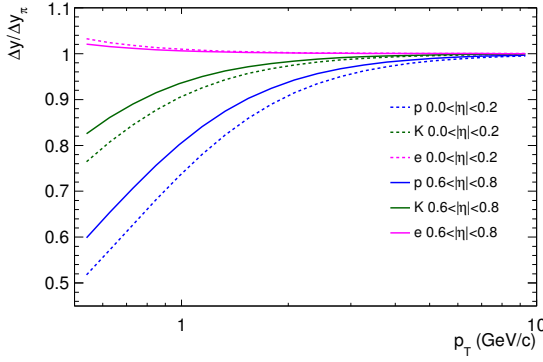
7.1.5 Calculation of p_{T} -spectra and yield ratios

The normalized p_{T} -spectra (for the normalization strategy, cf. [Aam11b]) is calculated for positively and negatively charged particles separately as follows:

$$\frac{1}{N_{\text{INEL}}} \frac{1}{2\pi p_{\text{T}}} \frac{d^2 N_k}{dy dp_{\text{T}}} = \frac{1}{N_{\text{ev}}|(\text{MB}\&\text{Vtx})}} \frac{N_{\text{ev}}|(\text{MB}\&\text{Vtx})}}{N_{\text{ev}}|\text{MB}} \epsilon_{\text{trig}} \times \frac{1}{2\pi p_{\text{T}}} \frac{\Delta N}{\Delta y_k \Delta p_{\text{T}}} A_k(p_{\text{T}}) f_{k,\text{prim}}(p_{\text{T}}) \frac{R_k(p_{\text{T}})}{\epsilon_k(p_{\text{T}})}, \quad (7.2)$$

where

- $N_{\text{ev}}|\text{MB}$, $N_{\text{ev}}|(\text{MB}\&\text{Vtx})$ and $N_{\text{ev}}|(\text{MB}\&\text{Vtx}\&Z_{\text{vtx}})$ are the numbers of events after the MB, Vtx and Z_{vtx} cuts (Section 7.1.2),
- ϵ_{trig} is the minimum bias trigger efficiency estimated by the collaboration as 0.883 and 0.852 for 2.76 and 7 TeV pp collisions, respectively ($\epsilon_{\text{trig}} = 1$ for Pb–Pb collisions),

Figure 7.6: Δy ratios in different η -windows.

- ΔN is the number of particles of all types in the p_T -range Δp_T and rapidity range Δy_k (Eq. 6.10) in the sample with a given charge,
- $A_k(p_T)$ is the particle fraction in the sample as a function of p_T for particle type- k (Chapter 6),
- $f_{k,\text{prim}}(p_T)$ is the primary particle fraction for type- k (Section 7.1.3),
- and $\epsilon_k(p_T)$ is the tracking efficiency with the correction R_k (Section 7.1.4).

The spectrum is η -independent (possible η -variation is included in the systematic error) and can be extracted in η -windows and then averaged in the same way as discussed in the last part of Sections 6.4. For η -windows of equal widths, Δy_k depends on the particle type (see Section 6.1.3). In an η -window, the statistical errors of ΔN , $A_k(p_T)$, $f_{k,\text{prim}}(p_T)$ and $\epsilon_k(p_T)$ are propagated to the spectrum assuming uncorrelated measurements. The systematic error of the fraction $A_k(p_T)$ is also propagated. Similar to the case for the particle fractions, in this case for the spectra the errors in individual η -windows are then propagated to the η -averaged one with an additional component from the η -variation of the spectra for the systematic error, which effectively contains systematic uncertainties from the particle number ΔN , the primary particle fraction $f_{k,\text{prim}}(p_T)$ and the tracking efficiency $\epsilon_k(p_T)$, all being evaluated independently in η -windows.

The (same charge) particle yield ratio is defined as the spectrum ratio relative to the pion of the same charge, which can be calculated from the particle fractions as

$$\left(\frac{1}{N_{\text{INEL}}} \frac{1}{2\pi p_T} \frac{d^2 N_i}{dy dp_T} \right) / \left(\frac{1}{N_{\text{INEL}}} \frac{1}{2\pi p_T} \frac{d^2 N_\pi}{dy dp_T} \right) = \frac{d^2 N_i}{dy dp_T} / \frac{d^2 N_\pi}{dy dp_T} \quad (7.3)$$

$$= \frac{\Delta y_\pi(p_T)}{\Delta y_i(p_T)} \frac{A_i(p_T)}{A_\pi(p_T)} \frac{f_{i,\text{prim}}(p_T)}{f_{\pi,\text{prim}}(p_T)} \frac{\epsilon_\pi(p_T)}{\epsilon_i(p_T)} R_i(p_T). \quad (7.4)$$

The yield ratio, like the spectra, is calculated in η -windows and then averaged. The covariance matrix between A_k 's is used when calculating the ratios $A_i(p_T)/A_\pi(p_T)$. The Δy ratios are shown in Fig. 7.6. Compared to the spectrum Eq. 7.4, it can be seen that the particle number of all types with the same charge ΔN and the normalization factor $\epsilon_{\text{trig}} N_{\text{ev}|(\text{MB}\&\text{Vtx}\&Z_{\text{vtx}})} / N_{\text{ev}|(\text{MB}\&\text{Vtx})} / N_{\text{ev}|\text{MB}}$ is canceled in the yield ratio, resulting in reduced systematic errors.

7.2 Results and discussions

A comparison of the p_{T} -spectra (Eq. 7.2) among different collision systems at different center of mass energies is shown in Fig. 7.7. The systematic uncertainty, whose dominant part is estimated by the η -variation, is about 5 – 10%. It is important to note that at low p_{T} the Δy ordering, as discussed for the uncorrected fractions in Section 6.4, is eliminated by the Δy normalization. It can be seen that for pp collisions, the spectra at $\sqrt{s} = 7$ TeV are higher than the 2.76 TeV spectra. The difference increases with p_{T} and is about 30% at 1 GeV/c, consistent with the results for unidentified particles [Abe13c]. The spectra from Pb–Pb collisions, which are all above the ones in pp collisions, increase as the collisions go more central, as is expected from the increase of the number of binary nucleon-nucleon collisions (Fig. 7.1).

A comparison of the pp spectra at 2.76 TeV to the low p_{T} [Bus13] ($p_{\text{T}} < 4$ GeV/c, extended to 6 GeV/c for protons) and high p_{T} [Chr13] ($p_{\text{T}} > 3$ GeV/c, extended to 2 GeV/c for pions) analyses is shown in Fig. 7.8. In the first case the PID is performed piecewise by different detectors (ITS, TPC, TOF and HMPID) whose application is limited by the diminishing separation power between particle species when approaching p_{T} about 4–5 GeV/c, while in the latter the incoherent TPC PID method, which relies on external PID information, only works on the relativistic rise of the specific energy loss ($p_{\text{T}} \gtrsim 3$ GeV/c). The results from different analyses are consistent.

A charge ratio is defined as the spectra ratio between the two charges of the same particle type i :

$$\begin{aligned} i^+/i^- &\equiv \left(\frac{1}{N_{\text{INEL}}} \frac{1}{2\pi p_{\text{T}}} \frac{d^2 N_{i^+}}{dy dp_{\text{T}}} \right) / \left(\frac{1}{N_{\text{INEL}}} \frac{1}{2\pi p_{\text{T}}} \frac{d^2 N_{i^-}}{dy dp_{\text{T}}} \right) \\ &= \frac{\Delta N^+}{\Delta N^-} \frac{A_{i^+}(p_{\text{T}})}{A_{i^-}(p_{\text{T}})} \frac{f_{i^+, \text{prim}}(p_{\text{T}})}{f_{i^-, \text{prim}}(p_{\text{T}})} \frac{\epsilon_{i^-}(p_{\text{T}})}{\epsilon_{i^+}(p_{\text{T}})} \frac{1}{R_{i^-}(p_{\text{T}})}. \end{aligned} \quad (7.5)$$

The superscripts \pm denote the particle charges for which the spectra are extracted separately. Compared to the (same charge) yield ratio, the systematic errors from ΔN^\pm both enter the charge ratio. The charge ratios are shown in Fig. 7.9. As can be seen, within errors the ratios are flat around unity as a function of p_{T} . The charge ratio p/\bar{p} is consistent with the dedicated high precision measurement in $0.45 \leq p_{\text{T}} (\text{GeV}/c) \leq 1.05$ [Abb13]. Because of their consistency, spectra and yield ratios from both charges are summed and averaged assuming uncorrelated errors, respectively, for further discussions.

The low p_{T} parts of the π , K, and p spectra are simultaneously fit to a blast-wave function [Sch93], which models the fireball expansion with a transverse velocity profile

$$\beta_{\text{T}}(r) = \left(\frac{r}{R} \right)^n \beta_{\text{T}}(R), \quad (7.6)$$

where $r \leq R$ is the radial position in the fireball. When $n = 1$, the expansion is Hubble-like. In this parametrization, besides the individual normalization of the spectra there are further three parameters: the kinetic freezeout temperature T_{kin} , the average transverse velocity $\langle \beta_{\text{T}} \rangle$ and the velocity profile exponent n . Because the particles with higher p_{T} decouple from the collective motion progressively, the upper bounds of the p_{T} ranges have systematic influence on the fit. Here the p_{T} ranges are from 0.6 GeV/c, which is the common lower cut-off in this analysis, to the standard upper bounds used in [Abe13a]: 1, 1.5

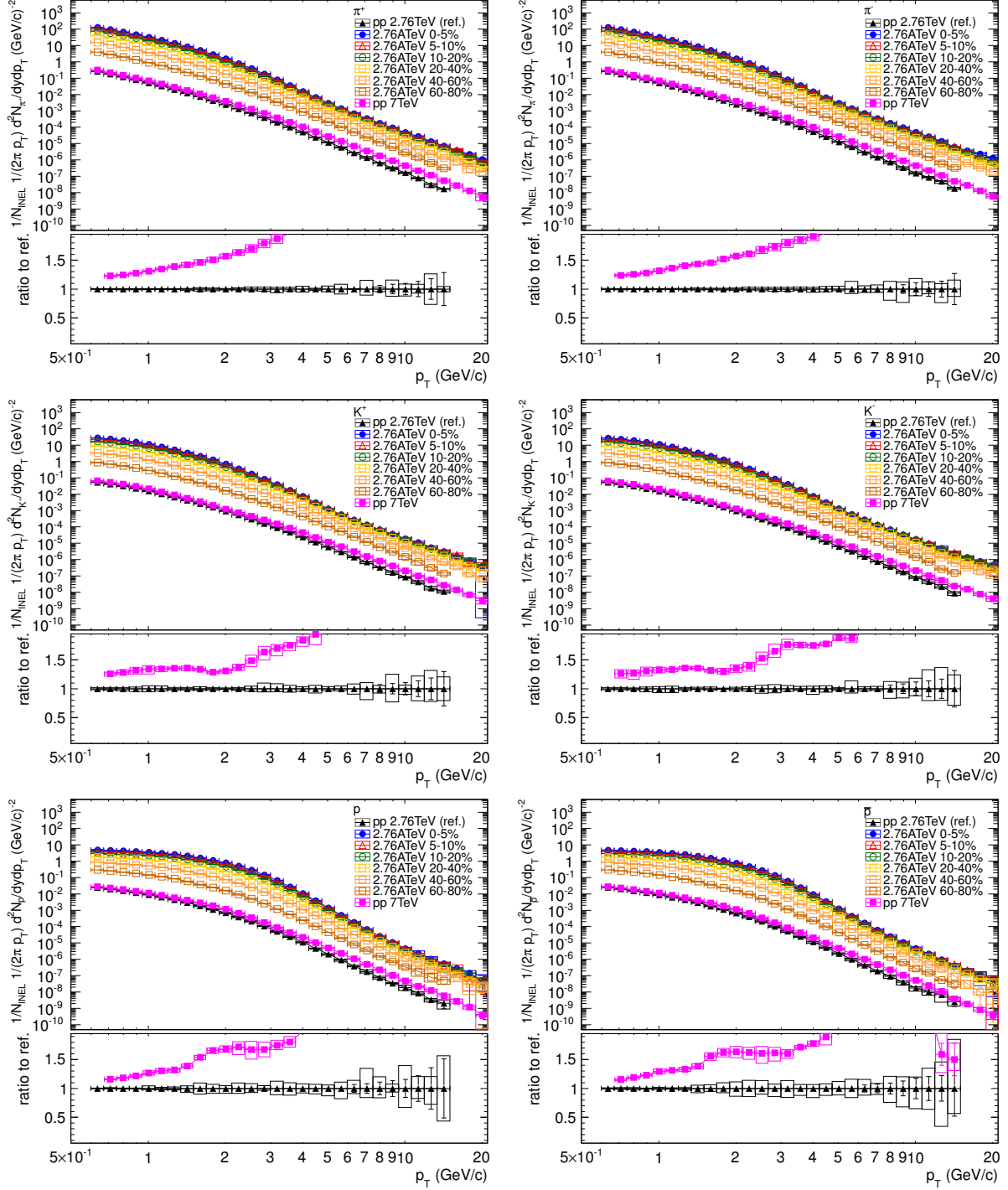


Figure 7.7: Comparison of the p_T -spectra in different collision systems with different center of mass energies.

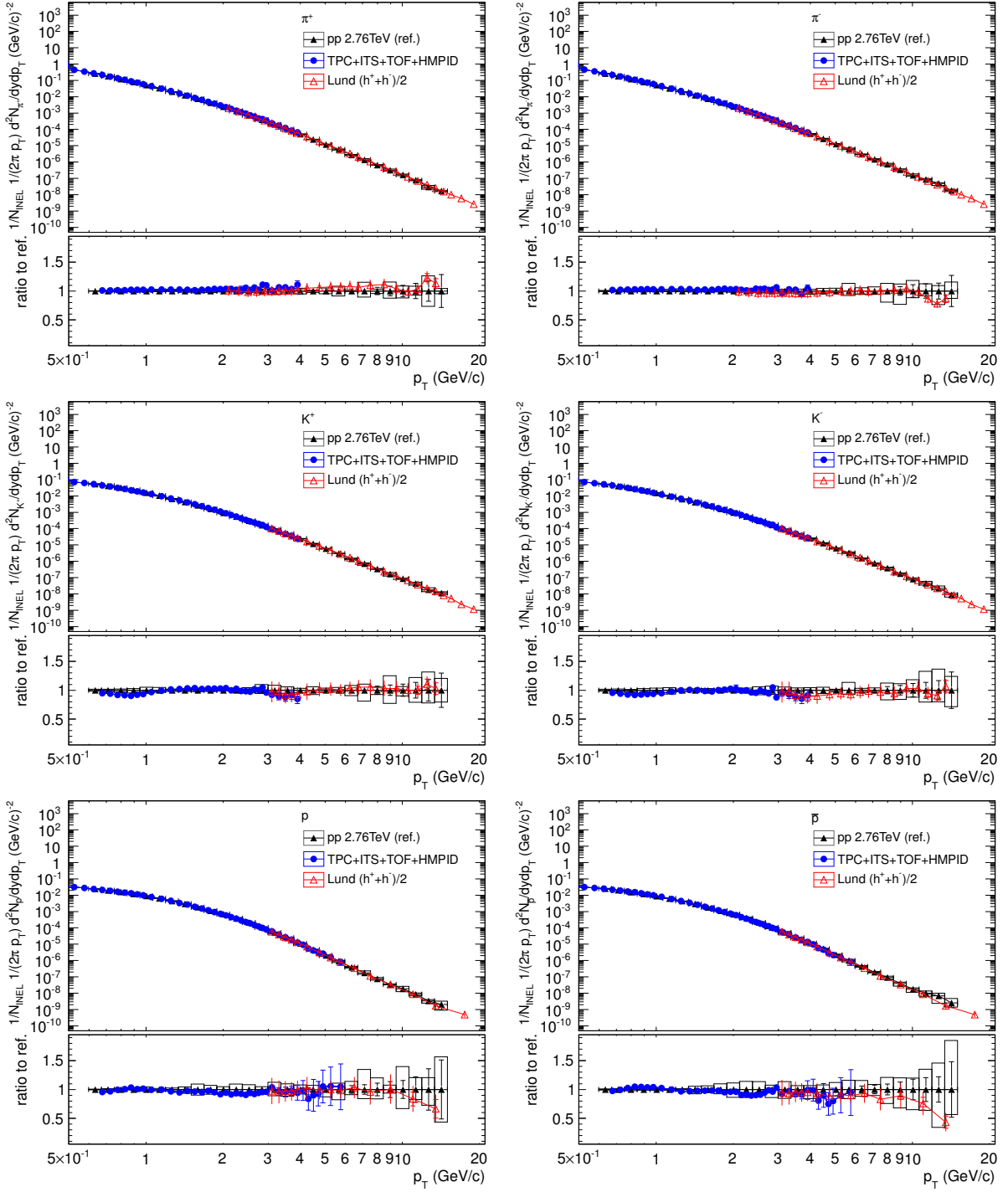


Figure 7.8: Comparison of the p_T -spectra in pp collisions at $\sqrt{s} = 2.76$ TeV to the low p_T [Bus13] (TPC+ITS+TOF+HMPID) and high p_T [Chr13] (Lund) analyses. The high p_T spectra are the averages between the positive and negative particles.

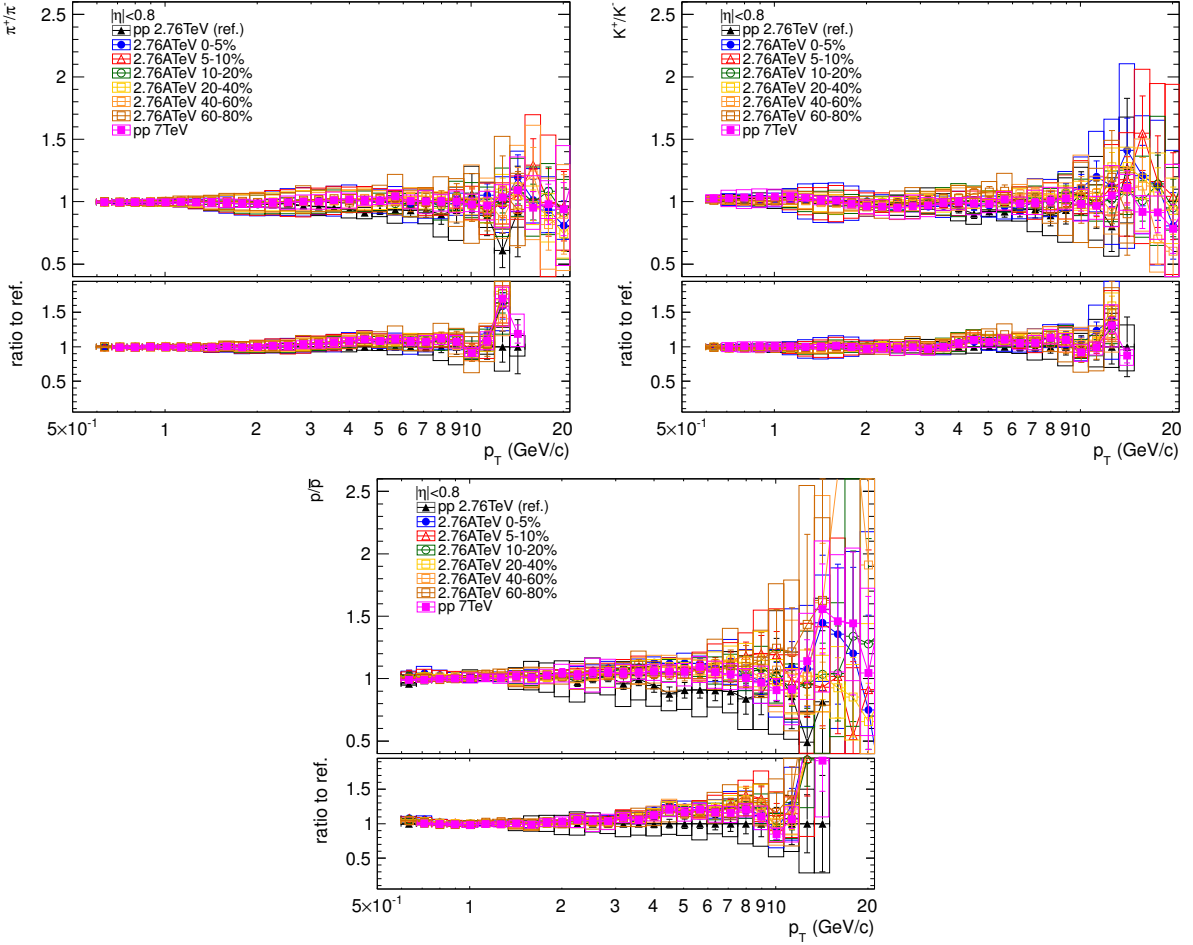


Figure 7.9: Charge ratios for pions, kaons and protons.

and 3 GeV/ c for π , K, and p, respectively. Another source of fit instability is the species dependence of T_{kin} which is not considered in the model. Different combinations of the particle species in the fit systematically vary the results. A simultaneous fit to all three species is adopted here following the standard procedure. As is discussed in [Abe13a], variations with respect to the standard setup should be considered sources of systematic errors of the fit.

The blast-wave fit with the standard setting discussed above is applied to the spectra from Pb–Pb collisions, and also to pp collisions for a comparison. The fit results are summarized in Tab. 7.4. The reduced χ^2 shows that the fit quality in general is good. The ratios between the spectra and the blast-wave fits are shown in Fig. 7.10. Above the p_{T} upper bound of each species the fit under-estimates the spectra with larger deviation at higher p_{T} . Figure 7.11 shows the $1-\sigma$ contours for the correlation between T_{kin} and $\langle \beta_{\text{T}} \rangle$, the sizes of which represent the measurement uncertainties of the spectra. The Pb–Pb results are consistent with the ones in [Abe13a] which have different p_{T} lower bounds: 0.5, 0.2 and 0.3 GeV/ c for π , K, and p, respectively. As the collisions become more central, $\langle \beta_{\text{T}} \rangle$ increases, and n and T_{kin} decrease. It is interesting to note that for pp and Pb–Pb collisions, the correlation between T_{kin} and $\langle \beta_{\text{T}} \rangle$ lies on the same trend, and that all three parameters, T_{kin} , $\langle \beta_{\text{T}} \rangle$ and n , follow the same ordering as for the p_{T} spectra in Fig. 7.7, all suggesting pp collisions at higher energy resemble Pb–Pb collisions to a larger extent.

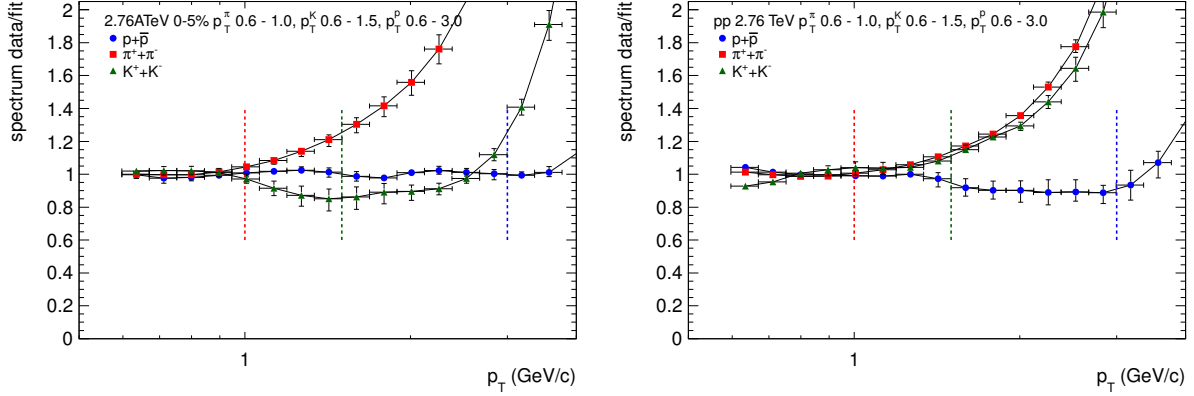


Figure 7.10: Ratios between the measured spectra and the simultaneous blast-wave fit to π , K and p up to p_T 1, 1.5 and 3 GeV/c , respectively. Results for (*left*) most central Pb–Pb collisions and (*right*) pp collisions at 2.76 TeV are shown. The vertical dashed lines indicate the upper p_T bounds in the fit.

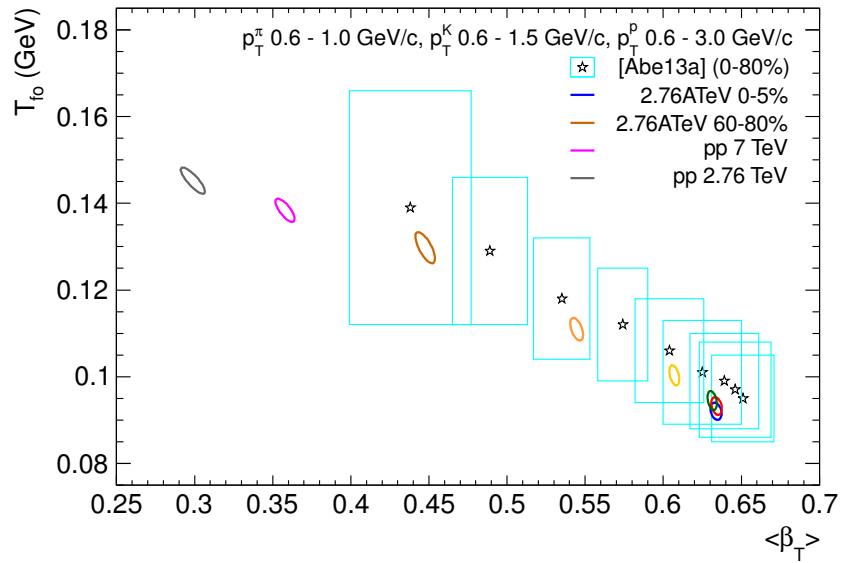


Figure 7.11: The 1- σ contour of the extracted T_{kin} and $\langle \beta_T \rangle$. Results from [Abe13a] are also shown with error boxes representing the full systematic errors including fit instability (obtained by varying the setting – see text for details – with respect to the standard one). For Pb–Pb collisions, $\langle \beta_T \rangle$ increases as the collisions become more central.

data	Pb–Pb 2.76 ATeV						pp	
	0–5%	5–10%	10–20%	20–40%	40–60%	60–80%	7 TeV	2.76 TeV
$T_{\text{kin}}/\text{MeV}$	92	93	94	100	111	130	138	145
$\sigma_{T_{\text{kin}}}/\text{MeV}$	2	2	2	2	3	4	3	3
$\langle \beta_T \rangle$	0.634	0.634	0.631	0.607	0.545	0.448	0.358	0.299
$\sigma_{\langle \beta_T \rangle}$	0.004	0.003	0.003	0.003	0.004	0.006	0.006	0.008
n	0.79	0.78	0.78	0.85	1.10	1.61	2.60	3.4
σ_n	0.02	0.02	0.02	0.02	0.03	0.05	0.09	0.2
χ^2/n_{DOF}	1.3	1.6	1.5	1.6	2.4	1.3	1.7	5.2

Table 7.4: Extracted T_{kin} , $\langle \beta_T \rangle$ and n from the blast-wave fit to the spectra from Pb–Pb and pp collisions. The reduced χ^2 is also shown.

The comparison of the yield ratios (Eq. 7.4) among collision systems and energies is shown in Figs. 7.12 and 7.13. Within errors the Pb–Pb results are consistent with [Abe13a] which covers the low p_T regions, 0.3–3 and 0.2–3 GeV/ c , for p/ π and K/ π , respectively. In contrast to the p_T -spectra and the blast-wave parameters, the yield ratios from pp collisions at different energies are consistent within errors. The baryon anomaly at p_T between 2–8 GeV/ c , characterized by a larger enhancement at more central collisions, is clearly seen in Fig. 7.12. The enhancement in the most central case is about a factor of three. On the other hand at $p_T < 1.5$ GeV/ c the p/ π ratio evolves with centralities in a reverse order with a maximum reduction of 2.5 at 0.6 GeV/ c . The different ordering implies that protons at low p_T are shifted to higher p_T and the effect is most prominent for central collisions. This is qualitatively expected from the collective flow effect where the particle p_T is blue-shifted proportionally to the mass. It is interesting to note that another reverse ordering seems to appear at $p_T > 10$ GeV/ c but the significance is limited by both the statistical and systematic uncertainties. This relates to the questions whether the p/ π ratio is suppressed in Pb–Pb collisions at high p_T and whether or how the baryon anomaly extends to the high p_T limit where hard partonic interactions dominate. As will be discussed, the ratio of yield ratios between Pb–Pb and pp collisions is the ratio of nuclear modification between particle species.

The K/ π ratio shown in Fig. 7.13 is in contrast more similar among collision systems and energies than the case for proton. There is a slight centrality ordering at p_T 1 – 2 GeV/ c . But the magnitude of enhancement is so small, maximum about 20%, that the significance is rather limited. At lower p_T there is no reverse ordering – though the possibility that the reverse ordering happens at $p_T < 0.6$ GeV/ c cannot be ruled out in this analysis.

As is already seen in Fig. 7.7, the p_T spectrum from Pb–Pb collisions increases with the number of binary nucleon-nucleon collisions. A detailed comparison to the spectrum from pp collisions at the same energy per nucleon scaled by the number of binary collisions describes how the particle production is modified in the medium produced in the Pb–Pb collisions. The so-called nuclear modification factor for particle- k is defined as

$$R_{\text{AA}}^k \equiv \frac{d^2 N_k^{\text{AA}} / dy dp_T}{\langle N_{\text{coll}} \rangle d^2 N_k^{\text{pp}} / dy dp_T}, \quad (7.7)$$

with the spectra $d^2 N_k^{\text{AA, pp}} / dy dp_T$ for nuclear and pp collisions, respectively, defined in their full forms in Eq. 7.2, and $\langle N_{\text{coll}} \rangle$ shown in Fig. 7.1. At high p_T , $R_{\text{AA}} < 1$ means

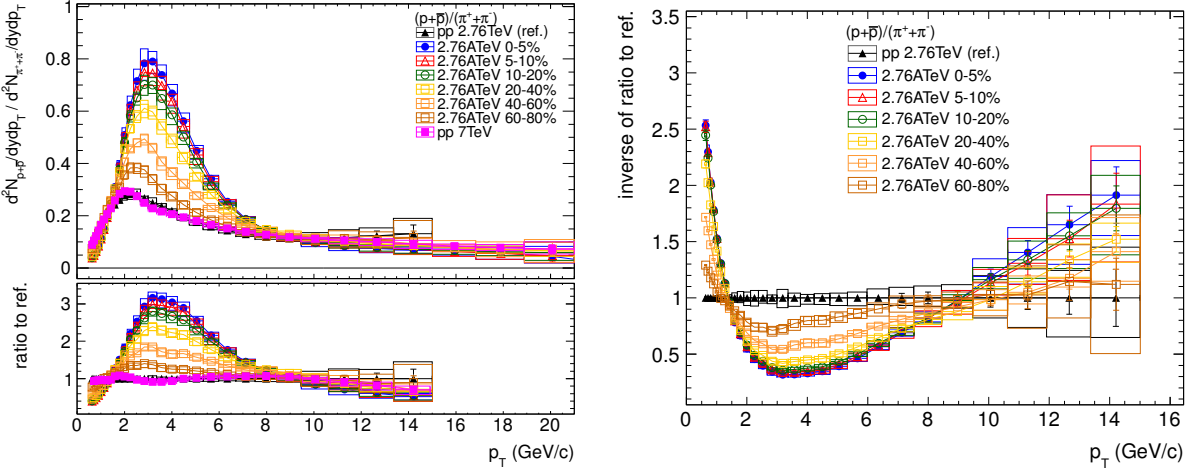


Figure 7.12: Comparison of $(p^+ + p^-)/(\pi^+ + \pi^-)$ in different collision systems with different center of mass energies. In the *right* panel the inverse of the ratio to the reference data is shown with focus on pp and Pb–Pb collisions at the same energy.

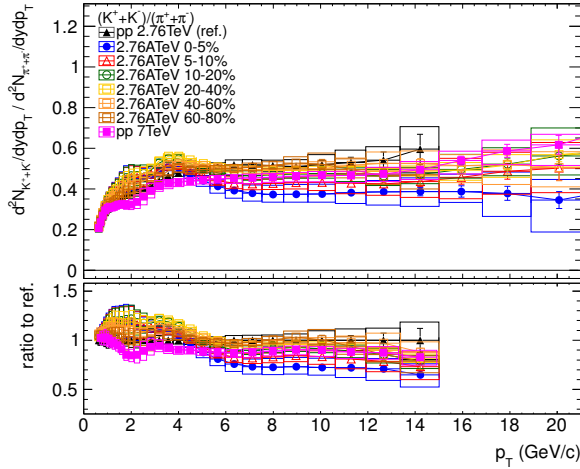


Figure 7.13: Comparison of $(K^+ + K^-)/(\pi^+ + \pi^-)$ in different collision systems with different center of mass energies.

that the production is suppressed in Pb–Pb collisions compared to an independent superposition of nucleon-nucleon binary collisions. The results are shown in Figure 7.14. The common centrality ordering for all three particle species indicates that the modification in general increases as the collisions become more central. For pions and kaons the modification reaches a local maximum at p_T around 6–7 GeV/ c and is lessened as p_T increases. This is consistent with the results for unidentified charged particles (see Fig. 1.8) [Aam11a, Abe13d] where the statistics is dominated by pions. The proton R_{AA} , on the other hand, does not exhibit any similar modification maximum up to the high p_T limit of this analysis, which is 15 GeV/ c imposed by the statistics of pp collisions at 2.76 TeV. The origin of this difference can be understood with the following observation. In fact the ratios between R_{AA} of different particle species have already been shown in the “ratio to ref.” lower panels in Figs. 7.12 and 7.13. This is illustrated as the

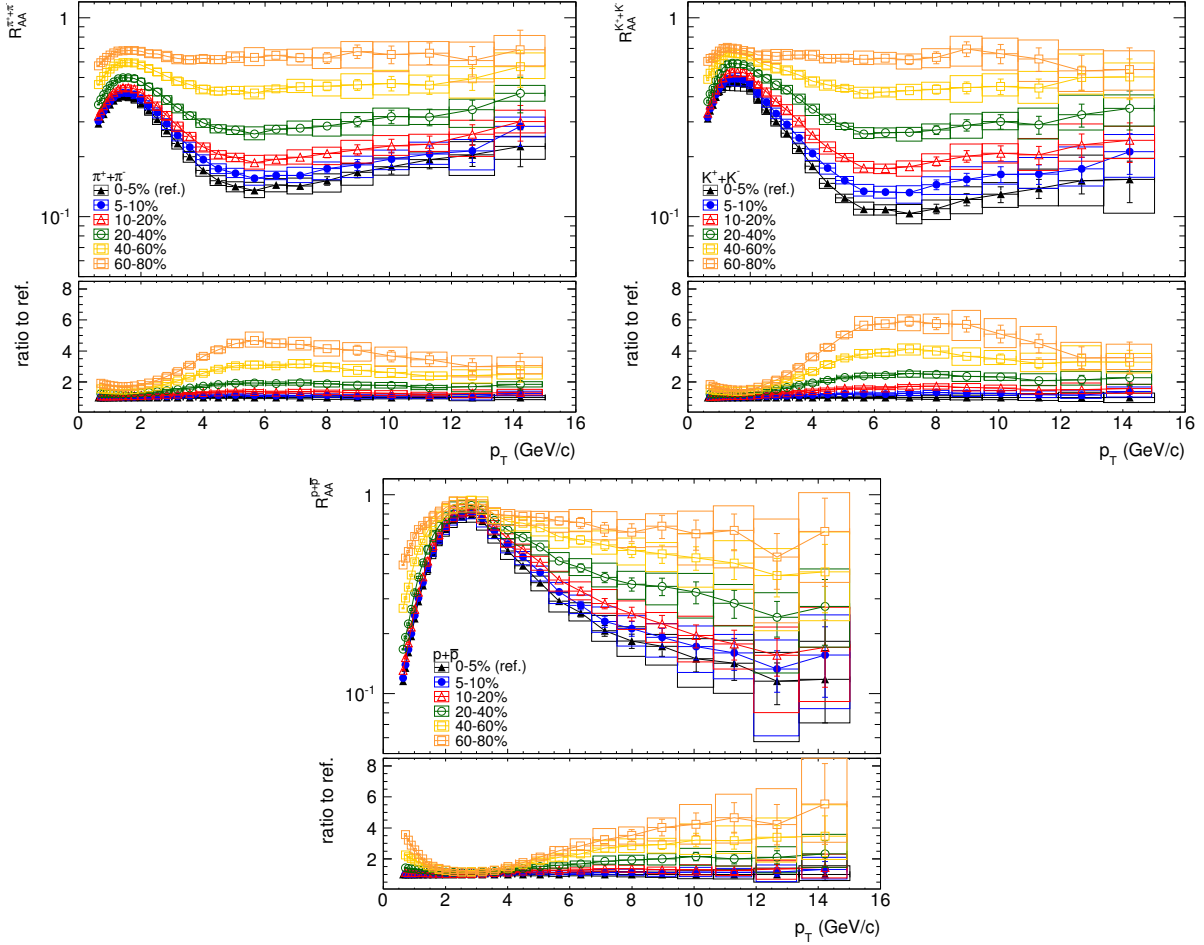


Figure 7.14: Nuclear modification factors for pions, kaons and protons.

following. The R_{AA} ratio of kaons or protons to pions for the same centrality is, according to Eq. 7.7,

$$\begin{aligned} \frac{R_{AA}^{K,p}}{R_{AA}^\pi} &= \left(\frac{d^2N_{K,p}^{AA}/dydp_T}{\langle N_{coll} \rangle d^2N_{K,p}^{pp}/dydp_T} \right) / \left(\frac{d^2N_\pi^{AA}/dydp_T}{\langle N_{coll} \rangle d^2N_\pi^{pp}/dydp_T} \right) \\ &= \left(\frac{d^2N_{K,p}^{AA}/dydp_T}{d^2N_\pi^{AA}/dydp_T} \right) / \left(\frac{d^2N_{K,p}^{pp}/dydp_T}{d^2N_\pi^{pp}/dydp_T} \right), \end{aligned} \quad (7.8)$$

where both the numerator and the denominator are the yield ratios defined by Eq. 7.3. As the pp collisions at 2.76 TeV are chosen as the reference data in Figs. 7.12 and 7.13, the ratio of the yield ratios between the Pb–Pb collisions and this reference data is the R_{AA} ratio between particle species. In other words, the observed proton R_{AA} is a product of the pion R_{AA} and the ratio of p/π with respect to the pp collisions, namely the local maximum of the nuclear modification for pions and the baryon anomaly cancel each other, leading to a monotonic increase of modification for protons at $p_T > 3 \text{ GeV}/c$. As the ratio of p/π with respect to the pp collisions tentatively suggests a suppression of p/π at high p_T in Pb–Pb collisions, it remains unclear whether the nuclear modification for the protons will continue to increase or at some point reach a local maximum, as for the pions and

kaons. In either case, at high p_{T} a suppressed yield ratio p/π in Pb–Pb collisions, or correspondingly a difference in R_{AA} for protons and pions, means that the hadrochemical composition from parton fragmentation is modified in Pb–Pb collisions.

7.3 Outlook – identified jet fragmentation

As an extension of the discussion, the TPC coherent fit is applied (without TOF identification) to the sample of primary particles in jets (see analysis details in [Aam13]) and the fractions of pions, kaons, and protons with p_{T} up to 30 GeV/c are extracted. Figure 7.15 shows the uncorrected particle fractions extracted from charged leading jets of p_{T} 10–80 GeV/c in pp collisions at $\sqrt{s} = 7$ TeV. Since at high p_{T} the tracking efficiencies tend to be independent of particle species (see Section 7.1.4), the results indicate that the proton yield in jets is smaller than the pion or kaon yields. The results are compared to MC simulations [Aam13] with Perugia-0 tune [Ska10] of PYTHIA6 [Sjo06] after the ALICE reconstruction. It can be seen that the simulation describes the data well. The particle fractions in jets are further compared to the particle fractions from the inclusive primary particle sample obtained by the same event and track selections but without jet reconstruction. The two sets of fractions are similar at $p_{\text{T}} \gtrsim 10$ GeV/c while at lower p_{T} the difference is large. Studies of identified particle production in jets from Pb–Pb collisions will provide further information of the fragmentation mechanism and the properties of the hot dense QCD medium created at the LHC.

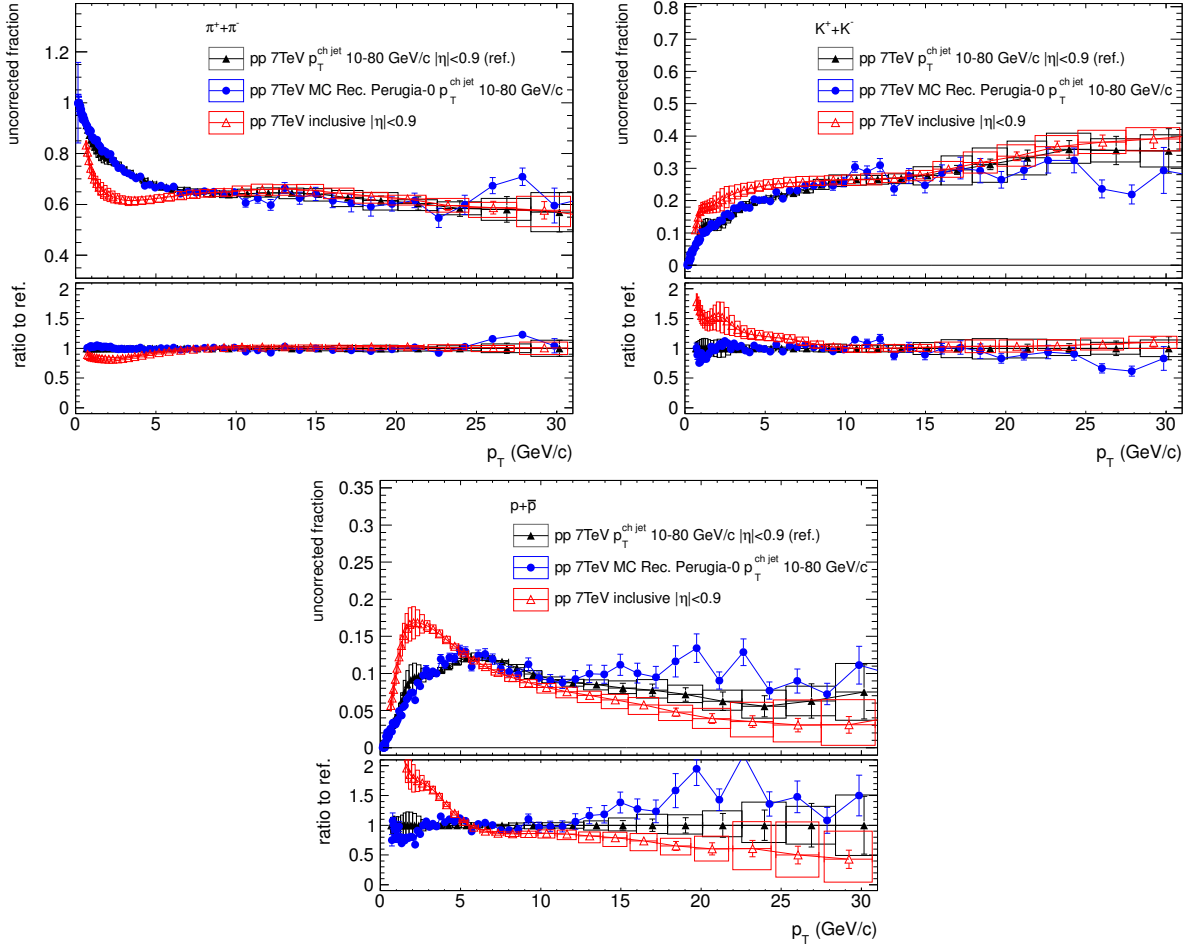


Figure 7.15: Uncorrected particle fractions (normalized to the total amount of primary pions, kaons and protons) extracted from charged leading jets of p_T 10–80 GeV/c in pp collisions at $\sqrt{s} = 7$ TeV by the TPC coherent fit without TOF pre-identification. The results are compared to MC simulations (see text for details). Also shown are the uncorrected particle fractions from the inclusive primary particle sample obtained by the same event and track selections but without jet reconstruction.

Chapter 8

Summary and conclusion

The newly developed TPC combined cosmic track fit (Chapter 2) greatly improves the momentum measurement for cosmic rays. It also provides a reference measurement for the standard TPC tracking.

A general statistical description of the TRD signal (Chapter 3) is developed. It is applicable for different signal compositions: collisional ionization with or without transition radiation. Together with the cosmic track fit, a novel measurement of the transition radiation induced by cosmic muons is performed (Chapter 4). The kinematic dependence of the transition radiation production is measured in the $\beta\gamma$ region from 1 to 10^4 , representing the state of the art for the community.

The knowledge of the cosmic track fit and the statistical description of the TRD signal is further applied to the investigation of the TRD truncated mean signal (Chapter 5). Systematic studies including calibration and various optimizations have been performed. With this method, the TRD is able to provide robust identification for electrons, hadrons and also light nuclei.

The TPC coherent fit (Chapter 6) is a novel particle identification method on a statistical basis involving high dimensional minimization and regularization. The method has been developed as a general framework aiming at simplicity, self-consistency and robustness. No fine tuning or external information is employed (though can be applied for second order accuracy¹). As is shown in its application in the study of identified particle production (Chapter 7), a good agreement with other analyses has already been achieved. Both the low p_T and high p_T analyses have conceptual limitations in the methods and are therefore confined to dedicated p_T regions. An advantage of the TPC coherent fit is its compatibility between different p_T regions. In principle this method can be useful to any analysis where statistical particle identification is needed. An example of a further application is the extraction of the pion, kaon, and proton fractions in jets (Section 7.3).

The (inclusive) production of pions, kaons, and protons is studied in p_T range from 0.6 GeV/c to about 20 GeV/c for different collision systems at different energies with the TPC coherent fit (Chapter 7). The baryon anomaly at $2 < p_T < 8$ GeV/c and the nuclear modification up to high p_T (> 10 GeV/c) in Pb–Pb collisions are observed.

¹External PID information has to be used with caution due to different detector acceptance, as should have been more emphasized in existing analyses.

The identified particle production is also studied in jets from pp collisions (Section 7.3). Compared to the inclusive production, a large difference is seen at $p_T \lesssim 10$ GeV/c. The jet fragmentation is further compared to Monte Carlo simulations and it is shown that the Perugia-0 tune of PYTHIA6 describes the data very well.

Appendix A

Exclusive central production of $\pi^+\pi^-$

In the early LHC period for proton-proton collisions where the pile-up could be ignored the following interaction was investigated in this work:

$$p + p \rightarrow p + p + X, \quad (\text{A.1})$$

where the protons only transfer a small amount of their momenta and X subsequently decays to two charged pions. Due to quantum number conservation, X is expected to have the vacuum quantum number. Candidates are the f_J and χ_{cJ} families with $J^{PC}=J^{++}$.

The measurement is based on 3.5×10^8 minimum biased events of proton-proton collisions at $\sqrt{s} = 7$ TeV. Because the out-going protons remain in the beam pipe, only indirect exclusivity can be ensured: events with exactly two unlike-sign tracks in the pseudo-rapidity range $|\eta| < 0.9$ are selected, requiring no signal in other detectors in $|\eta| > 0.9$. In total the ALICE detector can provide gaps (veto regions) in η about 7 units ($-3.7 < \eta < -0.9$ and $0.9 < \eta < 5.1$). With more veto detectors, the number of selected events decreases while the exclusivity is enhanced (see Table A.1). The event candidates are further selected if both tracks are identified as pions by TPC and TOF.

Veto detectors	V0	V0-FMD	V0-FMD-SPD	V0-FMD-SPD-TPC
veto regions in η	-3.7 – -1.7 2.8 – 5.1	-3.7 – -1.7 1.7 – 5.1	-3.7 – -0.9 0.9 – 5.1	-3.7 – -0.9 0.9 – 5.1
#exclusive two-track events $\times 10^4$	4.5	3.0	1.0	0.62
#minimum bias events				
#two-track events with unlike signs	3.0	3.9	8.7	14
#two-track events with like signs				

Table A.1: Number of selected events and exclusivity measured by the unlike-sign to like-sign ratio for different veto conditions.

The reconstructed $\pi^+\pi^-$ invariant mass distribution is shown in Figs. A.1. For comparison, the distribution from like-sign pairs is also shown as an indication for the contribution from non-exclusive background. Compared to the case with the veto detectors V0 alone, the like-sign background is much reduced by the veto detectors V0-FMD-SPD-TPC. In both cases, $f_0(980)$ and $f_2(1270)$ are clearly seen.

It is interesting to compare the like-sign subtracted distribution to the non-exclusive one (Fig. A.2). A large enhancement is seen for $f_0(980)$ and $f_2(1270)$ in exclusive events,

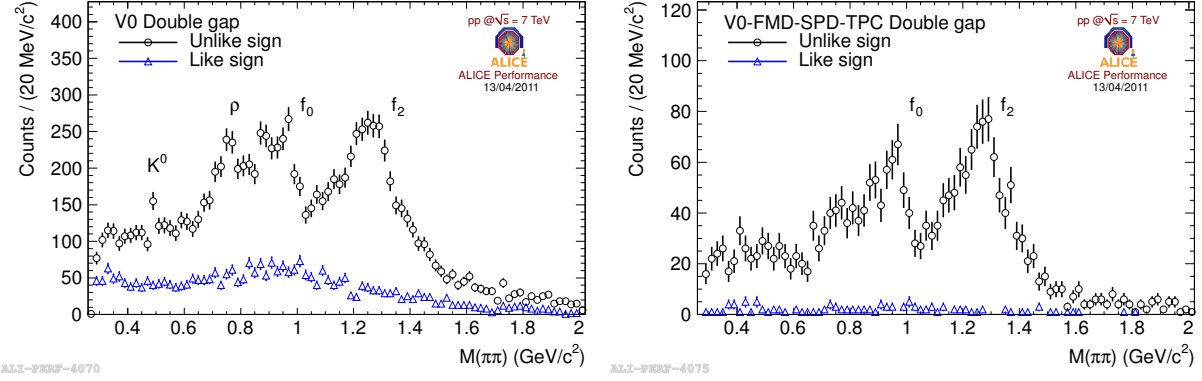


Figure A.1: Invariant mass distribution of exclusive two-pion events with veto detectors V0 (*left*) and V0-FMD-SPD-TPC (*right*). Events with like-sign tracks are compared.

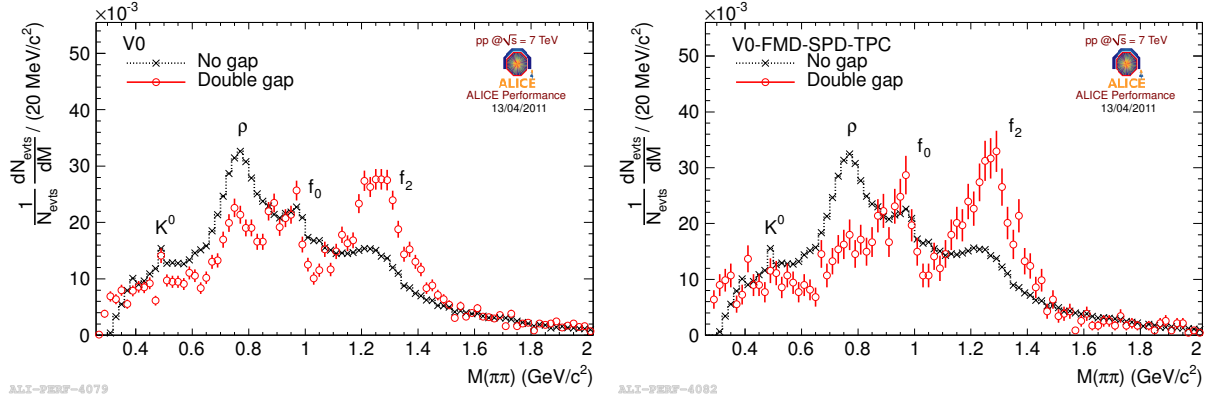


Figure A.2: Like-sign subtracted invariant mass distribution (events with double gaps) with veto detectors V0 (*left*) and V0-FMD-SPD-TPC (*right*). Non-exclusive events (no gap) are compared.

consistent with the expectation according to the quantum number conservation argument. It is also interesting to note that, the f_0 and f_2 signals are still very strong even though with V0 alone the exclusivity condition is less stringent which is indicated by the more prominent K_s^0 and $\rho(770)$ in the exclusive distribution.

The production of $f_0(980)$ and $f_2(1270)$ under investigation is typically non-perturbative. Higher states like the χ_c family which would render a quantitative comparison to theories is beyond the current statistical reach. The non-exclusive background can only be removed to a negligible level by measuring the out-going protons which is not available at the time of writing. Future potential experimental improvement may find its difficulty for this measurement due to the large pile-up foreseen in future LHC proton-proton collisions.

Appendix B

Track cuts for the particle production analysis

In order to select primary particles and ensure tracking qualities, the following track cuts are applied.

```
1 AliESDtrackCuts *raaCut = AliESDtrackCuts::  
2     GetStandardITSTPCTrackCuts2010(kTRUE,1);  
3     raaCut->SetMinNCrossedRowsTPC(120);  
4     raaCut->SetMinRatioCrossedRowsOverFindableClustersTPC(0.8);  
5     raaCut->SetMaxChi2PerClusterITS(36);  
6     raaCut->SetMaxFractionSharedTPCClusters(0.4);  
7     raaCut->SetMaxChi2TPCConstrainedGlobal(36);  
8     raaCut->SetEtaRange(-0.9,0.9);  
9     raaCut->SetPtRange(0.15, 1e10);
```

For the TPC coherent fit, a cut is applied to ensure the TPC signal quality.

```
1 trackptr->GetTPCsignalN() >60.
```

The following pseudo-codes are used for TOF identification for pions, kaons and protons,

```
1 if( TOF_status == AliPIDResponse::kDetPidOk ){  
2     n_sigma_pion      = PIDResponse->NumberOfSigmasTOF( track , AliPID::  
3                 kPion);  
4     n_sigma_kaon      = PIDResponse->NumberOfSigmasTOF( track , AliPID::  
5                 kKaon);  
6     n_sigma_proton    = PIDResponse->NumberOfSigmasTOF( track , AliPID::  
7                 kProton);  
8 }  
9 //inclusion_cut = 1 or 2, exclusion_cut = 4  
10 if( abs(n_sigma_pion) <inclusion_cut && abs(n_sigma_kaon)>  
11     exclusion_cut \\  
12     && abs(n_sigma_proton)> exclusion_cut ) is_pion = true;  
13     if( abs(n_sigma_kaon) <inclusion_cut && abs(n_sigma_pion)>  
14         exclusion_cut \\  
15     && abs(n_sigma_proton)> exclusion_cut ) is_kaon = true;  
16     if( abs(n_sigma_proton)<inclusion_cut && abs(n_sigma_kaon)>  
17         exclusion_cut \\
```

```
12 && abs(n_sigma_pion) > exclusion_cut) is_proton = true;
```

where the cut on the TOF status additionally requires no mismatch with the TPC identification.

List of Figures

1.1	Running coupling in a pure SU(3) gauge (i.e. no quark degree of freedom) theory at finite temperature (colored curves). Figure from [Brau07].	2
1.2	A schematic QCD phase diagram. Figure from [Alf08].	3
1.3	The hadronic mass spectrum from [Hag65]. For an update, cf. [Bro04]. . .	4
1.4	Pseudo-critical temperature T_{pc} for QCD transition(s) determined by recent lattice QCD calculations. Figure from [Fuk11], for details cf. references therein.	5
1.5	Lattice results on the temperature dependence of the energy density ϵ . Figure from [Bor10b]. The Stefan-Boltzmann limit of an ideal gas of quarks and gluons is indicated by an arrow. See also [Baz10].	6
1.6	Relative particle abundances measured at RHIC at $\sqrt{s_{NN}} = 130$ and 200 GeV compared to thermal model calculations. Figure from [Bra03].	7
1.7	p/π and \bar{p}/π ratios for Au–Au collisions at $\sqrt{s_{NN}} = 200$ GeV at RHIC. Figure from [Adl03].	8
1.8	Nuclear modification factor R_{AA} in central Pb–Pb collisions at $\sqrt{s_{NN}} = 2.76$ TeV at the LHC compared to measurements at $\sqrt{s_{NN}} = 200$ GeV at RHIC. Figure from [Aam11a].	8
1.9	The ALICE detector in 3D view. The inset shows the ITS.	9
1.10	3D view of the TPC field cage. Figure from [Alm10].	10
1.11	The layout of the TRD. Figure from [And12].	11
1.12	Cross-sectional view of a TRD module in (a) rz -plane and (b) $r\phi$ -plane. Figures from [And12].	12
1.13	The particle velocity β (in unit of the speed of light) measured by TOF as a function of the momentum.	12
1.14	Connections between chapters. Black arrows indicate direct dependency in terms of machinery. Red dashed arrows represent logical connections following which the techniques involved can be understood in a general framework based on the fact that the qualitative properties of the TPC signal is the same as for the TRD without transition radiation.	13

LIST OF FIGURES

2.1	Correlation between p_T measured by even- and odd-pads separately. For each x-slice the distribution is normalized to unity so that the interpretation of the z-coordinate is the conditional probability of a p_T from even-pads given a p_T from odd-pads. The <i>left</i> panel is using the standard track fit on cosmic tracks of half length, while the <i>right</i> one is using the combined track fit on cosmic tracks of full length.	18
2.2	RMS of different correlations: even-odd, standard-combined.	19
2.3	RMS of the even-odd correlation for the standard and combined track fits. Cosmic data taking at $B = 0.1$ T and cosmic particles in full acceptance including the region of the muon filter (see Footnote 1) are also compared.	19
2.4	Inverse- p_T resolution for the standard and combined track fits.	20
2.5	RMS of the even-odd correlation for the total momentum, where $\sigma(\log_{10} p \text{ (GeV}/c))$ stands for $(1/\sqrt{2})\text{RMS}f(\log_{10} p_{\text{event-pad}} \log_{10} p_{\text{odd-pad}})$ as in Fig. 2.3 but for the total momentum.	21
2.6	Right sign probability (see definition in text) for the standard track fit as a function of p_T	21
3.1	Landau distribution with different parameters. Eq. 3.25 is evaluated with the program ROOT [Bru97].	28
3.2	Distributions of measured collisional ionization (dE/dx) in TRD by pions (<i>left</i>) and electrons (<i>right</i>) with momentum 1 GeV/c. N is the statistics.	31
3.3	Summary of the fitting results for measured collisional ionization (dE/dx).	31
3.4	Distributions of measured TRD signal with TR component ($dE/dx+TR$) by electrons with momentum 1 GeV/c (<i>left</i>) and 6 GeV/c (<i>right</i>). N is the statistics.	32
3.5	Summary of the fitting results for measured TRD $dE/dx+TR$ signal. The fitted values of σ is consistent with zero, indicating that the convolution with the Gaussian distribution is redundant.	33
4.1	One cosmic event in ALICE TPC and TRD (3D view along the beam pipe).	36
4.2	Most probable TRD signals from cosmic muons. Horizontal error bars are obtained from the estimated momentum resolution (see Chapter 2).	37
4.3	Most probable values of the TRD signals from different data sets as a function of $\beta\gamma$	39
5.1	Development of the most probable cluster signals (<i>left</i>) and the weight (<i>right</i> panel, see text for definition, $f = 0.6$) with an increasing velocity of cosmic muons. Positive and negative time-bins are for the lower and upper TRD sectors, respectively.	42

5.2	Mean values of $\langle Q \rangle_{0.6}$ from two cosmic data taking periods with $B = 0.1$ T and $B = 0.5$ T. Note that the y -scale is chosen such that the minimum ionizing signal is around 1. Signals from upper and lower sector at $B = 0.5$ T are separately shown. The discrepancy between data sets is due to uncalibrated detector effects at the cluster level (see Section 5.2).	43
5.3	Cluster signal distributions in different time-bins (<i>left</i>) before and (<i>right</i>) after the time-bin gain calibration. The black line indicates the most probable values.	44
5.4	Development of the most probable cluster signals (<i>left</i>) and the weight (<i>right</i>) after the time-bin gain calibration.	45
5.5	Mean values of $\langle Q \rangle_{0.6}$ after the time-bin gain calibration. The y -scale is chosen such that the minimum ionizing signal is around 1.	46
5.6	The mean, the standard deviation and the separation of the truncated mean signal as a function of the truncation fraction. Note that the arguments of all y -axis functions are $\log_{10} \beta\gamma$ and that the scale of the signal is chosen in such a way that $m(\log_{10} \beta\gamma = 0.55) = 1$ for all f	47
5.7	Truncated mean signals (<i>left</i>) and the number of above-baseline clusters (<i>right</i>) as a function of the velocities of the identified particles from Λ , K_s^0 decays and γ conversions [Fas12] from pp collisions at 7 TeV. The three distinct regions in $\log_{10} \beta\gamma$ are from left to right exclusively populated with protons, charged pions and electrons. The black curve is an ALEPH+logistic fit to the mean of $\langle Q \rangle_{0.55}$ (see Section 4.2).	48
5.8	Number of clusters as a function of the particle path length in the TRD. .	49
5.9	(<i>Left</i>) Scaled truncated mean signal and (<i>right</i>) the signal resolution as a function of the number of clusters.	49
5.10	Truncated mean signals as a function of momentum for charged particles in minimum bias data from p-Pb collisions at $\sqrt{s_{NN}} = 5.02$ TeV (LHC period 13c).	51
5.11	Truncated mean signals as a function of momentum for protons from Λ , charged pions from K_s^0 , and electrons from γ -conversions [Fas12] from p-Pb collisions at $\sqrt{s_{NN}} = 5.02$ TeV (LHC period 13c).	51
5.12	Probability densities of the truncated mean signal for pions from K_s^0 and electrons from γ -conversions [Fas12] from p-Pb collisions at $\sqrt{s_{NN}} = 5.02$ TeV (LHC period 13c) in the momentum bins (<i>left</i>) 0.9–1.1 GeV/c and (<i>right</i>) 3.9–4.1 GeV/c. It is obtained by requiring signals in six TRD chambers for each track and the number of (above-baseline) clusters per chamber larger than 17.	52
5.13	Correlation between pion and electron efficiencies (see text for definition) at different momenta (p-Pb collisions at $\sqrt{s_{NN}} = 5.02$ TeV, LHC period 13c). Error bars are statistical only.	52
6.1	TPC signal as a function of the momentum of traversing particles.	53

LIST OF FIGURES

6.2 Energy loss between the collision vertex and the TPC. <i>Left</i> : fitting the momentum ratio $p_{\text{vertex}}/p_{\text{TPC}}$ in a single pseudo-rapidity $ \eta $ window. The points are experimental data and the curves are the fitting results of Eq. 6.5 with the material budget L as a free parameter. <i>Right</i> : material budget L as a function of $ \eta $. The points are the fitting results of L in different $ \eta $ windows and the curves are Eq. 6.6 fitted to the points with parameter B .	55
6.3 Correlation between p_{T} and p in $0.6 < \eta < 0.8$	56
6.4 Relative difference of rapidity width at $0.6 < \eta < 0.8$ with respect to that at $ \eta < 0.2$	57
6.5 Comparison of the unbiasedness between the χ^2 and BML estimations. ToyMCs of binned distributions with different counts are used.	60
6.6 (a)-(b) Extracted fractions as functions of momentum. Connected points are the extracted values and lines are ToyMC input. (c)-(d) Fit to generated distribution at a given momentum. (a) and (c) are by the incoherent fit. (b) and (d) are by the coherent fit without regularization. A ToyMC of a (p, Δ) -distribution is used.	61
6.7 Extracted fractions by the coherent fit with and without regularization. (a)-(d) compare the extracted fractions for pions, kaons, protons and electrons, respectively, to the MC truth at the reconstruction level. Different regularization ranges ($n \pm 1, 2$) are compared. The biases at the signal crossing points are reduced to less than 20%. The ALICE MC production LHC11b10a is used.	62
6.8 Statistical weight w with $C = 10^4$ (black) as a function of momentum ($0.6 < \eta < 0.8$). The actual count N is shown as the red dashed histogram. The bin width below 4 GeV/c is 1/10 of the one above.	64
6.9 Mean signal obtained by the coherent fit, shown as the black curves overlaid on top of the measured signal distribution ($0.6 < \eta < 0.8$).	65
6.10 Comparison of the fitted mean signals (<i>left</i>) between the ALEPH and the modified Bethe-Bloch parametrizations and (<i>right</i>) between different η -windows.	65
6.11 Comparison of the fitted resolutions between the two parametrizations, Eqs. 6.18 and 6.23 (model I and II, respectively).	66
6.12 TPC signal resolution obtained by the coherent fit as a function of momentum for different particle species in (<i>left</i>) $ \eta < 0.2$ and (<i>right</i>) $0.6 < \eta < 0.8$	66
6.13 Comparison between unregularized and regularized particle fractions ($0.6 < \eta < 0.8$, the electron fraction which is at per mil level is not shown).	67
6.14 The coherent fit results projected at different momentum bins ($0.6 < \eta < 0.8$).	67
6.15 Uncorrected particle fractions from proton-proton collisions at $\sqrt{s} = 2.76$ TeV in η -windows. See text for the interpretation of the error bars and error boxes.	68

6.16 TOF fractions (defined in Eq. 6.33) obtained from data (period 11a $0.6 < \eta < 0.8$) as a function of momentum for the cuts (see text for details) with 1– and 2– σ inclusion, respectively. Also shown are the sum of TOF fractions of pions, kaons and protons.	70
6.17 The extracted remaining fractions by the TPC coherent fit A_k^{TOF} with (“w/ reg. TOF”) and without (“no reg. TOF”) regularization and the resulting calculated overall fractions A_k^{tot} (“w/ reg. TOF 2σ ”). The TOF cut with 2σ inclusion is used. (period 11a $0.6 < \eta < 0.8$)	71
6.18 Comparison among overall fractions A_k^{tot} obtained by TOF inclusion with cuts with 1– and 2– σ inclusion, respectively, and also by the “no TOF” method (period 11a $0.6 < \eta < 0.8$).	72
6.19 Comparison between the η -averaged fractions by the TOF inclusion and the “no TOF” method.	73
6.20 TOF fractions obtained from MC (LHC11b10a $0.6 < \eta < 0.8$).	74
6.21 Extension of the comparison in Fig. 6.7. Extracted fractions by the “no TOF” method and by the TOF inclusion with different cuts are compared to the MC truth.	74
7.1 $\langle N_{\text{coll}} \rangle$ as a function of the event centrality. Data from [Abe13b].	76
7.2 Ratios between normalized p_{T} -distributions after different event cuts. Generated primary particles in MC are used.	77
7.3 Comparison among contributions of secondary particles in the MC track sample selected by the track cuts.	78
7.4 Tracking efficiencies estimated in MC (10d period, pp collisions at 7TeV) for positively charged particles (<i>left</i>) and negatively charged particles (<i>right</i>).	79
7.5 Ratios between the GEANT3 and FLUKA tracking efficiencies for negative kaons (<i>left</i>) and antiprotons (<i>right</i>).	80
7.6 Δy ratios in different η -windows.	81
7.7 Comparison of the p_{T} -spectra in different collision systems with different center of mass energies.	83
7.8 Comparison of the p_{T} -spectra in pp collisions at $\sqrt{s} = 2.76$ TeV to the low p_{T} [Bus13] (TPC+ITS+TOF+HMPID) and high p_{T} [Chr13] (Lund) analyses. The high p_{T} spectra are the averages between the positive and negative particles.	84
7.9 Charge ratios for pions, kaons and protons.	85
7.10 Ratios between the measured spectra and the simultaneous blast-wave fit to π , K and p up to p_{T} 1, 1.5 and 3 GeV/ c , respectively. Results for (<i>left</i>) most central Pb–Pb collisions and (<i>right</i>) pp collisions at 2.76 TeV are shown. The vertical dashed lines indicate the upper p_{T} bounds in the fit.	86

LIST OF FIGURES

7.11 The $1-\sigma$ contour of the extracted T_{kin} and $\langle \beta_T \rangle$. Results from [Abe13a] are also shown with error boxes representing the full systematic errors including fit instability (obtained by varying the setting – see text for details – with respect to the standard one). For Pb–Pb collisions, $\langle \beta_T \rangle$ increases as the collisions become more central.	86
7.12 Comparison of $(p^+ + p^-)/(\pi^+ + \pi^-)$ in different collision systems with different center of mass energies. In the <i>right</i> panel the inverse of the ratio to the reference data is shown with focus on pp and Pb–Pb collisions at the same energy.	88
7.13 Comparison of $(K^+ + K^-)/(\pi^+ + \pi^-)$ in different collision systems with different center of mass energies.	88
7.14 Nuclear modification factors for pions, kaons and protons.	89
7.15 Uncorrected particle fractions (normalized to the total amount of primary pions, kaons and protons) extracted from charged leading jets of p_T 10–80 GeV/ c in pp collisions at $\sqrt{s} = 7$ TeV by the TPC coherent fit without TOF pre-identification. The results are compared to MC simulations (see text for details). Also shown are the uncorrected particle fractions from the inclusive primary particle sample obtained by the same event and track selections but without jet reconstruction.	91
A.1 Invariant mass distribution of exclusive two-pion events with veto detectors V0 (<i>left</i>) and V0-FMD-SPD-TPC (<i>right</i>). Events with like-sign tracks are compared.	96
A.2 Like-sign subtracted invariant mass distribution (events with double gaps) with veto detectors V0 (<i>left</i>) and V0-FMD-SPD-TPC (<i>right</i>). Non-exclusive events (no gap) are compared.	96

List of Tables

2.1	Flow of loss of statistics in each step of the combined cosmic track fit. Data was taken in May–June 2011 with 0.5 T B-field and TOF back-to-back trigger. Only events with 2 standard tracks are used.	17
2.2	Transverse momentum resolution for the TPC standard and combined track fits.	20
4.1	Fitted parameters of the ALEPH parametrization to the dE/dx TRD signal.	38
4.2	Fitted parameters of the ALEPH+logistic parametrization to the $dE/dx+TR$ TRD signal.	38
6.1	Iterations in the guided convergence. Note the minus signs in front.	63
6.2	Fitted parameters of the ALEPH parametrization ($0.6 < \eta < 0.8$). The number in the parenthesis is the statistical uncertainty in the last digit.	65
6.3	TOF identification efficiency (defined in Eq. 6.35) after a cut of 2σ inclusion and 4σ exclusion in period 11a $0.6 < \eta < 0.8$	71
7.1	Summary of data sets used in the particle production analysis.	76
7.2	Comparison between the ratio of the normalized p_T -distributions and the inverse ratio of the event numbers ($0.6 < \eta < 0.8$). The former is obtained by a fit of a constant to the ratio. Effect of the Vtx cut is shown.	77
7.3	Comparison between the ratio of the normalized p_T -distributions and the inverse ratio of the event numbers ($0.6 < \eta < 0.8$). The former is obtained by a fit of a constant to the ratio. Effect of the Z_{vtx} cut is shown.	77
7.4	Extracted T_{kin} , $\langle \beta_T \rangle$ and n from the blast-wave fit to the spectra from Pb–Pb and pp collisions. The reduced χ^2 is also shown.	87
A.1	Number of selected events and exclusivity measured by the unlike-sign to like-sign ratio for different veto conditions.	95

LIST OF TABLES

Bibliography

- [Aad12] G. Aad *et al.* [ATLAS Collaboration], “Observation of a new particle in the search for the Standard Model Higgs boson with the ATLAS detector at the LHC,” Phys. Lett. B **716** (2012) 1.
- [Aam08] K. Aamodt *et al.* [ALICE Collaboration], “The ALICE experiment at the CERN LHC,” JINST **3** (2008) S08002.
- [Aam11a] K. Aamodt *et al.* [ALICE Collaboration], “Suppression of Charged Particle Production at Large Transverse Momentum in Central Pb–Pb Collisions at $\sqrt{s_{NN}} = 2.76$ TeV,” Phys. Lett. B **696** (2011) 30.
- [Aam11b] K. Aamodt *et al.* [ALICE Collaboration], “Production of pions, kaons and protons in pp collisions at $\sqrt{s} = 900$ GeV with ALICE at the LHC,” Eur. Phys. J. C **71** (2011) 1655.
- [Aam13] K. Aamodt *et al.* [ALICE Collaboration], “Study of charged jet production cross sections and properties in proton-proton collisions at $\sqrt{s} = 7$ TeV,” paper in preparation (2013).
- [Abb13] E. Abbas *et al.* [ALICE Collaboration], “Mid-rapidity anti-baryon to baryon ratios in pp collisions at $\sqrt{s} = 0.9$, 2.76 and 7 TeV measured by ALICE,” arXiv:1305.1562 [nucl-ex].
- [Abe06] B. I. Abelev *et al.* [STAR Collaboration], “Identified baryon and meson distributions at large transverse momenta from Au+Au collisions at $s(\text{NN})^{**}(1/2) = 200$ -GeV,” Phys. Rev. Lett. **97** (2006) 152301.
- [Abe13a] B. Abelev *et al.* [ALICE Collaboration], “Centrality dependence of π , K, p production in Pb-Pb collisions at $\sqrt{s_{NN}} = 2.76$ TeV,” arXiv:1303.0737 [hep-ex].
- [Abe13b] B. Abelev *et al.* [ALICE Collaboration], “Centrality determination of Pb-Pb collisions at $\text{sqrt}(s_{\text{NN}}) = 2.76$ TeV with ALICE,” arXiv:1301.4361 [nucl-ex].
- [Abe13c] B. Abelev *et al.* [ALICE Collaboration], “Energy Dependence of the Transverse Momentum Distributions of Charged Particles in pp Collisions Measured by ALICE,” arXiv:1307.1093 [nucl-ex].
- [Abe13d] B. Abelev *et al.* [ALICE Collaboration], “Centrality Dependence of Charged Particle Production at Large Transverse Momentum in Pb–Pb Collisions at $\sqrt{s_{NN}} = 2.76$ TeV,” Phys. Lett. B **720** (2013) 52.

BIBLIOGRAPHY

- [Abr72] M. Abramowitz, I. Stegun (eds.) “Handbook of Mathematical Functions with Formulas, Graphs, and Mathematical Tables,” 10ed., NBS (1972) p. 228-229.
- [Ada05] J. Adams *et al.* [STAR Collaboration], “Experimental and theoretical challenges in the search for the quark gluon plasma: The STAR Collaboration’s critical assessment of the evidence from RHIC collisions,” Nucl. Phys. A **757** (2005) 102.
- [Adc02a] K. Adcox *et al.* [PHENIX Collaboration], “Centrality dependence of pi+ / pi-, K+ / K-, p and anti-p production from $s(\text{NN})^{**}(1/2) = 13\text{-GeV}$ Au+Au collisions at RHIC,” Phys. Rev. Lett. **88** (2002) 242301.
- [Adc02b] K. Adcox *et al.* [PHENIX Collaboration], “Suppression of hadrons with large transverse momentum in central Au+Au collisions at $\sqrt{s_{NN}} = 130\text{-GeV}$,” Phys. Rev. Lett. **88** (2002) 022301.
- [Adc05] K. Adcox *et al.* [PHENIX Collaboration], “Formation of dense partonic matter in relativistic nucleus-nucleus collisions at RHIC: Experimental evaluation by the PHENIX collaboration,” Nucl. Phys. A **757** (2005) 184.
- [Adl02] C. Adler *et al.* [STAR Collaboration], “Centrality dependence of high p_T hadron suppression in Au+Au collisions at $\sqrt{s_{NN}} = 130\text{-GeV}$,” Phys. Rev. Lett. **89** (2002) 202301.
- [Adl03] S. S. Adler *et al.* [PHENIX Collaboration], “Scaling properties of proton and anti-proton production in $s(\text{NN})^{**}(1/2)$ 200-GeV Au+Au collisions,” Phys. Rev. Lett. **91** (2003) 172301.
- [Alf08] M. G. Alford, A. Schmitt, K. Rajagopal and T. Schäfer, “Color superconductivity in dense quark matter,” Rev. Mod. Phys. **80** (2008) 1455.
- [Alm10] J. Alme, Y. Andres, H. Appelshauser, S. Bablok, N. Bialas, R. Bolgen, U. Bonnes and R. Bramm *et al.*, “The ALICE TPC, a large 3-dimensional tracking device with fast readout for ultra-high multiplicity events,” Nucl. Instrum. Meth. A **622** (2010) 316.
- [Amb03] M. Ambrosio *et al.* [MACRO Collaboration], “Measurement of the residual energy of muons in the Gran Sasso underground laboratories,” Astropart. Phys. **19**, 313 (2003).
- [And12] A. Andronic and J. P. Wessels, “Transition Radiation Detectors,” Nucl. Instrum. Meth. A **666** (2012) 130.
- [Aok06] Y. Aoki, G. Endrodi, Z. Fodor, S. D. Katz and K. K. Szabo, “The Order of the quantum chromodynamics transition predicted by the standard model of particle physics,” Nature **443** (2006) 675.
- [Ars05] I. Arsene *et al.* [BRAHMS Collaboration], “Quark gluon plasma and color glass condensate at RHIC? The Perspective from the BRAHMS experiment,” Nucl. Phys. A **757** (2005) 1.

- [Bac05] B. B. Back, M. D. Baker, M. Ballintijn, D. S. Barton, B. Becker, R. R. Betts, A. A. Bickley and R. Bindel *et al.*, “The PHOBOS perspective on discoveries at RHIC,” Nucl. Phys. A **757** (2005) 28.
- [Bai06] R. Bailhache *et al.* [ALICE TRD Collaboration], “New test beam results with prototypes of the ALICE TRD,” Nucl. Instrum. Meth. A **563** (2006) 310.
- [Baz10] A. Bazavov *et al.* [HotQCD Collaboration], “Taste symmetry and QCD thermodynamics with improved staggered fermions,” PoS LATTICE **2010** (2010) 169.
- [Ber12] J. Beringer *et al.* [Particle Data Group Collaboration], “Review of Particle Physics (RPP),” Phys. Rev. D **86** (2012) 010001.
- [Bil84] P. Billoir, “Track Fitting With Multiple Scattering: A New Method,” Nucl. Instrum. Meth. A **225** (1984) 352.
- [Bjo82] J. D. Bjorken, preprint Fermilab-Pub-82/59-THY (1982) and erratum, unpublished.
- [Blu08] W. Blum, W. Riegler, L. Rolandi, “Particle Detection with Drift Chambers,” Springer-Verlag Berlin Heidelberg (2008).
- [Bor10a] S. Borsanyi *et al.* [Wuppertal-Budapest Collaboration], “Is there still any T_c mystery in lattice QCD? Results with physical masses in the continuum limit III,” JHEP **1009** (2010) 073.
- [Bor10b] S. Borsanyi, G. Endrodi, Z. Fodor, A. Jakovac, S. D. Katz, S. Krieg, C. Ratti and K. K. Szabo, “The QCD equation of state with dynamical quarks,” JHEP **1011** (2010) 077.
- [Bra96] P. Braun-Munzinger, J. Stachel, J. P. Wessels and N. Xu, “Thermal and hadrochemical equilibration in nucleus-nucleus collisions at the SPS,” Phys. Lett. B **365** (1996) 1.
- [Bra03] P. Braun-Munzinger, K. Redlich and J. Stachel, “Particle production in heavy ion collisions,” In *Hwa, R.C. (ed.) et al.: Quark gluon plasma* 491-599 [nucl-th/0304013].
- [Bra07] P. Braun-Munzinger and J. Stachel, “The quest for the quark-gluon plasma,” Nature **448** (2007) 302.
- [Brau07] J. Braun and H. Gies, “Running coupling at finite temperature and chiral symmetry restoration in QCD,” Phys. Lett. B **645** (2007) 53.
- [Bre69] M. Breidenbach, J. I. Friedman, H. W. Kendall, E. D. Bloom, D. H. Coward, H. C. DeStaeler, J. Drees and L. W. Mo *et al.*, “Observed Behavior of Highly Inelastic electron-Proton Scattering,” Phys. Rev. Lett. **23** (1969) 935.
- [Bro04] W. Broniowski, W. Florkowski and L. Y. .Glozman, “Update of the Hagedorn mass spectrum,” Phys. Rev. D **70** (2004) 117503. W. Broniowski and W. Florkowski, “Different Hagedorn temperatures for mesons and baryons from experimental mass spectra, compound hadrons, and combinatorial saturation,” Phys. Lett. B **490** (2000) 223.

BIBLIOGRAPHY

- [Bro08] S. J. Brodsky and A. Sickles, “The Baryon Anomaly: Evidence for Color Transparency and Direct Hadron Production at RHIC,” Phys. Lett. B **668** (2008) 111.
- [Bru94] R. Brun, F. Carminati and S. Giani, “GEANT Detector Description and Simulation Tool,” CERN-W5013.
- [Bru97] R. Brun and F. Rademakers, “ROOT: An object oriented data analysis framework,” Nucl. Instrum. Meth. A **389**, 81 (1997).
- [Bus13] R. Bustamante *et al.* ” π , K, p analysis in pp collisions at $\sqrt{s} = 2.76$ TeV,” ALICE analysis note (2013).
- [Cab75] N. Cabibbo and G. Parisi, “Exponential Hadronic Spectrum and Quark Liberation,” Phys. Lett. B **59** (1975) 67.
- [Cha12a] S. Chatrchyan *et al.* [CMS Collaboration], “Combined results of searches for the standard model Higgs boson in pp collisions at $\sqrt{s} = 7$ TeV,” Phys. Lett. B **710** (2012) 26.
- [Cha12b] S. Chatrchyan *et al.* [CMS Collaboration], “Study of high-pT charged particle suppression in PbPb compared to pp collisions at $\sqrt{s_{NN}} = 2.76$ TeV,” Eur. Phys. J. C **72** (2012) 1945.
- [Chr13] P. Christiansen *et al.* ”Particle identification at high- p_T with TPC-dE/dx in the relativistic rise,” ALICE analysis note (2013).
- [Col75] J. C. Collins and M. J. Perry, “Superdense Matter: Neutrons Or Asymptotically Free Quarks?,” Phys. Rev. Lett. **34** (1975) 1353.
- [Cor01] P. Cortese *et al.* [ALICE Collaboration], “ALICE: Technical Design Report of the Transition Radiation Detector,” CERN-LHCC-2001-021 (2001).
- [Dec90] D. Decamp *et al.* [ALEPH Collaboration], “ALEPH: A detector for electron-positron annihilation at LEP,” Nucl. Instrum. Meth. A **294** (1990) 121 [Erratum-ibid. A **303** (1991) 393].
- [Del00a] G. Dellacasa *et al.* [ALICE Collaboration], “ALICE technical design report of the time-of-flight system (TOF),” CERN-LHCC-2000-012 (2000).
- [Del00b] G. Dellacasa *et al.* [ALICE Collaboration], “ALICE: Technical design report of the time projection chamber,” CERN-OPEN-2000-183 (2000).
- [Dol93] B. Dolgoshein, “Transition radiation detectors,” Nucl. Instrum. Meth. A **326** (1993) 434.
- [Eng81] J. Engels, F. Karsch, H. Satz and I. Montvay, “High Temperature SU(2) Gluon Matter on the Lattice,” Phys. Lett. B **101** (1981) 89.
- [Eva08] L. Evans and P. Bryant, “LHC Machine,” JINST **3** (2008) S08001.
- [Fas12] M. Fasel, “Single-electron analysis and open charm cross section in proton-proton collisions at $\sqrt{s} = 7$ TeV,” Ph.D. Thesis at Technische Universität Darmstadt (2012).

- [Fer05] A. Ferrari, P. R. Sala, A. Fasso and J. Ranft, “FLUKA: A multi-particle transport code (Program version 2005),” CERN-2005-010.
- [Fri08] R. J. Fries, V. Greco and P. Sorensen, “Coalescence Models For Hadron Formation From Quark Gluon Plasma,” *Ann. Rev. Nucl. Part. Sci.* **58** (2008) 177.
- [Fuk11] K. Fukushima and T. Hatsuda, “The phase diagram of dense QCD,” *Rept. Prog. Phys.* **74** (2011) 014001.
- [Gas82] J. Gasser and H. Leutwyler, “Quark Masses,” *Phys. Rept.* **87** (1982) 77.
- [Gro73] D. J. Gross and F. Wilczek, “Ultraviolet Behavior of Nonabelian Gauge Theories,” *Phys. Rev. Lett.* **30** (1973) 1343.
- [Gro81] D. J. Gross, R. D. Pisarski and L. G. Yaffe, “QCD and Instantons at Finite Temperature,” *Rev. Mod. Phys.* **53** (1981) 43.
- [Gyu90] M. Gyulassy and M. Plumer, “Jet Quenching In Dense Matter,” *Phys. Lett. B* **243** (1990) 432.
- [Hag65] R. Hagedorn, “Statistical thermodynamics of strong interactions at high-energies,” *Nuovo Cim. Suppl.* **3** (1965) 147.
- [Hei00] U. W. Heinz and M. Jacob, “Evidence for a new state of matter: An Assessment of the results from the CERN lead beam program,” *nucl-th/0002042*.
- [Iva12] M. Ivanov, private communication (2012).
- [Jac99] J. D. Jackson, “Classical electrodynamics,” 3ed., Wiley (1999) Chapter 13.
- [Ken79] M. Kendall, A. Stuart, “The advanced theory of statistics,” 4ed., vol. 2, CHARLES GRIFFIN & COMPANY LIMITED, England (1979).
- [Kog75] J. B. Kogut and L. Susskind, “Hamiltonian Formulation of Wilson’s Lattice Gauge Theories,” *Phys. Rev. D* **11** (1975) 395.
- [Kog82] J. B. Kogut, M. Stone, H. W. Wyld, J. Shigemitsu, S. H. Shenker and D. K. Sinclair, “The Scales of Chiral Symmetry Breaking in Quantum Chromodynamics,” *Phys. Rev. Lett.* **48** (1982) 1140.
- [Kog83] J. B. Kogut, M. Stone, H. W. Wyld, W. R. Gibbs, J. Shigemitsu, S. H. Shenker and D. K. Sinclair, “Deconfinement and Chiral Symmetry Restoration at Finite Temperatures in SU(2) and SU(3) Gauge Theories,” *Phys. Rev. Lett.* **50** (1983) 393.
- [Kol03] P. F. Kolb and U. W. Heinz, “Hydrodynamic description of ultrarelativistic heavy ion collisions,” In *Hwa, R.C. (ed.) et al.: Quark gluon plasma* 634-714.
- [Kut81] J. Kuti, J. Polonyi and K. Szlachanyi, “Monte Carlo Study of SU(2) Gauge Theory at Finite Temperature,” *Phys. Lett. B* **98** (1981) 199.
- [Lan44] L. D. Landau, “On the energy loss of fast particles by ionization,” *J. Phys. (USSR)* **8** (1944) 201. See also D. Ter Haar (ed.), “Collected Papers of L. D. Landau,” Gordon & Breach Science (1965) p. 417.

BIBLIOGRAPHY

- [Loh13] D. Lohner, “Anisotropic flow of direct photons in Pb-Pb collisions at s(NN)=2.76 TeV,” Ph.D. Thesis at Universität Heidelberg (2013).
- [Lu11] X. Lu, [for the ALICE Collaboration] “Combined TPC Track-fit for Cosmic Rays and Implementation in AliROOT,” <https://indico.cern.ch/contributionDisplay.py?contribId=0&confId=160767> (2011).
- [Mar06] R.A. Maronna, R.D. Martin, V.J. Yohai, “Robust Statistics – Theory and Methods,” John Wiley & Sons Ltd, England (2006).
- [McL81] L. D. McLerran and B. Svetitsky, “Quark Liberation at High Temperature: A Monte Carlo Study of SU(2) Gauge Theory,” Phys. Rev. D **24** (1981) 450.
- [Mul12] B. Muller, J. Schukraft and B. Wyslouch, “First Results from Pb+Pb collisions at the LHC,” Ann. Rev. Nucl. Part. Sci. **62** (2012) 361.
- [Pol73] H. D. Politzer, “Reliable Perturbative Results for Strong Interactions?,” Phys. Rev. Lett. **30** (1973) 1346.
- [Pol78] A. M. Polyakov, “Thermal Properties of Gauge Fields and Quark Liberation,” Phys. Lett. B **72** (1978) 477.
- [Sch93] E. Schnedermann, J. Sollfrank and U. W. Heinz, “Thermal phenomenology of hadrons from 200-A/GeV S+S collisions,” Phys. Rev. C **48** (1993) 2462.
- [Sch03] D. J. Schwarz, “The first second of the universe,” Annalen Phys. **12** (2003) 220.
- [Shi79a] M. A. Shifman, A. I. Vainshtein and V. I. Zakharov, “QCD and Resonance Physics. Sum Rules,” Nucl. Phys. B **147** (1979) 385.
- [Shi79b] M. A. Shifman, A. I. Vainshtein and V. I. Zakharov, “QCD and Resonance Physics: Applications,” Nucl. Phys. B **147** (1979) 448.
- [Shu78] E. V. Shuryak, “Theory of Hadronic Plasma,” Sov. Phys. JETP **47** (1978) 212 [Zh. Eksp. Teor. Fiz. **74** (1978) 408].
- [Shu04] E. Shuryak, “Why does the quark gluon plasma at RHIC behave as a nearly ideal fluid?,” Prog. Part. Nucl. Phys. **53** (2004) 273.
- [Shu09] E. Shuryak, “Physics of Strongly coupled Quark-Gluon Plasma,” Prog. Part. Nucl. Phys. **62** (2009) 48.
- [Sjo06] T. Sjostrand, S. Mrenna and P. Z. Skands, “PYTHIA 6.4 Physics and Manual,” JHEP **0605** (2006) 026.
- [Ska10] P. Z. Skands, “Tuning Monte Carlo Generators: The Perugia Tunes,” Phys. Rev. D **82** (2010) 074018.
- [Sol64] F. T. Solmitz, “Analysis of experiments in particle physics,” Ann. Rev. Nucl. Part. Sci. **14** (1964) 375.
- [Sta93] J. Stachel and G. R. Young, “Relativistic heavy ion physics at CERN and BNL,” Ann. Rev. Nucl. Part. Sci. **42** (1992) 537.

- [Sus79] L. Susskind, “Lattice Models of Quark Confinement at High Temperature,” Phys. Rev. D **20** (1979) 2610.
- [Top11] V. Topor Pop, M. Gyulassy, J. Barrette and C. Gale, “Baryon anomaly and strong color fields in Pb+Pb collisions at 2.76A TeV at the CERN Large Hadron Collider,” Phys. Rev. C **84** (2011) 044909.
- [Wan92] X. -N. Wang and M. Gyulassy, “Gluon shadowing and jet quenching in A + A collisions at $s^{**}(1/2) = 200\text{-GeV}$,” Phys. Rev. Lett. **68** (1992) 1480.
- [Wil74] K. G. Wilson, “Confinement of Quarks,” Phys. Rev. D **10** (1974) 2445.
- [Wil92] William H. Press, Saul A. Teukolsky, William T. Vetterling, and Brian P. Flannery. “Numerical Recipes in C: The Art of Scientific Computing,” 2ed., Cambridge University Press, New York, NY, USA (1992).

BIBLIOGRAPHY

Acknowledgment

I would like to thank my supervisor Prof. Johanna Stachel for all her supports, both academic and personal. I am grateful for the much valuable advice and insightful comments. Even at her busiest time as Präsidentin der Deutsche Physikalische Gesellschaft she is always available for my questions. The moments when I discussed with her about my different ideas are always remembered.

I would like to thank Prof. Norbert Herrmann for providing me a position in the International Research Training Group (IRTG). I have learned a lot as tutor in his lectures. I am grateful for the cheerful discussions with him.

I would like to thank Prof. Carlo Ewerz and Dr. Klaus Reygers for taking the responsibility as my second supervisors. Thank Klaus again for proofreading this thesis.

I would like to thank Dr. Marian Ivanov. We have worked on many topics in this thesis since 2010 when I first tried to realize the cosmic track fit. I have benefited a lot from his expertise. The coffee and lunch time with him is always enjoyable.

I would like to thank Dr. Oliver Busch. We collaborated on the jet analysis. I have benefited a lot from his careful reading each page of the whole thesis draft and the inspiring comments. This thesis has improved a lot with his help. (Needless to say, this thesis has suffered from my constant modifications until the day of submission. The full responsibility of any kind of errors is on me.)

I would like to thank all the people I have worked with, especially Dr. Alexander Kalweit, Dr. Alexandru Bercuci, Dr. Anton Andronic, Dr. Antonio Ortiz Velasquez, Prof. Dr. Christoph Blume, Dr. Jens Wiechula, Dr. Joerg Lehnert, Dr. Markus Fasel, Dr. Peter Christiansen, Dr. Rainer Schicker, and Dr. Raphaelle Bailhache. Their discussions and help are greatly acknowledged.

I would like to thank my colleagues in Heidelberg, especially Alice Zimmermann, Dr. Min-Jung Kweon, Dr. Yvonne Pachmayer for being wonderful office mates, and Dr. Antonin Maire, Daniel Lohner, Jochen Klein, Dr. Kai Schweda, Michael Winn for various discussions.

My thanks also go to Dr. Monica Dunford for proofreading this thesis.

I owe many thanks to my family for their understanding and support throughout these years.